Femtosecond Structural Dynamics on the Atomic Length Scale

Dissertation

zur Erlangung des Doktorgrades

des Fachbereichs Physik

der Universität Hamburg

vorgelegt von

Dongfang Zhang

aus Shandong, China

Hamburg

2013

Gutachter der Dissertation:	Prof. Dr. R. J. Dwayne Miller Dr. Klaus Flöttmann
Gutachter der Disputation:	Prof. Dr. R. J. Dwayne Miller Prof. Dr. Nils Huse
Datum der Disputation:	17.12.2013
Vorsitzender des Prüfungsausschusses:	Prof. Dr. Peter Schmelcher
Vorsitzender des Promotionsausschusses:	Prof. Dr. Peter Hauschildt
Dekan der MIN Fakultät:	Prof. Dr. Heinrich Graener
Leiter des Department Physik:	Prof. Dr. Daniela Pfannkuche

Abstract

This thesis reports on the development and application of two different but complementary ultrafast electron diffraction setups built at the Max Planck Research Department for Structural Dynamics. One is an ultra-compact femtosecond electron diffraction (FED) setup (Egun300), which is currently operational (with a maximum electron energy of 150 keV) and provides ultrashort ($\sim$300 fs) and bright ($\sim$10 e/μm^2) electron bunches. The other one, named as Relativistic Electron Gun for Atomic Exploration (REGAE) is a radio frequency driven 2 to 5 MeV FED setup built in collaboration with different groups from DESY. REGAE was developed as a facility that will provide high quality diffraction with sufficient coherence to even address structural protein dynamics and with electron pulses as short as 20 fs (FWHM).

As one of the first students in Prof. R.J. Dwayne Miller's group, I led the femtosecond (fs) laser sub-group at REGAE being responsible for the construction of different key optical elements required to drive both of aforementioned FED systems. A third harmonic generation (THG) and a nonlinear optical parametric amplifier (NOPA) have been used for the photo-generation of ultrashort electron bursts as well as sample laser excitation. Different diagnostic tools have been constructed to monitor the performance of the fs optical system. A fast autocorrelator was developed to provide on the fly pulse duration correction. A transient-grating frequency-resolved optical gating (TG-FROG) was built to obtain detail information about the characteristics of fs optical pulse, i.e. phase and amplitude of its spectral components.

In addition to these optical setups, I developed a fs optical pump-probe system, which supports broadband probe pulses. This setup was successfully applied to investigate the semiconductor-to-metal photoinduced phase transition in VO_2 and the ultrafast photo-reduction mechanism of graphene oxide.

In regard to FED setups, I have been deeply involved in their development. I performed the first study in our compact FED system. I studied the optical and structural response of alkali halides to intense UV excitation conditions, i.e. above the damage threshold of the samples which required the application of a single-shot scheme. In order to gain a better understanding of the ablation process that follows fs optical excitation in alkali halides, I applied a variety of different techniques. Optical reflectivity, femtosecond electron diffraction, ion detection and crater measurements revealed the existence of a cold ablation process that occurs well below the threshold for plasma formation and even that for the melting point of the salts. This atypical cold explosion owes to the presence of highly localized excitonic states and reflects the repulsive nature of initial electronic correlations at play.

In the case of REGAE, we performed the first time-resolved experiment following the fs laser heating dynamics and partial melting of polycrystalline gold films. This experiment was crucial to test the overall synchronization of our REGAE machine. We were able to observe a clear dynamics under single-shot photo-excitation conditions and found time zero within 1 picosecond. Further electron pulse characterization will involve the implementation of ponderomotive scattering. I have already constructed the required modular setup and performed all preliminary ASTRA N-body simulations.

Kurzfassung

Diese Dissertation beschäftigt sich mit der Entwicklung und Anwendung zweier sich ergänzender Aufbauten für ultraschnelle Elektronenbeugungsexperimente, die innerhalb der Max Planck Forschungsabteilung für strukturelle Dynamik aufgebaut wurden. Ein kompakter Aufbau für Femtosekunden - Elektronendiffraktion (FED) wird derzeit mit maximal 150 keV betrieben und erzeugt ultrakurze Elektronenpulse von bis zu 300 fs bei einer hohen Helligkeit von 10 $e/\mu m^2$. Der zweite Aufbau, genannt REGAE (*Relativistic Electron Gun for Atomic Exploration*), wurde in Zusammenarbeit mit verschiedenen DESY Gruppen erbaut. REGAE ist ein mit Hochfrequenz betriebener FED Aufbau, der im Energiebereich von 2 bis 5 MeV Beugungsbilder hoher Qualität erzeugen wird. Dabei soll eine derart hohe Strahkohärenz erreicht werden, um strukturelle Dynamik in Proteinkristallen mit Pulsen von bis zu 20 fs beobachten zu können.

Als einer der ersten Doktroranden in der Gruppe von Prof. R.J. Dwayne Miller war ich für den Aufbau der Schlüsselelemente des Femtosekunden Lasersystems für beide zuvor genannten FED Aufbauten verantwortlich. Ein Aufbau zur Erzeugung der dritten Harmonischen (THG) sowie ein nichtlinearer optisch parametrischer Verstärker (NOPA) wurden für die Photoanregung kurzer Elektronenpulse sowie die Anregung der Proben verwendet. Verschiedene Diagnosewerkzeuge wurden aufgebaut um die Eigenschaften des Systems zu überwachen. Ein schneller Autokorrelator dient der Echtzeitkorrektur der Pulslänge. Ein TG-FROG (*transient-grating frequency-resolved optical gating*) wurde gebaut um die Eigenschaften des fs-Laserpulses, wie die Phase und Amplitude seiner Spektralkomponenten detailliert zu charakterisieren.

Zusätzlich wurde ein Femtosekunden *Pump-Probe* Aufbau entwickelt, der breitbandige Pulse zum Abtasten erzeugt. Dieser Aufbau wurde erfolgreich verwendet um den lichtinduzierten Halbleiter-Metall-Phasenübergang in VO_2, sowie den ultraschnellen Photoreduktionsmechanismus in Graphenoxid zu studieren.

Des Weiteren werden maßgebliche Entwicklungen der FED-Experimente beschrieben. In der ersten Studie mit dem kompakten 150 keV FED Aufbau wurde die optische und strukturelle Reaktion von Alkalihaliden auf intensive Anregung mit UV-Strahlen beobachtet. Da die Anregung oberhalb der Zerstörschwelle des Materials stattfand, musste eine Einzelschusskonfiguration gewählt werden. Verschiedene Techniken wurden angewandt um ein besseres Verständnis der optischen Anregung in Alkalihaliden zu gewinnen. Die Untersuchungen mittels Messung der Reflektivität, Femtosekunden - Elektronenbeugung, Detektion von Ionen und Bestimmung der Kratertiefe deckten einen kalten Ablationsprozess auf, der weit unter der Schwelle für Plasmaerzeugung und sogar unter dem Schmelzpunkt des Salzes stattfand.

Mit REGAE wurden erste zeitaufgelöste Experimente durchgeführt, um die Erwärmungdynamik und das darauffolgende Schmelzen nach Beschuss mit Laserpulsen zu verfolgen, was auch als wichtiger Test für die Synchronisierung diente. Unter Einzelschussbedingungen konnte eine eindeutige Dynamik beaobachtet werden, wobei sich der zeitliche Nullpunkt innerhalb einer Pikosekunde festlegen ließ. Die weitere Charakterisierung der Elektronenpulse wird mit Hilfe von ponderomotorischer Streuung erfolgen. Der benötigte modulare Aufbau wurde bereits erstellt und die dazugehörigen Vielteilchensimulationen mit ASTRA durchgeführt.

Contents

1. Introduction **1**
- 1.1. Basics of electron diffraction . . . 2
- 1.2. History of time-resolved electron diffraction . . . 4
- 1.3. Thesis outline . . . 6

2. Femtosecond laser system **9**
- 2.1. Ti:sapphire laser system . . . 9
  - 2.1.1. Oscillator (Micra-5) . . . 9
  - 2.1.2. Laser amplifier . . . 10
  - 2.1.3. Characterization . . . 10
- 2.2. Laser setups for FED systems . . . 14
  - 2.2.1. Photocathode laser setup in FED systems . . . 14
  - 2.2.2. Laser pump arm for sample excitation . . . 24
  - 2.2.3. Synchronization of the laser system with RF . . . 25
- 2.3. Femtosecond optical pump-probe spectroscopy system . . . 27
  - 2.3.1. Layout of optical pump-probe setup . . . 28
  - 2.3.2. Automation and characterization of the system . . . 29
- 2.4. Summary . . . 32

3. Development of Femtosecond Electron Diffraction system **33**
- 3.1. Compact Femtosecond Electron diffraction system . . . 33
  - 3.1.1. Compact electron gun configuration . . . 33
  - 3.1.2. Time-resolved electron diffraction measurement . . . 37
- 3.2. Relativistic electron gun for atomic exploration – REGAE . . . 40
  - 3.2.1. REGAE beamline . . . 41
  - 3.2.2. Main characteristics of REGAE (ASTRA simulation) . . . 46
  - 3.2.3. Femtosecond electron diffraction with REGAE . . . 46
- 3.3. Summary . . . 50

4. Hot electron driven phase transition **51**
- 4.1. Introduction . . . 51
- 4.2. Experimental setup . . . 53
- 4.3. Optical pump-probe results . . . 55
- 4.4. Discussion . . . 59
- 4.5. Conclusion . . . 62
- 4.6. Future outlook . . . 62

5. Electronically-driven ablation via highly localized electronic states **65**
- 5.1. Introduction . . . 65

5.2. Results and discussion 66
5.2.1. Time-resolved optical reflectivity measurements 66
5.2.2. Ion measurement 69
5.2.3. Surface crater observation 70
5.2.4. Estimation of the fraction of excited halide centers 73
5.2.5. Time-resolved electron diffraction measurements 76
5.3. Conclusion 87

6. Characterization of electron time zero and pulse duration in REGAE 89
6.1. Time zero of REGAE 89
6.2. Precise bunch length and timing measurement for REGAE 92
6.3. Conclusion 97

7. Summary and outlook 99

Appendix 101

A. ASTRA Codes 103
A.1. Generator 103
A.2. ASTRA 104

B. Coupled-wave equation 107

Bibliography 109

List of Publications 123

Acknowledgments 125

List of Figures

1.1. Schematic of electron diffraction 3
1.2. Diffraction pattern of single crystalline silicon and polycrystalline gold . . 4
1.3. Calculated elastic mean free path of different materials 5
1.4. Schematic of the potential energy surfaces in different materials 7

2.1. Temperature change on the optical table 11
2.2. Layout of an autocorrelator 11
2.3. Schematic of a PG-FROG 13
2.4. Home-made TG-FROG 13
2.5. Schematic of THG generation 15
2.6. Calculated SHG generation with different BBO crystal thickness 15
2.7. Layout of the excitation laser setup for the photocathode of REGAE 17
2.8. Laser pointing drift with and without the stabilizer 18
2.9. Electron bunch length and transverse emittance as a function of UV pulse duration (ASTRA simulation) 18
2.10. Measured UV pulse duration 20
2.11. The influence of uniform and gaussian longitudinal laser beam distribution to the transverse emittance (ASTRA simulation) 20
2.12. Configuration of 4f setup 21
2.13. Temporal flat-top beam Generation 21
2.14. Transverse emittance as a function of UV beam diameter (ASTRA simulation) 22
2.15. Transverse emittance with respect to a flat-top and gaussian photocathode laser beam (ASTRA simulation) 23
2.16. Layout of the transverse beam profile control 23
2.17. Schematic of a noncollinear interaction geometry and phase matching angle 24
2.18. Diagram of synchronization setup for REGAE 25
2.19. Stability of laser with and without the noise eater 26
2.20. Timing jitter from phase and amplitude change of RF field (ASTRA simulation) 27
2.21. Layout of an optical pump-probe setup 28
2.22. Knife-edge beamdiameter measurement 30
2.23. Beamdiameter measurement GUI 31
2.24. Optical pump-probe GUI 32

3.1. Principle of the pulsed electron generation in the compact FED system . . 34
3.2. Correlation between the electron density and the electron pulse duration (ASTRA simulation) 35
3.3. Assembly of Egun300 vacuum chamber 36
3.4. GUI for laser beam pointing optimization and beam overlap 38

3.5. Layout of the compact FED machine . . . 39
3.6. GUI for data acquisition of the compact FED system . . . 40
3.7. Layout of the REGAE beamline . . . 41
3.8. Correlation of the thermal emittance to the transverse coherence length (ASTRA simulation) . . . 43
3.9. Bunch length with and without the Buncher cavity (ASTRA simulation) . . . 43
3.10. REGAE Sample chamber . . . 44
3.11. Calibrated electron energy relative to the dipole current . . . 45
3.12. REGAE detector system . . . 45
3.13. Characteristics of REGAE (ASTRA simulation) . . . 47
3.14. REGAE control panel . . . 48
3.15. Layout of REGAE FED system . . . 49
3.16. GUI for data acquisition of REGAE . . . 50

4.1. The Structure of VO_2 . . . 52
4.2. The structure of the Au/VO2/ITO sample . . . 54
4.3. The changes in transmission as a function of time for VO_2/sapphire, Au/sapphire, and Au/VO_2/sapphire . . . 56
4.4. The changes in transmission with bias assistance for Au/VO_2/ITO . . . 57
4.5. SMT signal as a function of bias voltage . . . 58
4.6. The electron band diagram of Au/ VO_2 for ohmic contact . . . 59
4.7. Schematic band diagram change of Au/VO_2 . . . 61
4.8. Al/Si electron diffraction . . . 63

5.1. Relative reflectivity changes as a function of the time delay for Si, CsI, NaCl and KI . . . 67
5.2. Spectroscopic time-resolved reflectivity changes in CsI . . . 68
5.3. Experimental setup for the ion measurement . . . 69
5.4. Yield for the detection of positive and negative ions . . . 71
5.5. Interferometer images of CsI and Si samples . . . 72
5.6. Micrographs of the craters on KI . . . 73
5.7. Absorbed pump energy for NaCl, CsI and KI . . . 75
5.8. Substrate preparation for KI samples . . . 77
5.9. XRD and rocking curve of KI samples . . . 77
5.10. Typical electron diffraction pattern from KI samples . . . 78
5.11. XRD and rocking curve of CsI samples . . . 79
5.12. The profiles of the single-shot diffraction patterns from KI . . . 80
5.13. Time-dependent electron diffraction intensity changes from 50-nm thick KI 81
5.14. Time-dependent electron diffraction intensity changes from 100-nm thick KI 82
5.15. Comparison between the time-dependent electron diffraction intensity changes and time-dependent reflectivity changes of KI . . . 84
5.16. Optical reflectivity change for CsI and NaCl with high resolution . . . 85
5.17. Potential surface energy of NaCl molecule . . . 86

6.1. Nanosecond timing scheme for REGAE . . . 90
6.2. Single-shot electron diffraction of gold melting . . . 91

6.3. Correlation of the electron energy to the time of flight at the sample position (ASTRA simulation) 92
6.4. Principle of a streak camera 93
6.5. Schematic drawing of REGAE ponderomotive setup 95
6.6. Ponderomotive scattering simulated by ASTRA (ASTRA simulation) 96
6.7. Laser power dependence of the ponderomotive scattering (ASTRA simulation) 96

7.1. Radially averaged intensity profile of Al diffraction 100

List of Tables

2.1. Characteristics of the Ti:sapphire oscillator 9
2.2. Characteristics of the Ti:sapphire amplifier 10
2.3. Autocorrelator deconvolution factor 12
2.4. Beam stability measurement 19

4.1. Lattice parameters of VO_2 51
4.2. The measured reflection and transmission from the sample (VO_2/sapphire, Au/sapphire, Au/VO_2/sapphire, and Au/VO_2/ITO) 53
4.3. The calculated absorbed laser intensity of each sample (VO_2/sapphire, Au/sapphire, Au/VO_2/sapphire, and Au/VO_2/ITO) 54

5.1. Crater depth in Si, CsI, NaCl and KI samples 74

A.1. Parameters for ASTRA simulation 103

1. Introduction

The world is dynamic. Every phenomenon can be characterized by a certain time scale. Natural processes vary from the very slow motion of the continental drift to the very fast motion of forming hydrogen-oxygen covalent bonds in the human body. To advance our knowledge of the fundamentals governing the atomic motions, it is necessary to have a "molecular camera", which has the ability to both "see" atoms and "capture their pathway". Picturing how atoms move relative to one another could visualize, for example, a bond breaking in a chemical reaction, DNA unwinding or the simple structural transformation as matter goes from one state to another. The development of field ion microscopes, electron microscopes and scanning probe microscopes enables the direct observation of atoms in real space. However, such static pictures of matter contain no information about the dynamics. In the atomic world, the typical time scale for bond breaking is about 100 femtosecond (fs). Therefore, a camera with a fs shutter and atomic resolution is required to reveal the process.

Time-resolved techniques provide the possibility to capture the fs dynamic changes. In these processes, a fs pump laser triggers the fast dynamic change by optical excitation, and a fs probe (laser, X-ray or electron pulse) captures the dynamic process with a fs gate. The detector itself is much slower than the probe pulse (typically in seconds). So for each time point only one snapshot can be recorded. To obtain a time lapse series, many snapshots should be captured with different delays between the initiation of the process and the probe pulse.

Optical pulses are now available in the attosecond range and can be used for probing the ultrafast chemical reactions. However, atomic structure cannot be visualized directly by laser pulses due to its wavelength, which is three orders of magnitude longer than typical atomic distances. Hard X-rays and electrons that have wavelengths of about 1 Å or less are able to interfere with the atomic structure. Combining the spatial resolution of diffraction techniques with the temporal resolution of pump-probe techniques gives us the possibility to directly observe atomic motion in real time. The development of advanced fs X-ray and electron [1–10] sources opens unprecedented opportunities for the investigation of complex phenomena on the atomic time scale. In the last few years, enormous progress has been made towards achieving this goal, using ultrafast laser excitation pulses to trigger structural changes and either X-ray or electron probes to follow the induced atomic motions.

The comparison between electron and X-ray diffraction is not straight forward. Both have their own merits and shortcomings [11]. X-ray is a form of electromagnetic radiation. Atoms scatter X-ray waves primarily through the atoms' electrons. Electrons, on the other hand, are scattered by the electric potential, which is formed by both the electrons and nuclei of the sample. From the perspective of this thesis work, we have chosen electrons over X-ray as the fast probe, benefiting from more than ten years experience in developing the femtosecond electron diffraction (FED) systems

in the Miller group. There are a few main advantages for electrons over X-rays. First, the mean free path of the electrons in solids well matches the optical absorption depth, which enables homogeneous excitation. In contrast, X-rays have much larger penetration depth than the optical excitation, which requires a grazing incidence. However this leads to a loss in time resolution due to a pulse front tilt of X-ray. Second, the FED experiments are of "tabletop" scale and therefore more flexible. In addition, the fs X-ray sources are limited due to their large size, costly operation, and limited access. Third, electrons introduce less damage to specimens than X-rays. For instance, in biological samples the deposited energy by inelastic scattering is 1000 times higher for X-rays than that for electrons per elastically scattered electron/X-ray. For X-ray probe pulses, the radiation damage problem is also more of an issue for time-resolved experiments as the sample diffraction changes with the number of shots. The main challenge for using electrons is the space-charge broadening effect that limits the electron pulse duration, however, with the development of the new electrons sources, electrons are even catching up to generate comparable bunch length with X-ray sources in the sub-100 fs range [12].

1.1. Basics of electron diffraction

The first electron diffraction was performed by Davisson and Germer in 1927, which provides the first direct confirmation of de Broglies wave theory of matter. Since then, electron diffraction has been widely used and become an important tool for studying crystal and molecular structures.

When an electron passes along an atom it interacts with the atom's nucleus due to the Coulomb force, leading to scattering of the electron. The scattered waves are generally out of phase, and give zero intensity when added together. For certain scattering angles, however, the scattered waves are in phase, which forms constructive interference. The diffraction patterns bring immediate information about the type of the material, crystallinity, cell parameters, symmetry, etc.

The simplest way to derive the condition for constructive interference from a crystal is devised by W. Bragg. The scattering of the electrons by crystals can be described as a reflection of the beams at the lattice planes. When the Bragg condition is satisfied: $n\lambda = 2d_{hkl}\sin\theta_{hkl}$ (where θ_{hkl} is the Bragg angle, d_{hkl} is the interplanar spacing), the electron waves interfere constructively. By measuring the spacing between spots and diffracted angle $2\theta_{hkl}$ it is possible to determine the crystallographic orientation and the type of material. In the simplest case (Fig. 1.1), considering the small Bragg angles occurring with the transmission electron diffraction ($2\sin\theta_{hkl}=r_{hkl}/L$, where L is the distance between the sample and the detector and r_{hkl} is the measured distance between the Bragg spot (hkl) and the direct beam (000)), we can write the Bragg equation in a different way: $d_{hkl} = \frac{\lambda L}{r_{hkl}}$, which gives us the direct lattice parameter. In our electron diffraction setups, in order to increase the signal to noise ratio and match the detector size, solenoids are used to focus the electron beam to get sharp images on the detector. A careful calibration of the system is also required. For this purpose, silicon is chosen as a standard material since it has a well known structure and is routinely fabricated to even highest quality. It can be used to calibrate the magnification of the solenoid,

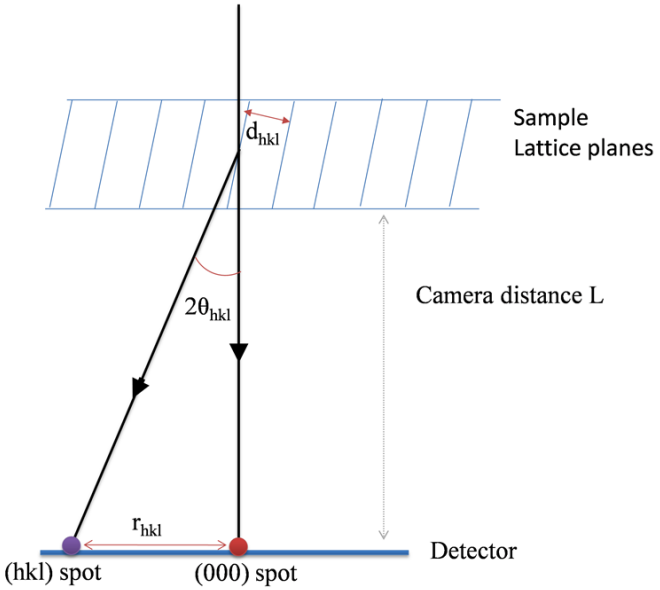

Figure 1.1: Schematic of electron diffraction: d_{hkl} donates the interplanar spacing, θ_{hkl} is the Bragg angle, L is the distance between the sample and the detector and r_{hkl} is the distance from a Bragg spot (hkl) to the direct beam (000).

camera constant, diffraction pattern rotation, etc.

The Bragg peaks are usually spots in real space for single crystals. Each spot corresponds to a different set of crystallographic planes in the crystal. The angles between diffraction spots are the same as the angles between corresponding directions in the crystal. For powder samples, however, which are composed of many tiny single crystals randomly oriented, the r_{hkl} vectors exist on a cone of scattering. Whenever Bragg's law is satisfied, we get a diffraction peak. Since there is usually some crystallite that has its planes orienting in the proper direction, we get a cone of constructive scattering with the Bragg angle 2θ.

Amorphous materials do not consist a long range order and hence the atoms are not arranged in ordered lattices, but instead are completely disordered. We can not resolve any discrete spots, and the diffraction pattern consists, if at all, of diffused rings on a consequence of some short range ordering.

Figure 1.2(a) shows the typical electron diffraction pattern from a single crystalline silicon (diffraction obtained from the compact electron gun), with dots represent the diamond cubic (Fd3m) structure of silicon. Due to the normal incidence of the electron beam on the <001> direction oriented film, the (111) plane peak is absent from the diffraction pattern. Figure 1.2(b) gives the diffraction pattern obtained from a polycrystalline gold (diffraction obtained from relativistic electron gun), with rings corresponding to the (111), (200), (220), (311), and (222) planes reflection of the face-centered-cubic (fcc) structure of gold.

A main challenge in electron diffraction is the preparation of electron-transparent

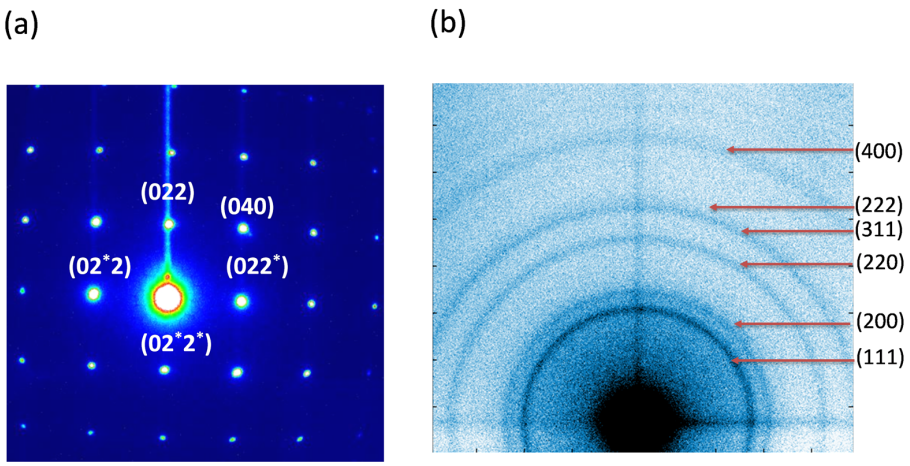

Figure 1.2: Diffraction pattern of single crystalline silicon crystal in <001> zone axis orientation, obtained with the compact electron gun (a), and polycrystalline gold obtained with the relativistic electron gun (b).

samples, which have to be so thin that enough electrons can get through without being absorbed to form a diffraction pattern. The thickness of a typical sample should be on the order of the electron elastic mean free path given by:

$$\Lambda_e = \frac{1}{N\sigma_e} \tag{1.1}$$

where N is the number density of atoms, and σ_e is the elastic scattering cross-section. Figure 1.3 shows the calculated elastic mean free path for gold and silicon.

Typical solid state sample thicknesses for FED experiment are in the order of tens to hundreds of nanometers depending on the material properties and electron beam energy. The sample surface should be big enough as FED electron beams are typically a few hundred micrometers in diameter. Many methods including vapor deposition, microtoming, chemical etching, ion milling, sputtering, etc. are used to prepare FED samples.

1.2. History of time-resolved electron diffraction

Electron diffraction is most frequently used in solid state physics and chemistry to study the crystal structures. The periodic structure of a crystalline solid acts as a diffraction grating, scattering the electrons in a predictable manner. Working back from the observed diffraction pattern, the structure of the crystal can be retrieved.

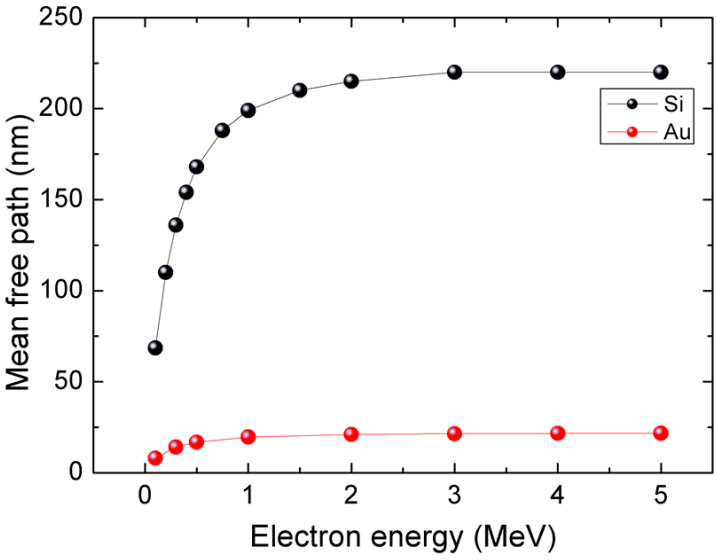

Figure 1.3: Calculated elastic mean free path for different materials with electron energy from 100 keV to 5 MeV. Adapted from Dr. Taisuke Hasegawa's private calculation.

Femtosecond electron diffraction (FED) provides the ability to "see" and "freeze" the atom movements during a phase transition and capture the frames with atomic resolution.

In the early 1980s, Williamson and Mourou at the University of Rochester started the development of time-resolved electron diffraction based on an optoelectronic streak camera [13]. The whole setup provided ~20 picosecond (ps) timing resolution. The first reported study was directed to the laser induced melting of Al [14]. It is now apparent that Debye-Waller effects and lattice heating misled the structural dynamic. However, this work illustrated the basic instrumental concept and recognized the potential of the technique. A variation on this setup that operates in reflection geometry – Reflection high-energy electron diffraction (RHEED) was introduced by Elsayed-Ali and Mourou [15]. It was further extended to gas electron diffraction by Zeweil group at Caltech [16,17]. This was the first use of a fs laser to drive the photoemission. Due to Coulomb repulsion (space-charge effect), the early setup was limited to a time resolution of a few picoseconds. The first attempts to solve this problem were based on either the use of low-density electron pulses [18–20] or shorter electron drifting time [21–23]. In principle the number of the electrons can be reduced to ~1 if the sample is fully reversible. However around 10^6 electrons are needed to record a decent diffraction pattern [24]. Frequent sample exchange or accumulated heating due to the excitation laser is very challenging for the whole experiment, especially for investigating strongly correlated materials [6–8]. Compact electron sources [21–23] were proposed by the Miller group at the University of Toronto, in which the space-charge induced pulse duration broadening is minimized by shorter propagation distance. With this setup

they performed the first study of structural changes under strongly nonreversible excitation conditions with sub-ps time resolution [6]. However, these techniques were still limited to a few hundred fs time resolution. Until recently, the development of relativistic electron sources and radio frequency (RF) rebunching cavity have made it possible to suppress space-charge effect and compress the bunch length to sub-100 fs range [9, 10, 12, 25, 26].

1.3. Thesis outline

Since the commissioning of the femtosecond electron diffractometer in our group, the first reported study is directed to the laser induced melting of Al [6] with a 30-keV electron source. Following this initial work, a number of other systems have been explored for different elements with different band structures. Figure 1.4 shows the effect of strong electronic excitation on the interatomic potential energy surface (PES) in elemental materials that have been studied by FED. In silicon, it was the first time to directly observe electronically induced nucleation centers [27, 28]. When 10% of the valence electrons are excited it drives the system into an antibonding condition, which takes the system to a rapidly fluctuating liquid potential energy surface (Fig. 1.4(b)). In contrast to the photoinduced bond softening in semiconductors, gold experiences an opposite effect [29]. The rate of disordering of the gold lattice is retarded with strong optical excitation, which is an indicative of increased lattice stability (Fig. 1.4(c)). Bi is a strongly correlated system. Upon photoexcitation, the PES minimum shifts that leads to the excitation of large-amplitude coherent acoustic phonons (Fig. 1.4(d)). Recently, the first investigation on organic material was done with a 95 keV FED setup, which shows photo-induced insulator-to-metal phase transition [30].

However, those studies were still limited to a time resolution of around 500 fs. In order to further improve the time resolution and resolve even faster chemical reactions, we were developing the new generation of electron guns within the Miller group at the University of Hamburg – a compact FED system (Egun300) that can provide an electron energy up to 150 keV and the relativistic MeV electron source (Relativistic Electron Gun for Atomic Exploration – REGAE). This thesis reports on the development of these two FED systems as well as one optical pump-probe setup for pre-characterization of the sample. The first experiments on studying phase transitions with these setups are also discussed.

In chapter 2 the laser system, which is one of the most important parts for a time-resolved electron diffraction setup, will be discussed. The chapter starts with describing the basic parameters of a commercial laser system and will introduce two characterization setups (Autocorrelator and Frequency-resolved optical gating (FROG)). A few nonlinear processes (THG, NOPA) will also be discussed for generating specific wavelengths, which are important for sample excitation and electron generation. To study the dynamic processes we have to know first the electronic properties of the sample, especially the damaging threshold and spectroscopic properties. For this purpose, an optical pump-probe system for studying material properties is developed and discussed in the last section of this chapter.

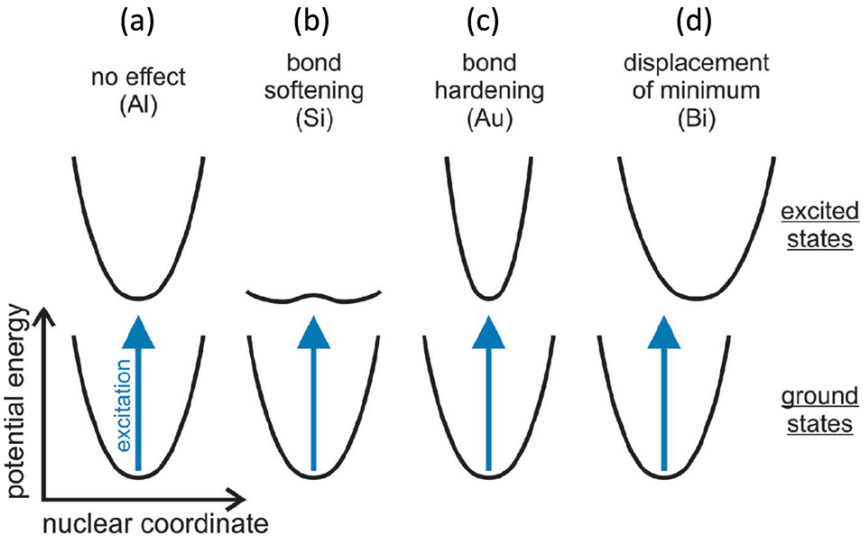

Figure 1.4: Schematic illustration of the possible effects of strong electronic excitation on the potential energy surfaces of different materials. Adapted from [31].

In chapter 3 two time-resolved electron diffraction systems (Egun300 and REGAE) are described. Egun300 is a compact FED setup with table-top size and very flexible operation. On the other hand REGAE is a 10 meter system. It provides much higher electron energy in the range of 3–5 MeV, which enables investigation of thicker samples and provides much shorter bunch length.

Chapter 4 describes the first optical pump-probe experiment using hot electrons to induce phase transitions in Vanadium dioxide (VO_2). In contrast to a general femtosecond pump-probe experiment, the phase change is driven by the electrons and the laser beam is used as the probe. A bias voltage is also applied to elucidate the contribution of photo induced hot electrons. Further application with electron probe and hot electron driven phase change on Al/Si multilayer is also proposed.

Chapter 5 will discuss the first FED experiment using the new diffractometer. All previously reported FED studies in our group were based on metal, semiconductor or organic materials that have a delocalized electron system. It would be very interesting to pursue the underlying system with localized electrons like alkali halides. Single-shot time-resolved optical reflectivity, ion measurement, surface crater observation and femtosecond electron diffraction are applied to investigate the evolution of the ablation process that follows strong fs-UV-laser excitation in single crystalline alkali halides.

Chapter 6 mainly talks about characterization of REGAE. It includes finding the time zero position, which is the relative timing difference between the electrons and the laser beam, and measuring the electron bunch length. A preliminary experiment has been performed by melting gold to determine the time zero in the sub-picosecond range. A further ponderomotive scattering study based on A Space Charge Tracking Algorithm (ASTRA)[1] [32] simulation is also proposed to measure sub-100 fs bunch length for relativistic electron sources.

In the final chapter, a summary of the main findings are presented, along with a perspective for the future developments.

[1] ASTRA is used for both Egun300 and REGAE throughout the whole thesis for all beam dynamic simulation. The detail parameters and setting can be seen in Appendix A.

2. Femtosecond laser system

One of the main elements for ultrafast electron diffraction is the laser, which is the driving force to generate pulsed electron bunches via photoemission, and the trigger to induce the phase transition of the sample under study. This chapter mainly describes the laser system and related parts. In addition a home-made optical pump-probe spectroscopy system, which is an essential tool for characterizing the sample properties, is discussed in the last section.

2.1. Ti:sapphire laser system

The laser is a commercial Coherent Elite Duo system [33] that generates pulses with a center wavelength of 790 nm, an energy of 8 mJ per pulse and a duration of 40 fs at 1 kHz. It consists of an oscillator (Micra-5) and a laser amplifier (Legend Elite Duo) for boosting the output power.

2.1.1. Oscillator (Micra-5)

Micra-5 is a Ti:sapphire laser oscillator capable of producing mode-locked pulses with a bandwidth exceeding 60 nanometers. It provides the seed laser source for further regenerative amplification. It has a good power stability (<1%) due to the use of power track beam steering technology. Micra-5 is pumped by Coherent Verdi, which is a continuous-wave green laser allowing for efficient absorption by the Ti:sapphire crystal. It uses a passive modelocking technique to generate an intense mode-locked laser beam. Table 2.1 lists the main characteristics of Micra-5. 95% of the laser power is sent to the laser amplifier for further amplification. The remainder is used for synchronization (described in section 2.2.3) and diagnostics.

Parameter	Value
Pump power	4.5 W
CW output power	300 mW
Mode-locked output power	360 mW
Repetition rate	83 MHz
Central wavelength	795 nm
Spectral width	80 nm
Pulse width	12 fs (FWHM)

Table 2.1: Characteristics of the Ti:sapphire oscillator.

2.1.2. Laser amplifier

In order to get the best amplification efficiency through pump laser (Evolution) and gain medium (Ti:sapphire), Chirped Pulse Amplification (CPA) technique [34–38] is used with the laser pulse being stretched out temporally prior to amplification to avoid damage. The seed laser is stretched by a grating pair stretcher and then sent to a regenerative cavity (REGEN) for strong amplification. The REGEN uses multiple passes through the gain medium by placing the gain medium in an optical resonator, together with an optical switch, consisting of an electro-optic modulator (Pockels cell), a $\lambda/2$ waveplate and a polarizer. From the technical viewpoint, the Pockels cells are the only electronic parts in the laser cavity that introduce most of the noise and fluctuations. We requested a custom-made solid metal housing, and replaced the high voltage Pockels cell driver adapter with home-made copper holder for better cooling compatibility and stability of the system.

After the REGEN, the beam passes through a single pass amplifier. The gain medium is also Ti:sapphire crystal and the pump is from the same Evolution. The amplified laser power can reach to 10 W. But the pulse is highly chirped and has a duration of a few hundred picoseconds. The dispersion is compensated by a grating compressor to achieve nearly transform limited femtosecond pulses. Table 2.2 summarizes the most important characteristics of the amplifier.

Parameter	Value
Pump power	40 W
Output power	8 W
Repetition rate	1 kHz
Central wavelength	800 nm
Spectral width	25 nm
Pulse width	40 fs FWHM

Table 2.2: Characteristics of the Ti:sapphire amplifier.

We employ an additional water cooling system integrated in the optical table to reduce temperature fluctuations for a better performance of the laser output and stability. On top of a commercial Newport optical table, there is honeycomb water cooling system and another layer of aluminum breadboard. Figure 2.1 shows the temperature change over 24 hours. After thermalisation, the temperature is stable within 0.1 degree, which is equal to the resolution of the temperature monitor.

2.1.3. Characterization

For sub-100 fs laser pulses, the measurement of the temporal pulse shape is not directly possible with electronics. The most common way is to use the combination of a mechanical scan of optical delay and a nonlinear optical measurement to convert from the fs range to ms or slower rates, which can be easily measured with conventional electronics. Examples are Autocorrelator, FROG, Spider, IAC [39–42].

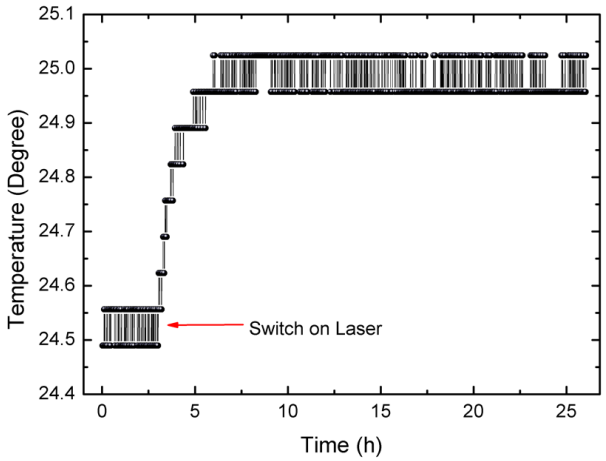

Figure 2.1: Temperature change over 24 hours on the optical table.

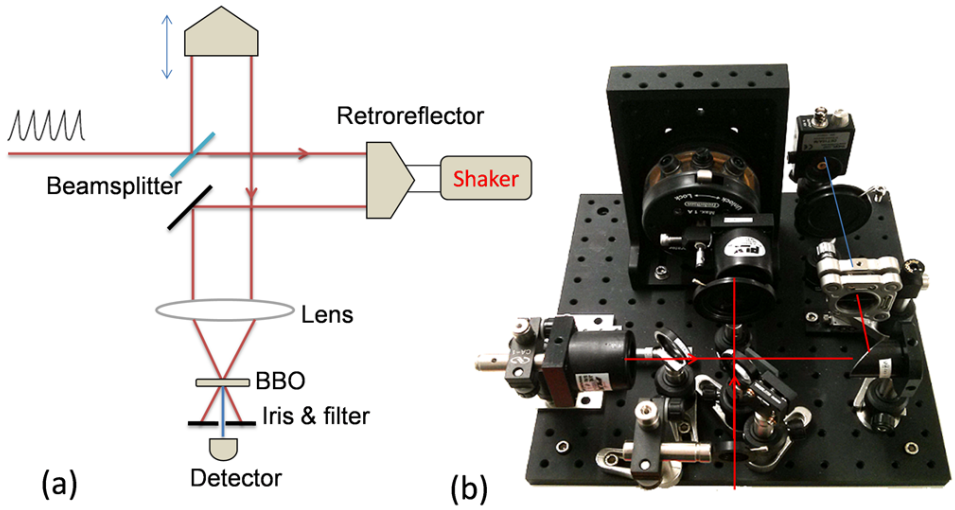

Figure 2.2: Layout of an autocorrelator. The laser beam is split into two. One arm is sent to the retroreflector with a low frequency shaker and the other one is sent to a delay line for balancing the two arms. They overlap on the BBO crystal and generate the signal pulse (a); Photo of the home-made autocorrelator (b).

The second harmonic (SH) autocorrelator is the simplest way for such a measurement. Figure 2.2 (a) presents the configuration of a SH autocorrelator. The pulse to be measured is split into two beams and after two delay lines they overlap again on a nonlinear crystal. One arm is for balancing the two arms. The other one contains a low frequency shaker that changes the optical path. The second harmonic generation (SHG) field has an intensity that is proportional to the product of the intensities of the two input pulses:

$$I_{\text{sig}}^{\text{SHG}} \propto I(t)I(t-\tau). \tag{2.1}$$

where I(t) is the time dependent optical power. The shorter the pulses are, the faster the autocorrelation signal will decay when τ is increased. For a known temporal pulse shape, the pulse duration is a certain factor times the measured width of the autocorrelation signal. Table 2.3 lists the factor for different pulse shapes.

Pulse shape	Deconvolution factor
sech^2	0.647
Gaussian	0.707
Rectangular	1
Triangular	0.692

Table 2.3: Deconvolution factors for different pulse shape.

Figure 2.2(b) shows our home-made autocorrelator. The optics are designed for visible wavelength with aluminum coated retroreflector and mirrors. The BBO crystal has a cutting angle of θ_{BBO} = 40 degrees, ϕ_{BBO} = 90 degrees and a thickness of 20 μm. By adjusting the phase matching angle of the BBO crystal, the setup is suitable for measuring wavelength from 500 to 800 nm.

In the above-mentioned method, the autocorrelation trace is measured using different pulses with different time delays. In contrast, it is also possible to measure a complete autocorrelation trace with a single pulse. Single-shot autocorrelation is based on crossing the beams at a large angle in a nonlinear crystal [42–44]. It converts the temporal distribution of the pulse to the spatial domain. Afterwards, a detector that consists of a photodiode array is used to record the autocorrelation signal.

Autocorrelators are relatively easy to control and align compared with other diagnostics. It provides on-the-fly pulse duration characterization. This enables the possibility to correct long-term drift in the pulse duration by carefully adjusting the laser compressor.

As autocorrelation related techniques yield little information about the pulse especially the unavoidable ambiguity in the direction of time, other techniques like FROG, SPIDER etc have been developed that allow people to measure the complete intensity and phase versus time of an ultrashort laser pulse.

FROG (Fig. 2.3) involves gating the pulse with a variable delayed replica of itself in an instantaneous nonlinear-optical medium and spectrally resolving the gated pulse with a set time delay. The process creates a spectrogram of the pulse. It can be used to determine the complex electric field of the laser pulse. A FROG trace can even visually

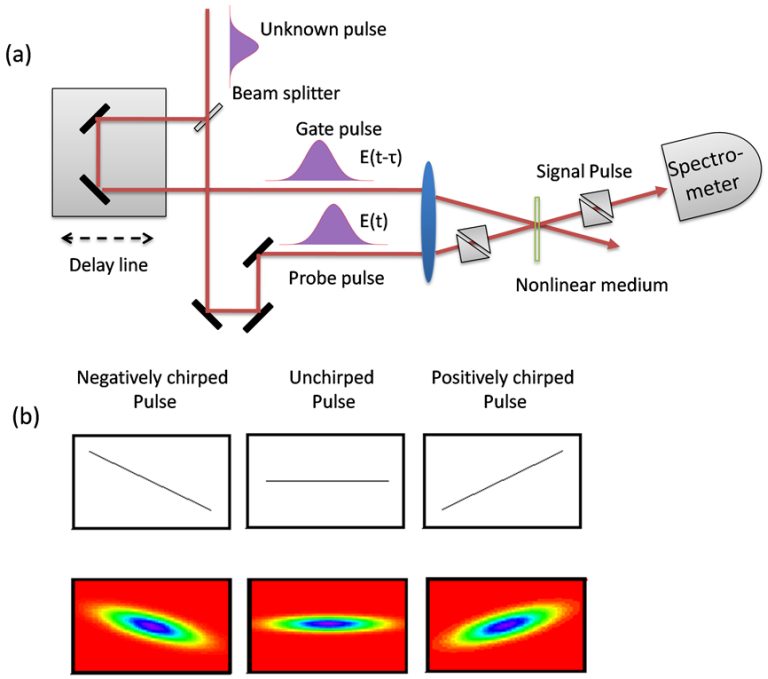

Figure 2.3: (a) Schematic of polarization gating PG-FROG. The spectrum of the nonlinear mixing product of the two beams is measured as a function of the relative time delay. (b) Measured PG-FROG trace with related chirp. Adapted from reference [45].

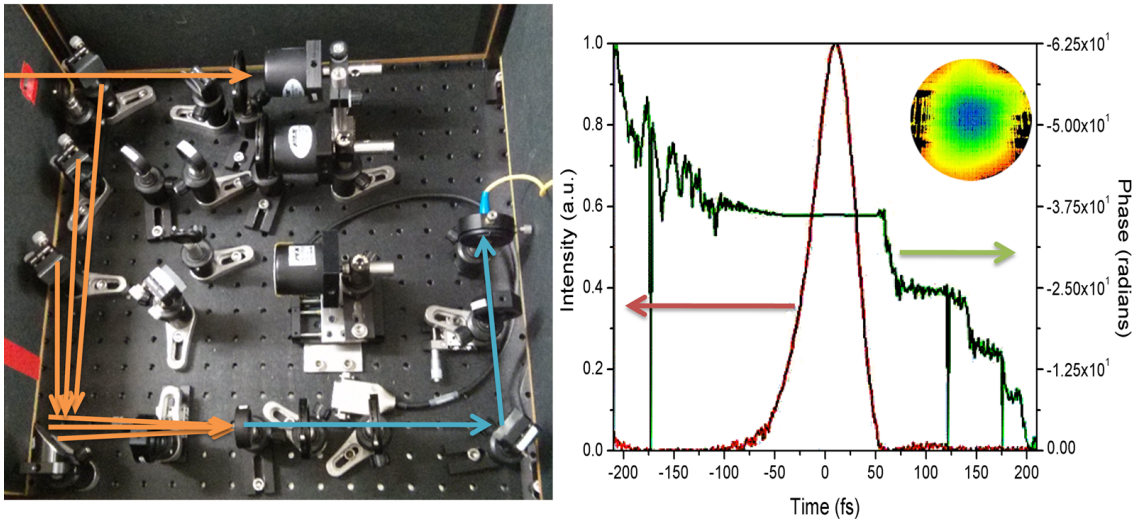

Figure 2.4: Home-made TG-FROG setup and retrieved FROG trace (FROG Demo [46]) with a pulse duration of 40 fs and zero chirp.

reveal the pulse frequency versus time. Figure 2.3 (b) shows a schematic example of the chirped information from a polarization gating (PG)-FROG scan.

The FROG spectrogram is a graph of intensity as a function of frequency ω and delay τ. The typical expression for a FROG trace from the nonlinear interaction is:

$$I_{\mathrm{FROG}}(\omega,\tau) = \left| \int_{-\infty}^{\infty} E(t)g(t-\tau)\exp(-i\omega t)dt \right|^2 \tag{2.2}$$

where $E(t)$ is the original pulse field, $g(t-\tau)$ is the gated nonlinear process. With sophisticated inversion the full information of the pulse can be retrieved. The theory is somewhat complex, but has been well developed by Rick Trebino's group and is commercially available from Femtosoft [46].

There are also different versions of FROG methods [39]. The four main FROG variants are SHG, self-diffraction (SD), PG, third-harmonic generation (THG). Further development also includes XFROG [47,48], Single-shot FROG [49], TG-FROG [50], GRENOUILLE FROG [51], etc.

Figure. 2.4 (a) shows a home-made transient grating FROG (TG-FROG) [50]. TG-FROG is based on $\chi^{(3)}$ nonlinearity that is background-free and can be used in the deep UV with proper optics. It has no ambiguities in the direction of time. However, it has a three-beam geometry, requiring that the input pulse is split into three pulses. Two of the pulses are overlapped in time and space at the optical-Kerr medium that produces a refractive-index grating. The third pulse is variably delayed and overlapped in the medium and is diffracted by the induced grating to produce the signal pulse. A measurement of our Ti:sapphire laser and the retrieved 40 fs pulse duration and zero chirp is presented in Fig. 2.4 (b).

2.2. Laser setups for FED systems

2.2.1. Photocathode laser setup in FED systems

In the FED setup the pulsed electron generation via photoemission is an optical excitation of electrons from the valence band into the higher empty states in the conduction band. Those electrons that have enough excess energy will overcome the work function and escape into the vacuum. To get short electron bunches femtosecond laser systems are typically used. We use 266 nm UV laser for both Egun300 and REGAE.

Third harmonic generation

Part of the IR laser beam is used to generate the UV light that is necessary to illuminate the photocathode. This is done via THG [52,53], more specifically: SHG and subsequently sum frequency generation (SFG). Figure 2.5 shows the configuration of THG by using two BBO crystals. It is also possible to use a single BBO crystal to generate the THG but with limited efficiency [54].

In the presented scheme, first of all the beam diameter is reduced to increase the peak intensity to the level needed for harmonic generation, which is around 100 GW/cm^2.

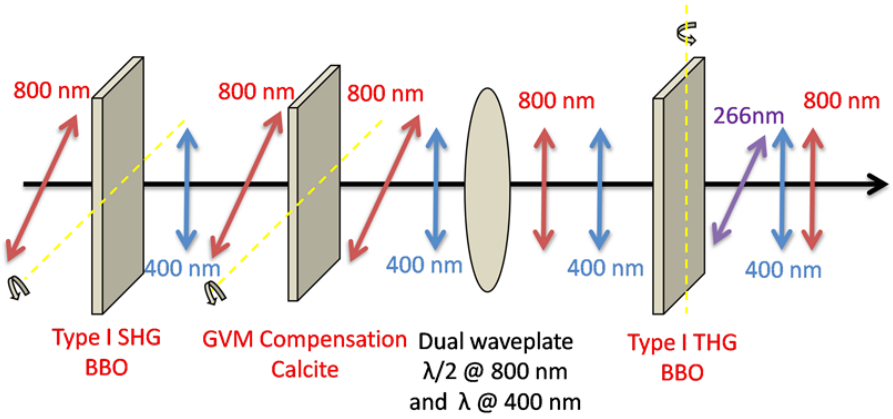

Figure 2.5: Schematic drawing of THG generation based on type I phase matching. The first BBO crystal is used for SHG. Calcite window compensates the GVM between FH and SH. A waveplate rotates the polarization of FH and SH. THG is generated in the second BBO crystal.

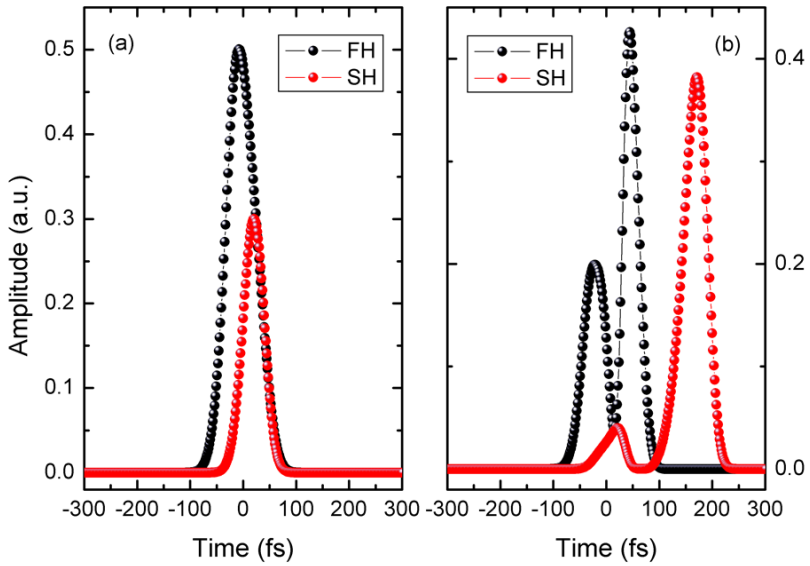

Figure 2.6: Calculated SH and FH with different crystal thickness (Nonlinear crystal: BBO, FH: 800 nm, SH: 400 nm). Crystal thickness (a) 0.2 mm and (b) 1 mm.

As the fundamental (FH) beam has a broad bandwidth (∼30 nm) it is crucial to use a thin crystal for achieving broad phase matching bandwidth and keeping short pulses. Essentially, this means that a constant phase relationship between the interacting waves is maintained along the propagation direction. Under the slowly-varying envelope approximation (SVEA), the one-dimensional coupled-wave equations would help to understand the whole process numerically [55, 56] (detail simulation methods are described in Appendix B). Figure 2.6 shows the calculated SHG with different crystal thickness. With a thicker crystal we can get higher SHG efficiency (partially comes from the satellite) but a longer walk-off and a deformed FH, which will negatively affect THG. Therefore, The thickness of the BBO crystal for SHG was chosen to be 200 μm with the cutting angles of θ_{SHG} = 29.2 deg., ϕ_{SHG} = 90 deg.

The FH and SH have different optical frequencies and polarization. When they propagate in the BBO crystal, their group velocities are different. FH is moving faster than SH, which is also shown in Fig. 2.6. This effect is bigger with increasing medium length. In order to compensate the group velocity mismatch (GVM) between FH and SH after second harmonic generation, a 1 mm thick calcite window with a cutting angle of $\theta_{calcite} = 45^{\circ}$ is used to adjust the GVM. Calcite crystal is a negative uniaxial crystal and is well-known for its high birefringence. After SHG, the FH and SH have different polarizations, therefore the calcite crystal makes the FH walks slower than the SH. Rotating the crystal can fine tune the GVM between FH and SH due to their different changing speed of group velocity in calcite crystal.

THG can be classified into Type I and Type II phase matching, which means that the polarization of FH and SH is either parallel (Type I) or perpendicular (Type II) to each other. We choose the BBO crystal with Type I phase matching as it has a larger phase matching bandwidth (two times larger) and nonlinear coefficient (0.60 d_{11} compared with 0.17 d_{11} for Type II). In addition, the spectral acceptance, which is determined by the wave vector mismatch Δk, is much bigger for Type I (1.9 nm) compared with Type II (0.1 nm). Therefore we have chosen Type I phase matching for THG. To maintain a good phase matching bandwidth and conversion efficiency, the thickness of THG crystal (BBO) was chosen to be 100 μm with θ_{THG} = 44.3 deg. and ϕ_{THG} = 90 deg. The overall design maintains a good conversion efficiency (10%) and a short pulse duration, which are very important for generating bright femtosecond electron bunches (see Chapter 3).

Photocathode laser for REGAE

In order to optimize the performance and achieve a more convenient operation for the relativistic electron gun, it is important to fully control the spatial and temporal profile of the UV excitation laser on the cathode. Figure 2.7 shows the basic layout for our UV photoexcitation laser setup that contains a beam stabilizer, THG, a prism-pair Stretcher, a pulse shaper, a cross-correlator, a monitoring CCD and a photodiode.

The photocathode of REGAE is about 10 meters away from the output of the Coherent laser system and placed on another floor. We use a periscope to propagate the laser beam. In order to get good pointing stability, we have to make sure that the laser beam in the total beam line is stable. As the temperature difference between the laser room and the REGAE tunnel is more than 10 degrees, there is a strong air drift if

the laser beam is propagating in free space. The periscope for propagating the laser beam is vacuum compatible, which prevents the air drift and increase the stability. In order to improve the stability, after the periscope we have implemented a beam stabilizer. It has two motorized mirrors and two cameras to monitor the beam position. Automatic correction is done through computer control by monitoring the pointing of the laser beam and then steering the motorized mirror mount with a closed-loop feedback. Figure 2.8 shows the long term beam stability measurement in horizontal (X) and vertical (Y) direction. There is clear improvement of the beam stability when the beam stabilizer is turned on. Table 2.4 gives the statistic values of the measurement.

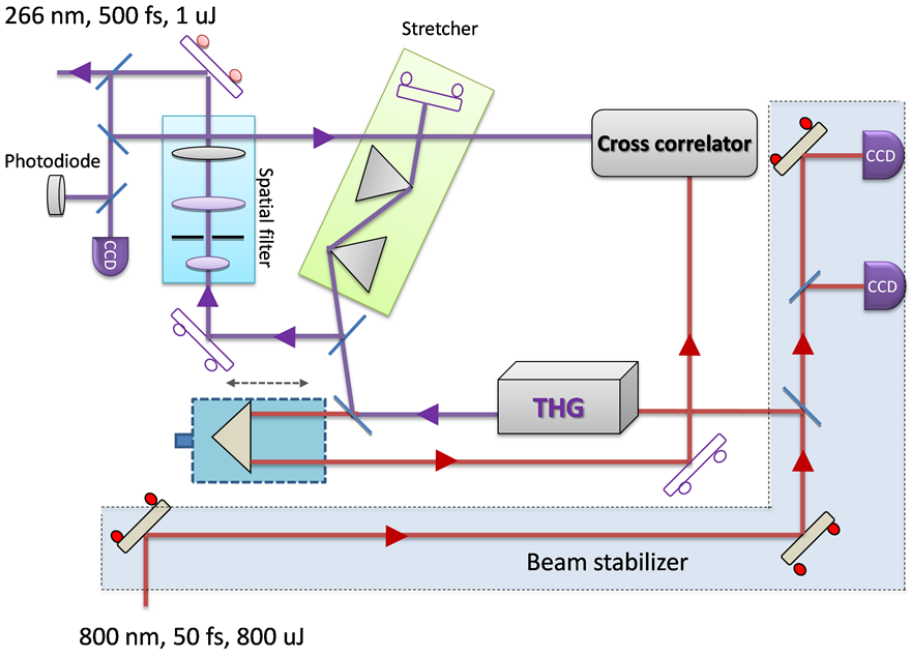

Figure 2.7: Layout of the excitation laser setup for the photocathode of REGAE. It includes beam stabilizer, THG, spatial and temporal filter, cross-correlator, and cathode monitoring system.

REGAE THG is generated as described in Fig. 2.5. In addition, we used a prism pair to build the stretcher for a better control of the pulse duration. By tuning the distance between the prism pair the total group velocity dispersion (GVD) added onto the UV beam can be adjusted, which gives us flexibility to tune the pulse duration between 100 fs to 1.5 ps FWHM. For the initial commission of REGAE a longer UV pulse helped find the electron beam. Afterwards we could tune the pulse duration for better performance and different purposes as illustrated in Fig. 2.9, a simple change of pulse duration will lead to the change of both the bunch length and the transverse emittance.

To measure the pulse duration of THG, a cross-correlator has been built for simple

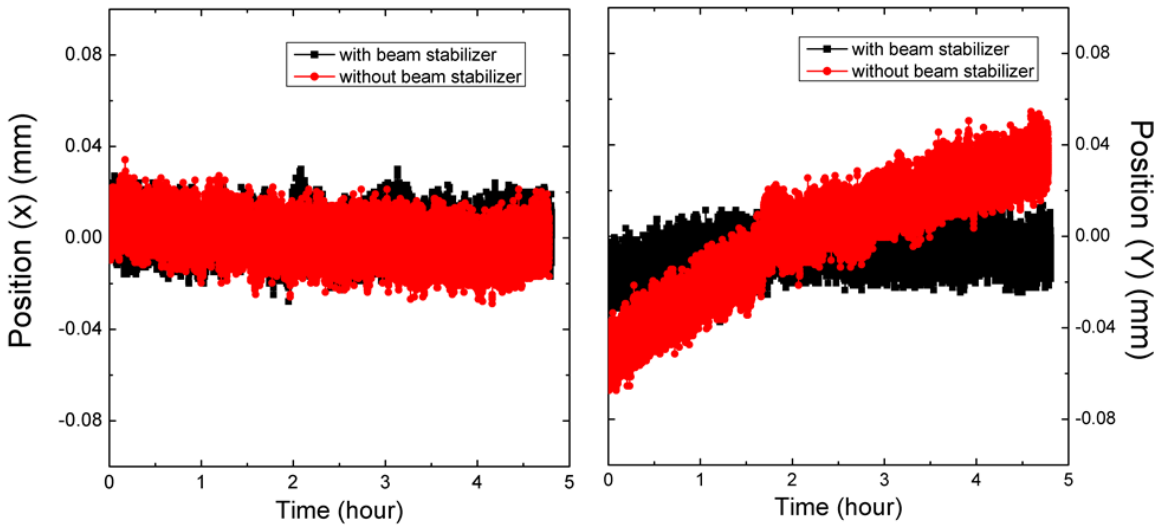

Figure 2.8: Laser beam pointing measurement with and without the stabilizer for 5 hours measurement in the horizontal (X) and the vertical (Y) direction.

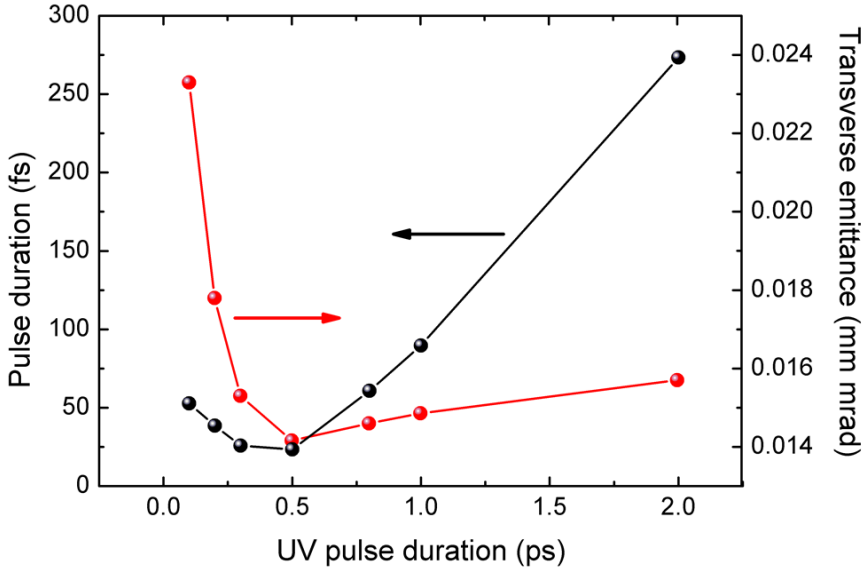

Figure 2.9: Electron bunch length and transverse emittance at the sample position as a function of UV pulse duration. ASTRA simulation based on REGAE, see Appendix A.

Without stabilizer	X (rms)	Y (rms)
5 hours drift	50 um (ϕ 10 mm) 100 nm (ϕ 20 um)	240 um (ϕ 10 mm) 480 nm (ϕ 20 um)

With stabilizer (5 h)	X (rms)	Y (rms)
5 hours drift	50 um (ϕ 10 mm) 100 nm (ϕ 20 um)	60 um (ϕ 10 mm) 120 nm (ϕ 20 um)

Table 2.4: Beam stability measurement for 5 hours, ϕ 10 mm and ϕ 20 um corresponding to different beam diameter.

and fast online detection. The residual 800 nm from THG is used as the probe to measure the stretched 266 nm beam. Figure 2.10 shows the cross correlation signal with a pulse duration of 1 ps (FWHM) and a very clean beam with no pre- and post-pulses within the 50 ps range.

Temporal profile of the UV laser for REGAE photocathode The ability to manipulate the laser pulse striking the photocathode would allow us to control the properties of electron bunches [57]. A flat-top intensity distribution in both the transverse and longitudinal dimensions could produce lower transverse emittance than the ordinary Gaussian laser pulses. Figure 2.11 shows that a uniform distribution could improve the transverse emittance by 40% compared to that formed from a Gaussian shaped pulse at the sample position.

There are multiple methods available to create flat-top UV pulses such as a 4f-setup [58–61], Dazzler [62] and Pulses stacks [57]. A 4f-line with different masks is one of the most well known schemes. Figure 2.12 shows the basic configuration of a 4f setup. Each spectral component is angularly dispersed by the first grating. In the Fourier plane (FP) all spectral components are spatially separated and focused. By putting a specific mask in the Fourier plane, one can modify the phase and amplitude of each spectral component and thus shape the output pulse. Dazzler uses an acoustic wave to diffract light. By tuning the timing, frequency, and amplitude of the acoustic wave, it is possible to introduce arbitrary dispersion functions and pulse shape.

In our practical implementation, as the 4f-setup and Dazzler are not cheap and the efficiency is quite low especially for UV pulses, we decide to use the pulse stack solution with UV birefringent crystals [57]. Figure 2.13 shows the simple configuration for generating a flat-top pulse with birefringent crystals.

The first birefringent crystal splits the initial linearly polarized laser pulse into two replicas with the phase velocity of ordinary and extraordinary beams. The amplitude ratio is given by: $\frac{E_e}{E_o} = cos(\theta_{in})$, with E_o and E_e the amplitude of the two replicas. θ_{in} is the angle between the optical axis of the birefringent crystal and the input laser polarization. In order to get flat-top beam, both replicas should have equal amplitude. Therefore, θ_{in} should be around 45 degree. The pulses corresponding to the ordinary and extraordinary beams travel through the crystal with a time difference Δt_2 ($\Delta t_2 = \Delta v * d$, here Δv is the velocity difference between the ordinary and the extraordinary beams, and d is the crystal thickness).

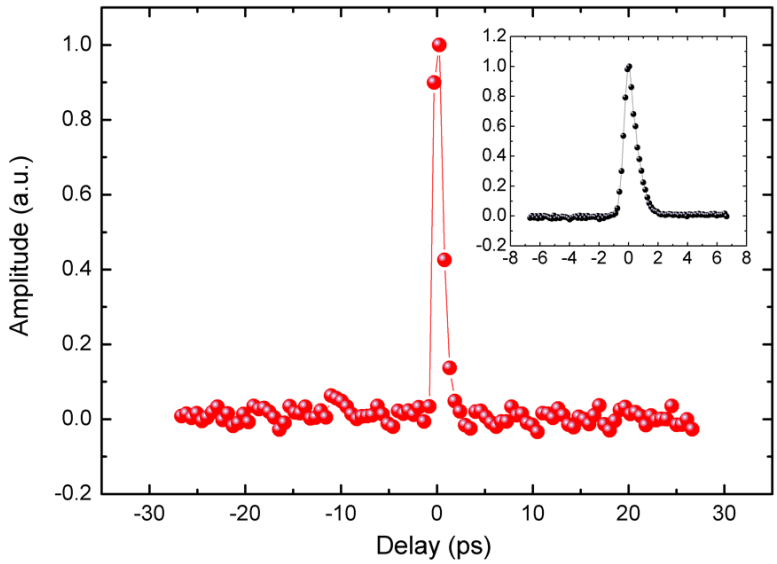

Figure 2.10: UV pulse duration 1 ps (FWHM) measured by cross-correlation. Laser pulse with 100 fs and 800 nm is used as the probe which cross-correlates with the unknown 266 nm UV laser.

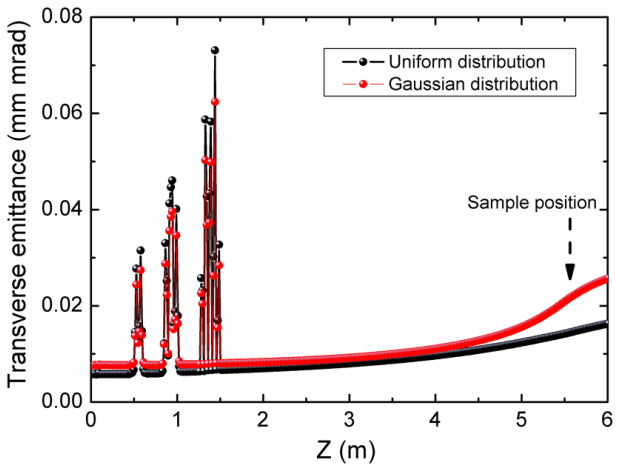

Figure 2.11: Simulated transverse emittance along the REGAE beam line with a uniform (black) and gaussian (red) longitudinal laser beam distribution. ASTRA simulation based on REGAE, see Appendix A.

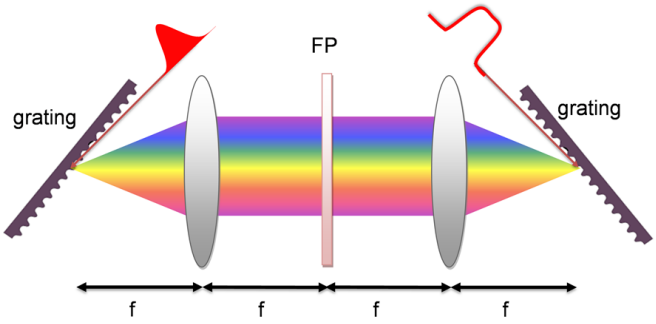

Figure 2.12: Basic configuration of a 4f setup. In the Fourier plane (FP), all the spectral components are spatially separated.

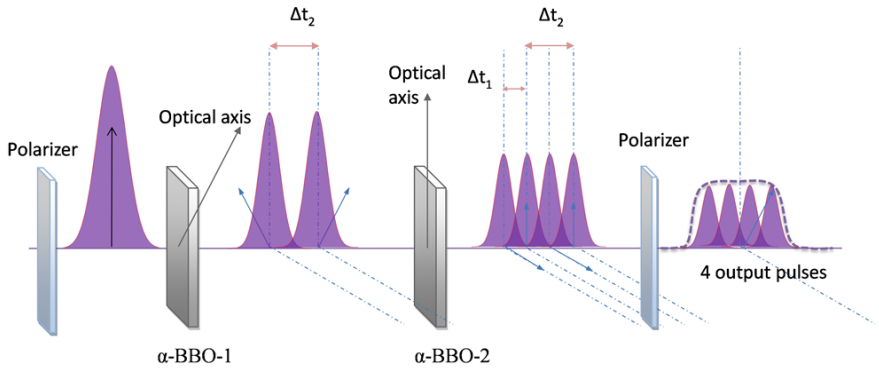

Figure 2.13: Schematic diagram by using 2 birefringent crystals to produce 4 stacked pulses.

The next crystal has its optical axis oriented in the same direction as the input pulse. When the two replicas pass through, each of them is divided into 2 more replicas with time difference Δt_1. After passing through another polarizer, four generated pulses form a flat-top beam.

By adjusting the prism stretcher we can fine tune the input pulse duration to optimize the beam profile. The generated beam can be further improved by more replicas and more careful design of the birefringent crystals.

Spatial profile of UV laser on RF photocathode Besides the temporal shape, the spatial laser profile also plays an important role in the electron gun. The electron beam emittance is dominated by the thermal emittance on the photocathode [63]:

$$\varepsilon_{ther,rms} \cong \sigma_r \sqrt{\frac{E_{kin}}{m_0 c^2}} \tag{2.3}$$

where E_{kin} is the excess kinetic energy arising from the difference between the energy of the driver laser photon energy and cathode work function, σ_r is the rms laser spot size. By controlling the beam diameter on the photocathode the beam emittance can be greatly improved. ASTRA simulation in Fig. 2.14 shows better transverse emittance with a smaller beam diameter.

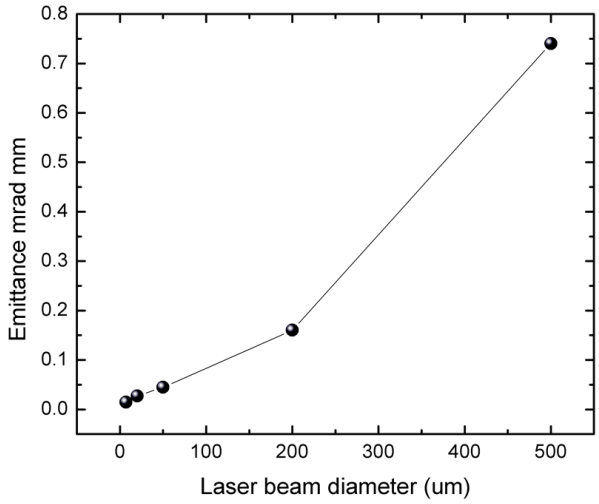

Figure 2.14: Simulated transverse emittance as a function of UV beam diameter. ASTRA simulation based on REGAE, see Appendix A.

To obtain a more uniform photoemission from the photocathode, a spatially flat-top beam (laser beam with uniform intensity distribution over the cross section of working plane) is also required. The beam shaper in this system is based on diffractive optics (New Span Opto-Technology Inc.). It transforms a near Gaussian incident laser beam into a uniform intensity spot. In order to get a better Gaussian beam and tight focus,

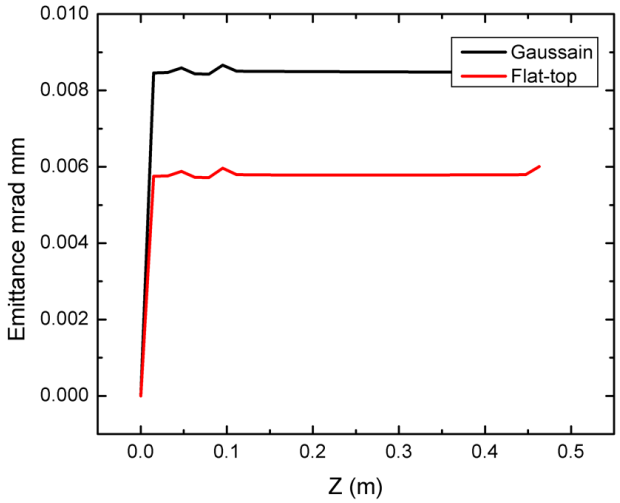

Figure 2.15: Simulated transverse emittance of a flat-top and Gaussian beam. ASTRA simulation based on REGAE, see Appendix A.

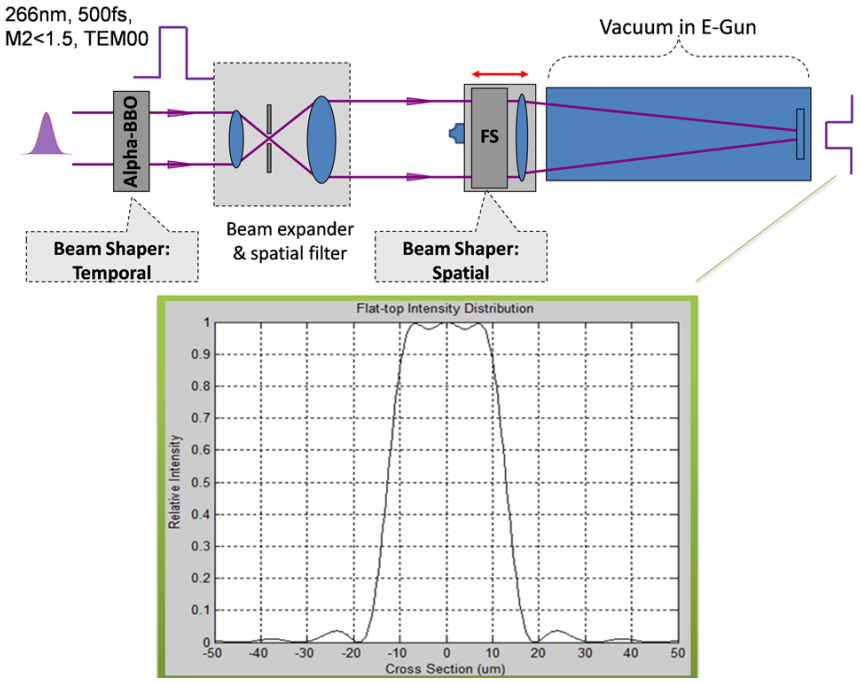

Figure 2.16: Layout of the transverse beam profile control setup. The input UV laser beam is first cleaned up by an alpha-BBO polarizer and spatial filter. A spatially flat-top beam can be generated at the photocathode position by diffractive filter and focusing lens.

a beam expander with a spatial filter has been used (Fig. 2.16). The simulated result (Fig. 2.16 insert, calculation from New Span Opto-Technology Inc.) shows that we could get RMS = 20 μm flat-top beam.

2.2.2. Laser pump arm for sample excitation

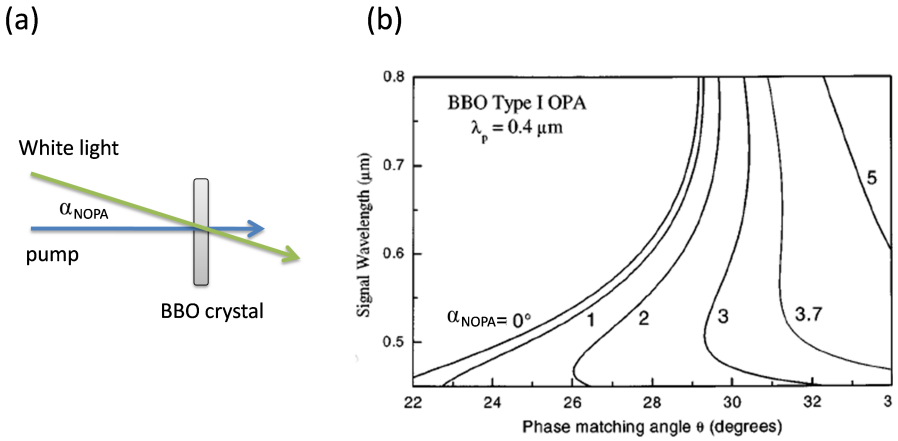

Figure 2.17: Schematic of a noncollinear interaction geometry (a) and phase matching angle (b). Adapted from [64].

Part of the laser beam is used as a pump laser to photoexcite the sample to trigger the structural change of interest. Based on the electronic properties of the sample, different pump laser wavelengths can be generated through nonlinear optical process. FH, SHG, and THG are the most commonly used beams as they are easy to be generated and can reach high fluence. In addition, a non-collinear optical parametric amplifier (NOPA) [64–67] has been built up to generate a continuously tunable wavelength from 450 nm to 700 nm. NOPA uses a white light continuum as the seed laser and SHG generated blue light as the pump (Fig. 2.17(a)). By properly adjusting the pump-signal angle (α_{NOPA}), we can achieve broadband phase matching over an ultrabroad bandwidth. Figure 2.17(b) shows that with an angle of α_{NOPA} = 3.7° the phase matching angle can extend from 0.5 to 0.75 μm. After proper dispersion compensation, it can produce up to 10 μJ of energy per pulse with sub-30 fs pulse width. A mid-infrared (mid-IR) OPA that can provide 3–7 μm is also under development.

Considering the long beam line for REGAE, many laser parameters need to be remotely controlled via instrument control systems. For example, the beam pointing on the sample should be controlled by a motorized mirror mount. The polarization state at the sample is controlled by a half-wave plate mounted on a motorized rotation

stage. Neutral density filters on a motorized rotation stage are used to control the pulse energy. The arrival time with respect to the electron pulse can be adjusted by a retro-reflector mounted on top of an optical delay-line with a 10 fs precision. The laser repetition rate is controlled by a pulse picker (Pockels cell plus polarizer).

2.2.3. Synchronization of the laser system with RF

An important parameter for the time-resolved experiments is the pulse-to-pulse variation of the arrival time of the bunches at a specific point in the system. Especially in a pump-probe experiment, where the laser pulses are used as a pump and the electrons are used as a probe, this variation directly limits the achievable time resolution. For a compact FED system, electrons are accelerated by constant electric field. There is no timing jitter between the electron bunch and pump laser. But for a relativistic electron gun, which uses RF field, it is very important to control the timing between the laser and RF. This is because a different phase of injection results in different electron energy, hence, a different arrival time at the sample position. The better the synchronization, the lower the energy jitter and arrival time-jitter of the accelerated electron bunches. REGAE has pulses with duration in the order of tens of fs. To fully exploit the opportunities provided by these short light sources, a system to synchronize the external lasers with the RF and to stabilize the electron bunch arrival time has been constructed. Here in REGAE we utilize a DESY phase lock solution that provides as little as 20 fs timing jitter.

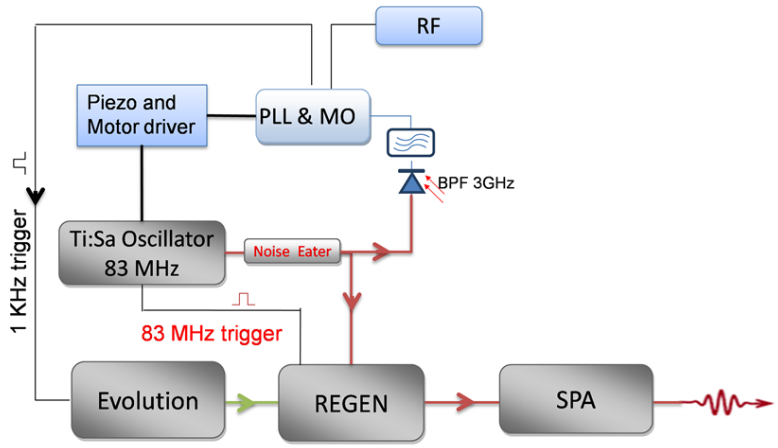

Figure 2.18: Diagram of synchronization setup for REGAE.

The synchronization system makes use of the fact that both the RF system (see

Chap. 3) and the laser system consist of an oscillator and an amplifier. The RF system includes an electronic oscillator and electronic klystron amplifier, while for the laser system both of them are optical. The precise synchronization is based on locking both the electron beam and the laser to the same reference, hence avoiding additional jitter by any intermediate system. Figure 2.18 shows a simplified diagram of the closed-loop synchronization. A 125 MHz crystal oscillator, which provides a more stable frequency, is chosen to be the master oscillator (MO). The Phase locked loop (PLL) technique is used to synchronize the laser oscillator to the MO. The closed-loop control checks the phase difference between laser oscillator and MO, and tunes the laser cavity to match the MO frequency.

The timing jitter of the overall setup is limited by the temperature, humidity, electronic jitter, and the stability of Micra-5 laser. The temperature and humidity for electronics are controlled by a cabinet with an AC system and the laser system is stabilized by a water cooling optical table. Meanwhile amplitude-to-phase conversion of the laser also limits the long-term phase stability of the microwave signals [68]. To improve this we implement a noise eater (Conoptics). This is an electro-optic feedback loop capable of reducing the amplitude variation commonly associated with lasers. Figure 2.19 shows measurement over 10 hours with and without the Noise Eater. It can be seen clearly that the long term amplitude stability is highly improved by using this noise eater.

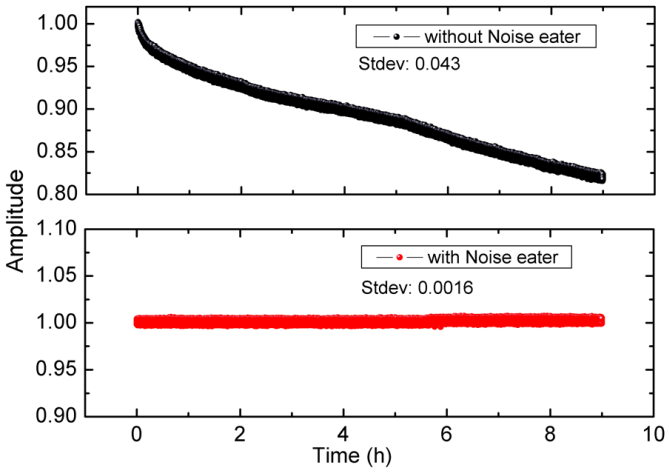

Figure 2.19: Stability of laser with and without the noise eater for over 10 hours.

Although the contribution of the laser amplifier to the total jitter is negligible, the jitter induced by a change of the klystron phase and amplitude is relatively high. A phase and amplitude change of the RF will induce a change of the arrival time of the electron beam on the sample. The influence of RF field change can be seen in Fig. 2.20. For simplicity, the simulation only takes into account the RF cavity. A change in phase of only 0.5 degree phase could induce more than 200 fs timing difference, which is crucial in a system with a bunch length of less than 100 fs. In order to correct

this, an electronic feedback system is used to compensate the long term drift of the RF field. The phase and amplitude jitter of the RF field was measured to be around 0.02 degree and 0.01% per hour, which enable good stability of less than 20 fs. Besides the RF system, REGAE includes many other electronics and optics that can induce electrical or optical noise. In order to get the best performance we have to investigate and improve the system further for problems.

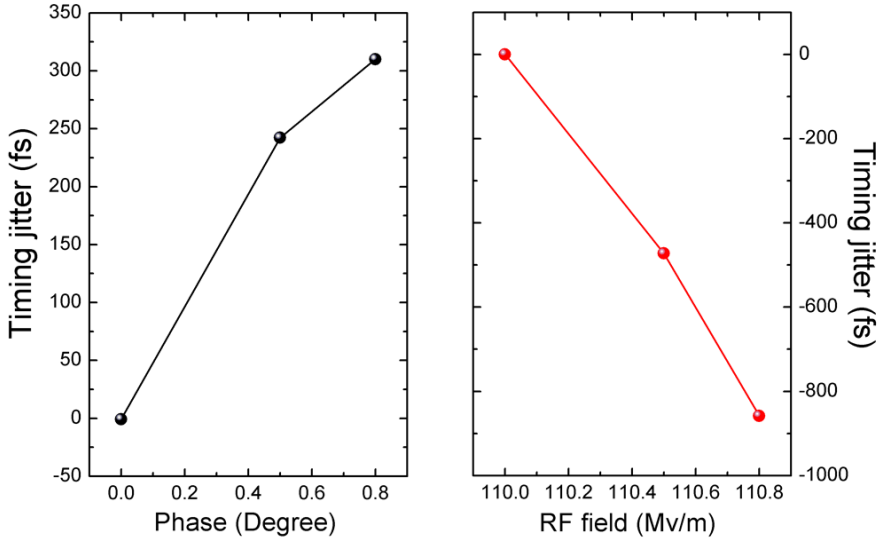

Figure 2.20: Timing jitter at the sample position introduced by phase and amplitude change from the Buncher cavity. ASTRA simulation based on REGAE, see Appendix A.

2.3. Femtosecond optical pump-probe spectroscopy system

The femtosecond laser system allows the exciting field of time-resolved spectroscopy to be developed. Pump-probe experiments with fs lasers have been widely used for studying ultrafast carrier dynamics in various materials in order to understand many fundamental properties of the materials. Femtochemistry was first founded upon the study of gas-phase molecular dynamics by Zeweil and co-workers, as recognized in 1999 by the Nobel Prize in Chemistry [69]. The technique was further applied to study fundamental chemical and physical processes. Femtosecond optical pump-probe spectroscopy [70] enables us to observe fast chemical reactions, phase transitions and surface processes on a fs time scale. In this technique, a material is excited with a pulsed laser that populates quantum states above the ground state, thereafter, creates nonequilibium density of quasiparticles that subsequently cause a change in the index of refraction. One then measures the transmission or reflection of the probe pulse with a variable delay. The change of the transmission or reflection curve provides relaxation time of the photogenerated excitations.

In order to obtain some preliminary knowledge of the sample properties, a femtosecond optical pump-probe spectroscopy system has been built in our FED lab. Compared

with the FED experiments, it has a much simpler configuration, but it is capable of providing us with a lot of information about the sample such as damage threshold, and optical and electrical properties that are complementary to the information obtained by the FED experiments. This section will mainly focus on building up a pump-probe setup. It includes the configuration, automation and characterization of the system.

2.3.1. Layout of optical pump-probe setup

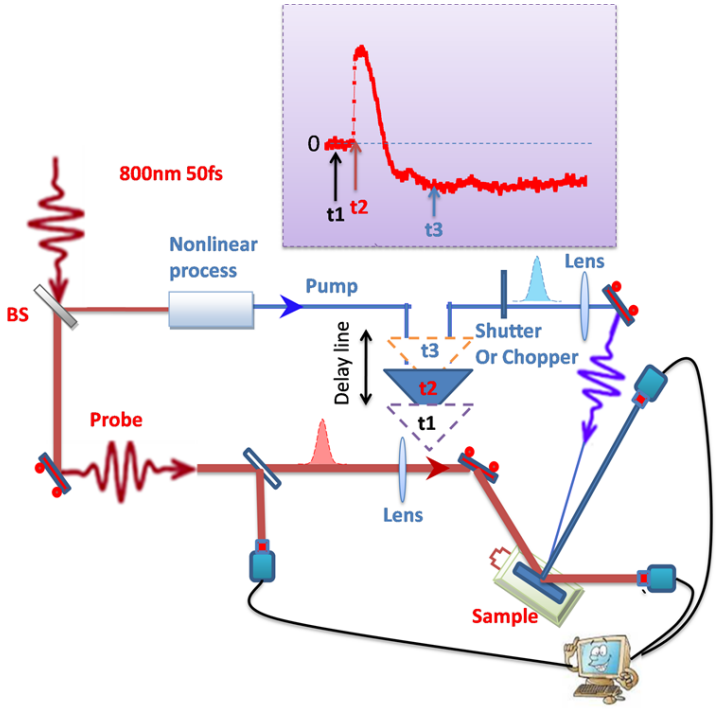

Figure 2.21: Layout of an optical pump-probe setup. The laser beam is split into two arms (a relatively strong pump beam on a motorized delay line, a small fraction for probe beam). Pump, probe and reference signals are collected by the computer through the data acquisition card. Insert: a simple pump-probe trace that shows different reaction of probe at different points in time (t1, t2, t3).

Figure 2.21 shows the basic layout of optical pump-probe setup. It is similar to the auttocorrelation setup described before (Fig. 2.2). A laser beam is split into two arms (one for pump with motorized delay line, and one for probe). Based on the electronic properties of the sample under study, the pump and probe beams can be varied in wavelengths via the generation of different nonlinear processes, e.g. white light generation, SHG, THG, OPA etc. The pump beam carries most of the energy to trigger dynamic changes of interest, e.g. a chemical reaction. The probe beam is kept much weaker than the pump beam in order to avoid probe-induced dynamics. Meanwhile to correct the shot to shot jitter of the laser a small portion of the probe beam is taken as reference. Pump, probe and reference signals are detected and saved simultaneously by the computer. Femtosecond time resolution is obtained by changing the relative

time delay between the pump and probe pulses. When the delay line is at position t1, as described in Fig. 2.21, the probe beam experiences a shorter optical path and arrives earlier than the pump beam on the sample. Therefore, the probe does not see any change of the sample and its reflectivity or transmittance does not change, which can also be seen in the differential transmission (reflection) plot in Fig. 2.21(insert). When the delay line is moved to t2, the pump and probe beams experience an equal optical path. The probe beam begins to experience the pump induced change. Afterwards, when the delay line is moved to t3, the probe has a longer optical path and arrives on the sample some time later than the pump. Now the probe sees the pump induced transient state. We can map out the time-resolved pump induced change of the sample by repeating the processes and plotting the reflectivity or transmissivity change of the probe beam as a function of the time delay, as shown in the insert in Fig. 2.21.

To suppress background light and low frequency noise of the probe beam, a chopper with a lock-in amplifier can be used. It uses phase-sensitive detection (PSD) to improve the signal-to-noise ratio. The analytical signal can be modulated at some reference frequency by the chopper. Typical mechanical choppers run up to 20 kHz. With acousto-optical modulators it can run up to one hundred MHz. The lock-in-amplifier amplifies only the component of the input signal at the reference signal, and filters out all other frequencies, i.e., noise. A gated Integrator can further improve the signal to noise ratio by integrating an analytical signal over a fixed time window when the signal is present, which is particularly helpful for pulsed laser measurement.

For irreversible samples, it is required to use a fresh sample for each shot. A fast shutter (mechanical shutter, normally more than ms, or optical shutter with less than ns opening time) is used to isolate each laser pulse. A motorized XYZ stage is used to move the sample. To improve the sensitivity we use a home-made photodiode with peak-hold feature ($\sim$100 μs) and low noise level. We can also replace the photodiode to a spectrometer for single-shot time-resolved spectroscopic measurement.

Many other pump-probe variants have been developed based on these methods like: Electro-optic sampling [71], THz spectroscopy [72] and Four-wave mixing [73].

2.3.2. Automation and characterization of the system

Automation and computing are of crucial importance to the experiment. A Labview based user interface has been developed for data acquisition. In this section, the two core software components of the experimental setup are described: beam diameter measurements, and pump-probe measurements, which include general data acquisition with a lock-in amplifier, single-shot measurements, and spectroscopic measurements. The experimental setup contains several hardware devices that need to be remotely controlled via software. These devices include XYZ translation stages to move the sample, an optical delay stage to vary the path length between the pump and probe laser arms, a spectrometer to record the spectrum, a photodiode with National instrument digital acquisition card to record the laser pulse trace, mechanical shutters to block or unblock the pump and probe laser arms, a CCD camera with microscope objective lens for checking the beam overlap, and a powermeter to measure the pump and probe power. The control program needs to talk separately to each of these devices, as well as synchronize various devices to allow data acquisition in a single-shot mode.

These aspects, which are often unnoticed in the scientific literature, involve careful design of the blueprint of the system, writing hundreds of pages of code, and finally creating a robust software for the experiments. In Chapter 3, similar software has been developed. However, they are more sophisticated in the case of FED system.

Beam diameter measurement

One of the important parameters in performing optical pump-probe studies is the pump fluence. It is especially important for irreversible experiments whose dynamic change of the sample highly depends on the pump laser fluence. For example, silicon can experience thermal melting, non-thermal melting and ablation when changing the fluence from a few mJ/cm^2 to tens of mJ/cm^2 and hundreds of mJ/cm^2. The beam diameter measurement is based on the Knife-edge method. The intensity distribution of the laser beam can be given by a Gaussian function $I(r,z) = A(z)e^{\frac{-2r^2}{w(z)^2}}$, in which r is the distance from the center of the beam, $A(z)$ and $w(z)$ describe the peak intensity and width of the beam, respectively. By moving in the knife edge, as illustrated in Fig. 2.22, the intensity change of the beam can be calculated by an integral: $\int_x^\infty Ae^{\frac{-2(x-x_0)^2}{w^2}}dx$, where x is the position of the knife edge.

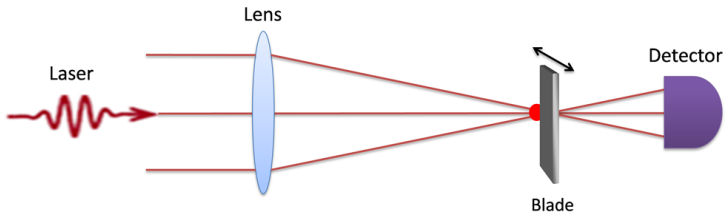

Figure 2.22: Knife-edge method for beam diameter measurement.

By moving the knife edge with a motorized stage and recording the unblocked part of laser power with a detector, we can plot the relative knife edge position versus laser power. The beam diameter and relative spatial beam profile can be retrieved from the curve with the integral. Figure 2.23 shows the basic Graphical User Interface (GUI) of the programmed software, which includes setting of the stage, alignment of the knife edge with motorized stage, and measured beam diameter.

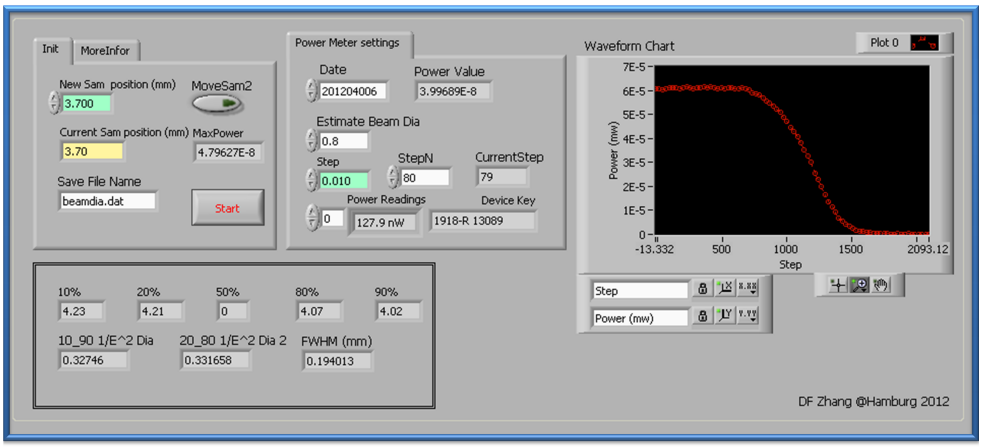

Figure 2.23: Labview user interface for beam diameter measurement. It includes controls to chang the knife edge position, set the scanning parameters, save and retrieve the data.

Data acquisition for optical pump-probe measurement

The data acquisition process is controlled by automation software based on Labview, which normally takes tens of minutes to hours. Depending on the specific experiment, single-shot, lock-in and spectroscopic techniques can be chosen for the signal detection.

The control and automation program include the basic alignment of the sample, setting of time zero position, step number and travel range in the experiment. The data collection with a lock-in amplifier is the simplest example, which just collects signals from the lock-in amplifier after each time step and plots it directly. The method relies on repeated measurement, where the sample returns to its initial state after each laser shot.

Single-shot measurements are required for any structural and chemical dynamics that occur irreversibly. Therefore, each portion of the sample is only excited once to avoid the accumulation of damage from the laser. In this case, we have to use a fast shutter to isolate single pulses. The software will collect all pump, probe, and reference signals and then plot online the $\delta T/T$ or $\delta R/R$ changes. After each laser shot, the sample should be moved to a fresh position with an XYZ motorized stage. The delay line should also be moved based on the average time of each time point.

Spectroscopic measurements use a spectrometer as the detector. In this case, a broadband probe (for example white light) can be used. The software can provide the $\delta T/T$ or $\delta R/R$ change for the overall spectrum, which gives us quick information about the dynamic change. Post data analysis can reveal more information as much more data are collected. But this spectroscopic method requires a longer data acquisition time and has a poor signal-to-noise ratio due to lack of integration in comparison with photodiodes.

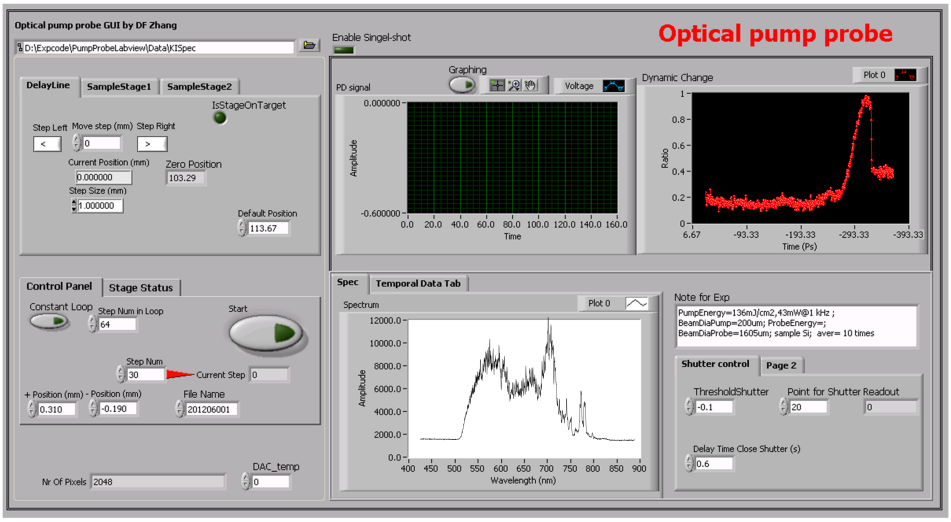

Figure 2.24: Labview based user interface for the optical pump-probe data acquisition.

2.4. Summary

This chapter presented the laser and related optical systems for the FED lab. An autocorrelator and a FROG have been built up for characterizing the commercial Ti:sapphire laser and related sub-systems. The autocorrelator measures the laser pulse duration on-the-fly, while the FROG can give more detailed phase and amplitude information for further optimization.

THG and related pulse shaping are important for pulsed electron generation. Other systems like SHG, and NOPA are also developed for generation of different wavelengths to meet with specific sample requirement. An overall control of the laser energy, pulse duration, polarization, spatial and temporal shape, and beam pointing is highly desirable in REGAE, and has been described in this Chapter.

A synchronization system that is based on DESY LLRF phase lock solution was also described. It is one of the key parts to achieve femtosecond time resolution for REGAE FED experiments.

Furthermore, an optical pump-probe spectroscopic system, which is important to study many fundamental properties of materials, was discussed in detail. Prior to FED experiments, this system helps us get the basic knowledge of the sample that is required to perform the experiments on FED setup.

Our FED systems have just started commissioning. Further improvement of the laser system will help to optimize the overall system.

3. Development of Femtosecond Electron Diffraction system

Femtosecond electron diffraction has been stimulated by its potential to provide a complete, global picture of structural dynamics on the femtosecond time scale with atomic level detail. The development of FED sources has attracted increasing interest over the past years [74, 75]. In this chapter the development of two femtosecond electron sources, a compact electron gun and a relativistic electron gun (REGAE), will be discussed. The first section will discuss the compact system, which is also known as table-top FED (Egun300). The system we built up in Hamburg is based on a scaled up version of the 60 keV machine [29] at the University of Toronto. The new machine can provide femtosecond electron bunches with an energy of up to 150 keV. The second part of this chapter describes our recently commissioned setup – REGAE. This accelerator based electron diffraction system has been built within a collaboration with DESY and Miller group. REGAE can provide 2–5 MeV electron bunches with sub-100 fs time resolution. This thesis was contributed to the development from the beginning of the collaboration.

3.1. Compact Femtosecond Electron diffraction system

This section will give a practical introduction to the development of a compact femtosecond electron diffraction system that relies on direct current (DC) i.e., where electrons are accelerated by a static electric field. Pulsed electron generation by compact electron gun design, present vacuum chamber configuration, and FED experiments will be discussed in detail.

3.1.1. Compact electron gun configuration

Electron generation for compact gun

Figure 3.1 shows the basic principle of a compact electron gun setup. After UV laser excitation the generated electrons will migrate to the solid surface and escape across the surface potential barrier into the vacuum [76–78]. Those electrons are further accelerated by the static electric field between the oppositely aligned capacitor plates and propagate to the sample chamber.

Egun300 uses carefully prepared photocathodes with backside illumination for electron generation (Fig. 3.1). A 16 mm diameter sapphire disk, which is transparent for the UV laser light, is used as the substrate of the photocathode. A layer of 3 nm chromium is deposited over the front side and the edge. In the second coating

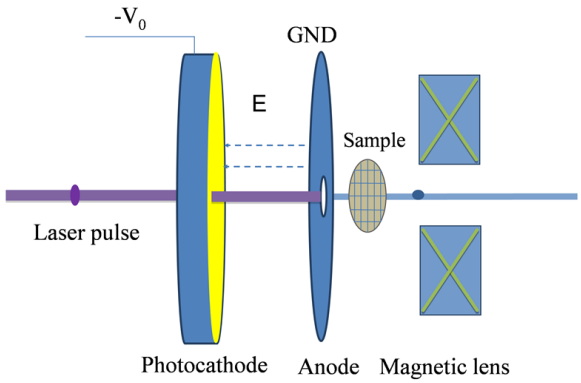

Figure 3.1: Principle of the pulsed electron generation in compact FED system. Electrons are generated from backside illumination of the gold photocathode and accelerated by the electric field between the photocathode and the anode.

procedure a 20 nm gold layer is deposited in the same way to provide the electrical contact with the power supply.

The photocathode is mounted to a macor holder that supports the cathode potential. Macor is a vacuum compatible and machinable ceramic, which has high dielectric strength. The surface of the macor should be smooth and curved to ensure a uniform field between the photocathode and the anode. The anode plate is made of a commercial silicon wafer, which is boron-doped for high electrical conductivity to avoid charge accumulation, and polished to optical flatness to avoid high-voltage discharges. A 500 μm hole is drilled in the center by mechanically drilling. To further collimate the electron beam a platinum pinhole (50–400 μm) is placed after the anode, which is normally required for a small sample size. The DC electric gradient between the photocathode and the anode is in the order of 10 MV/m with the cathode biased at -150 kV.

Pulsed electron bunches generated in a compact electron gun are normally highly influenced by the space charge broadening effect. The pulse duration increases with the number of electrons and the time of flight between the source and the target. Figure 3.2 gives the correlation of the electron density with the pulse duration at the sample position. It shows that the current 150 keV setup could provide a bunch length of around 200 fs for 10^5 electrons, which has a brightness of around 10 e/μm^2. There are two ways to achieve femtosecond time-resolved data, first by minimizing the distance between the electron source and target, and second, by maximizing the acceleration voltage [21–23]. The two competing requirements of structural and temporal resolution should be balanced: the electron density must be minimized while still maintaining sufficient signal to noise ratio. In this compact gun setup we reduced the electron propagation distance from the photocathode to the sample (the shortest:

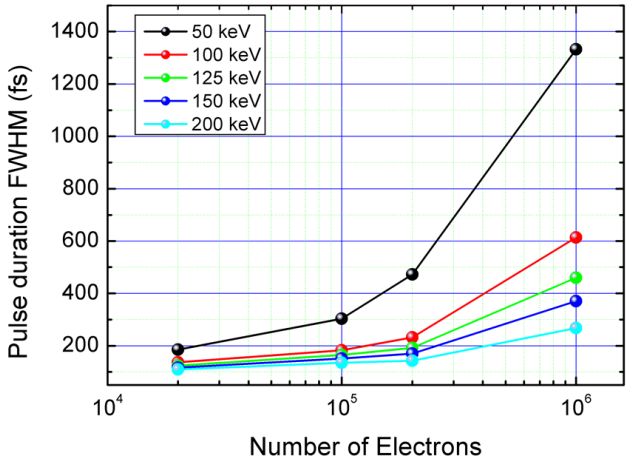

Figure 3.2: The correlation between the electron density and the electron pulse duration. ASTRA simulation based on compact FED system, see Appendix A.

1.5 cm) and increased the acceleration voltage (Power supply provides up to 300 kV. Currently the gun is running at ∼150 keV with stable operation) to get the optimal operation.

The high voltage acceleration potential defines the kinetic energy of the electrons and hence their velocity. At V_0 = 100 kV, the time that the electron pulse takes to propagate from the photocathode to the sample is 304 ps and changes by 2 fs per 1 V potential change in the high voltage. Therefore, the stability of the high voltage power supply must be better than 0.1% in order to keep the timing error below 100 fs. The Heinzinger PNC – 300000-1 power supply employed in our setup provides a stability of less than 0.01% rms over 8 hours, which enables a timing error of less than 10 fs.

Vacuum chambers in the compact FED setup

The vacuum chamber consists of two sections: electron gun and sample chamber. They are pumped by separated turbo and scroll pumps. Figure 3.3 shows the basic assembly of Egun300 chamber.

The photogun is equipped with a commercial ceramic HV feedthrough with its length made as long as possible to maximize the strike and creep distance. Ceramics are also ribbed in order to achieve maximum surface distances with minimal impact on an insulator's overall length. Electrons are generated through the photoemission as described above in the electron gun chamber and propagate into the sample chamber through the pinhole in the anode plate.

The sample chamber houses the sample, sample manipulation, pump beam optics, the magnetic lens and the detector. We use a commercial manipulator (Vab: PM12-150 with the travel range X = ±10 mm, Y = ±10 mm and Z = 0–150 mm), which incorporates a cold finger to provide the cooling and heating capabilities for certain experiments. It is important to be able to move the sample accurately and quickly,

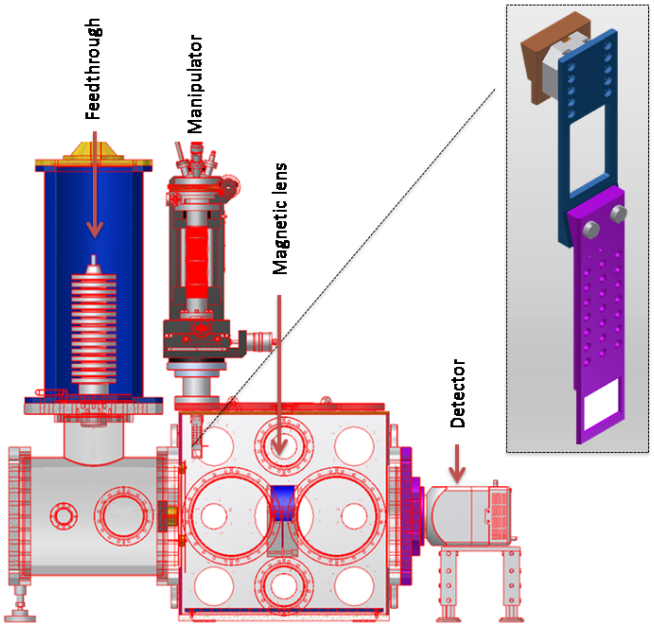

Figure 3.3: Assembly of Egun300 vacuum chamber (Insert: sample holder).

especially for single-shot experiments that require a fresh sample for each individual shot. If the sample is not parallel to the motion of the manipulator, a change in the pump-probe delay will be introduced:

$$\Delta\tau = \Delta z(\frac{1}{v_z} + \frac{1}{c}) \tag{3.1}$$

where v_z and c correspond to the electron velocity and the speed of light in vacuum respectively. Δz is the offset distance of the sample holder if moved from one position to another. This is particularly important for experiments using irreversible samples, which require a large amount of samples for many shots. To keep the deviation below 100 fs for samples arranged over a 2 cm long holder, the tilting relative to the motion of the manipulator should be less than 0.03 °. The insert in Fig. 3.3 shows the assembly of the sample holder on a goniometer. By using the needle or laser topography methods we can correct the parallelism to be better than 0.01 °, in which the relative position of the sample holder can be retrieved by monitoring the contact between the needle and the sample holder or by the reflective laser pointing while moving the manipulator.

The magnetic lens is placed downstream of the sample. The focal length (f) of a magnetic solenoid lens [79, 80] can be given by:

$$f = \frac{4m^2v_z^2}{e^2\int B_z^2 dz} \tag{3.2}$$

where v_z is the velocity of the electrons propagating in the z direction, m is the electron's rest mass, e is the electron's charge, and B_z is the magnetic field in z

direction. The integration is performed over the entire length of the field. The focus position for this compact FED setup is chosen to be 0.5 meters after the magnetic lens. The magnetic lens operating current is set by optimizing the sharpness of the diffraction rings observed on the detector. For a 150 keV electron beam a current of 0.5 A is necessary. As the current in the solenoid wire will heat up the system, cooling is provided by the contact with the holder. With the solenoid set at 0.5 A, the voltage change is less than 1% for over an hour's test, which corresponds to a temperature change of less than one degree. The whole magnetic lens is mounted on top of two motorized stages that can move the lens horizontally and vertically. They help center the electron beam with respect to the optical axis in order to minimize the divergence, which is very important for high quality data.

Electron diffraction detection is usually achieved by means of a phosphor or a scintillator where the energy of the electrons is converted into optical light subsequently detected by a CCD camera. The coupling between the phosphor and the CCD camera can be achieved either by a free-space optical system, in which a lens images the phosphor onto the CCD chip or by a fiber-optic plate, which is placed directly between the phosphor and the CCD chip. In our setup we have a 2084 x 2084 pixel imaging array with 1:1 fiber-coupled CCD camera (Princeton Instruments: 4320). A replaceable fiber optic plate coated with phosphor (P20 or P43) is used in front of the CCD chip to convert electrons to photons. This furthermore gives us flexibility to test different phosphors for best performance. In order to remove background from the pump laser a layer of aluminum (around 100 nm) is coated on top of the phosphor. Since the camera does not have a shutter and the read out time is much slower compared to the laser frequency, a mechanical shutter is used to stop injection of electrons during read out.

In order to measure the electron beam current, the vacuum chamber houses a Faraday cup, which can be moved in front of the detector by a motorized linear feedthrough. A typical configuration of 5000 electrons/pulse at a laser repetition rate of 1000 Hz corresponds to an average current of 0.8 pA. To measure these beam currents reliably, the Faraday cup is connected to a sensitive electrometer (Keithley 6514).

It is necessary to condition the photogun for withstanding high voltage. The voltage should be turned up slowly until breakdown is detected. The breakdown will smoothen the surface. The breakdown signal then restarts the power supply at a lower voltage and resumes the training until it is stable at the setting voltage. This normally takes a few to tens of hours depending on the gun condition.

3.1.2. Time-resolved electron diffraction measurement

Automation

For safety reasons the FED machine is enclosed in a radiation protection hutch, which is not accessible during experiments. This means most of the devices need to be automated. Motorized mirrors are used to control the position of the laser beam on the photocathode as well as the pump laser beam on the sample. Figure 3.4(left) shows the control panel for steering the mirrors. The pump beam diameter can be

adjusted by moving the focusing lens and is measured by the knife edge method (see Chapter 2). The electron beam diameter can be changed with the collimating pinhole. It is normally such that the pump beam is 2–3 times larger than the probe beam size to ensure a uniform pump illumination of the probe region. To overlap the pump and probe beams, a small aperture (500 μm) is inserted into the beam line by the manipulator. By measuring the reflected laser beam with a Firefly CCD camera and the transmitted electron beam with PI detector (as can be seen in Fig. 3.5) and comparing the measured intensity with the relative position of the small pin hole, we can optimize the spatial overlap of laser and electrons. As the pump laser detection is in reflection mode when it is centered in the pin hole, the CCD camera receives the lowest signal from the reflected laser, while the PI detector has the highest signal from transmitted electrons when it is well aligned with the electrons. Figure 3.4 depicts a screen shot of the user interface of the control panel showing the pump-probe overlap at 0.5 mm in the horizontal position. By steering the pump beam (Fig. 3.4 (left panel)) and overlapping the trough of pump with the peak of probe in Fig. 3.4(right panel), the pump and probe can be precisely overlapped within a few micrometers in horizontal and vertical directions.

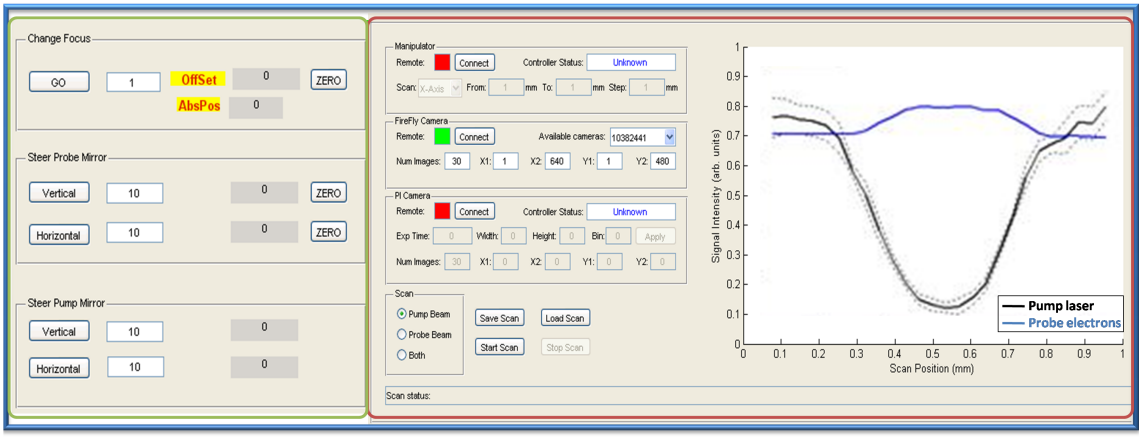

Figure 3.4: User interface for (left) laser pointing optimization and (right) electron-laser beam overlap.

FED configuration

Femtosecond electron diffraction has the potential to directly observe transition state processes. By changing the path difference between the pump laser and the probe electrons, the sample is imaged at different time points relative to the excitation; thereby capturing the photoinduced structural changes in real time. Figure 3.5 shows the basic layout of the time-resolved electron diffraction setup. It consists of a fs-laser

and a coupled photoemission electron gun arranged in a pump-probe geometry (see Chapter 2 optical pump-probe spectroscopy for detail).

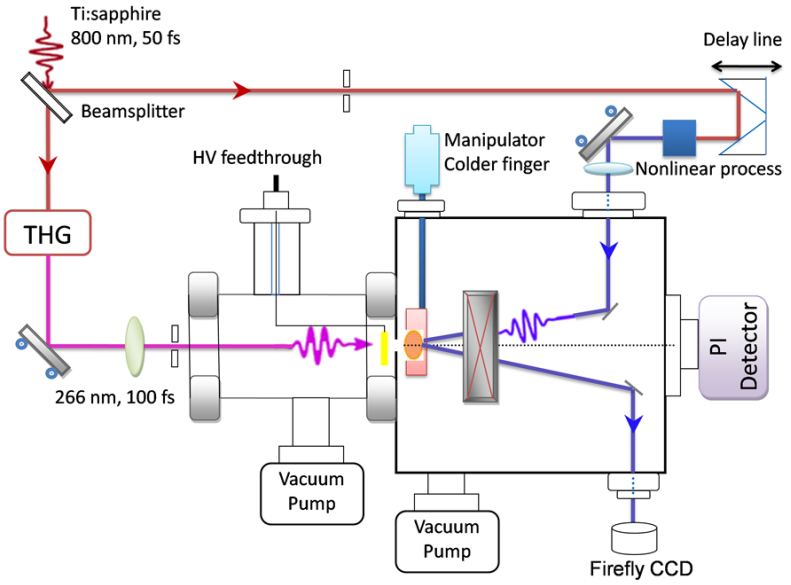

Figure 3.5: Layout of Femtosecond electron diffraction system.

To pursue a higher brightness and shorter pulse duration the new generation electron gun is powered with a 300 kV power supply, which can push the electron speed up to 77.6% of the speed of light. One laser beam is split into two for both the electron generation and the sample excitation. A 305 mm travel range delay line is used to adjust the relative delay between the probe electrons and the pump laser.

Data acquisition

Snapshots of diffraction images associated with transient structural changes induced by the laser excitation are obtained by the pump-probe program. The data acquisition for electron diffraction is quite different from the optical pump-probe as the probe and pump-probe data should be collected separately, and each shot is saved as one image with 2084*2084 pixels. A sequence of the probe delays is programmed to have electron pulses arrive either before (negative time) or after (positive time) the pump laser pulse. The time interval should be adjusted to match the rate of the relative structural changes. Figure 3.6 shows the control panel for the FED data acquisition. It includes the basic control and settings for manipulator, delay line, shutter and detector. During the experiment, we record 'before', 'during' and 'after' diffraction images, which are recorded before laser irradiation ($t = -\infty$), during laser irradiation (at a given time delay t), and afterward ($t = -\infty$).

Further data analysis is required to reveal the details of the dynamic processes. Figure 3.6 (insert) shows the time-resolved data from silicon before and after time

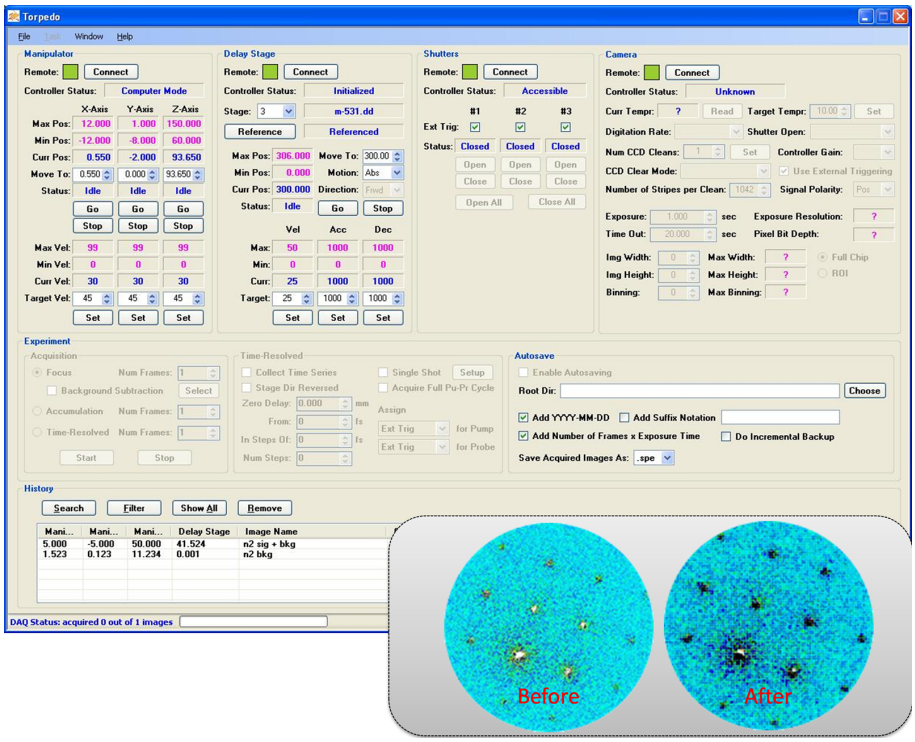

Figure 3.6: Data acquisition software for ultrafast electron diffraction and diffraction pattern from single crystalline silicon with and without pump laser.

zero with 400 nm pump laser (1 mJ/cm^2). The structure induced diffraction change is clearly visible. The loss of intensity in the diffracted orders is accounted for the Debye-Waller effect on a time scale indicative of a thermally driven process [81]. Exciting the material with even higher fluences, silicon will experience non-thermal melting or even Coulomb explosion, which will be discussed in Chapter 5.

3.2. Relativistic electron gun for atomic exploration – REGAE

The space-charge related time broadening effect is the most significant limitation for a DC accelerated electron gun setup, limiting the number of electrons to 10^5 per pulse for femtosecond bunches. Coulomb repulsion is suppressed in relativistic sources, which allows for more electrons per bunch. Several groups all over the world e.g. at SLAC [82], UCLA [9], Tsinghua University [83], Osaka University [10], BNL/Shanghai Jiaotong University [84] are developing RF guns for electron diffraction. Single-shot MeV electron diffraction and time-resolved measurements have been demonstrated successfully.

The RF gun uses the acceleration techniques developed for the linear accelerators (linac), which can bring electrons from a standing start to a relativistic velocity. It is based on alternating the current applied on the electrons from the klystron that creates

a time-varying electric field, typically in the range of 100 MV/m. They propagate down the cavity in the same direction as the electrons and impart a significant proportion of the RF power to the electrons. REGAE is based on an RF-accelerated electron source generating 2–5 MeV electron bunches with more than 10^6 electrons. It uses a rebunching cavity, which can compress the bunch length to as short as 20 fs (FWHM). In this section the main characteristics, basic beam line, and time-resolved FED configuration will be discussed in general.

3.2.1. REGAE beamline

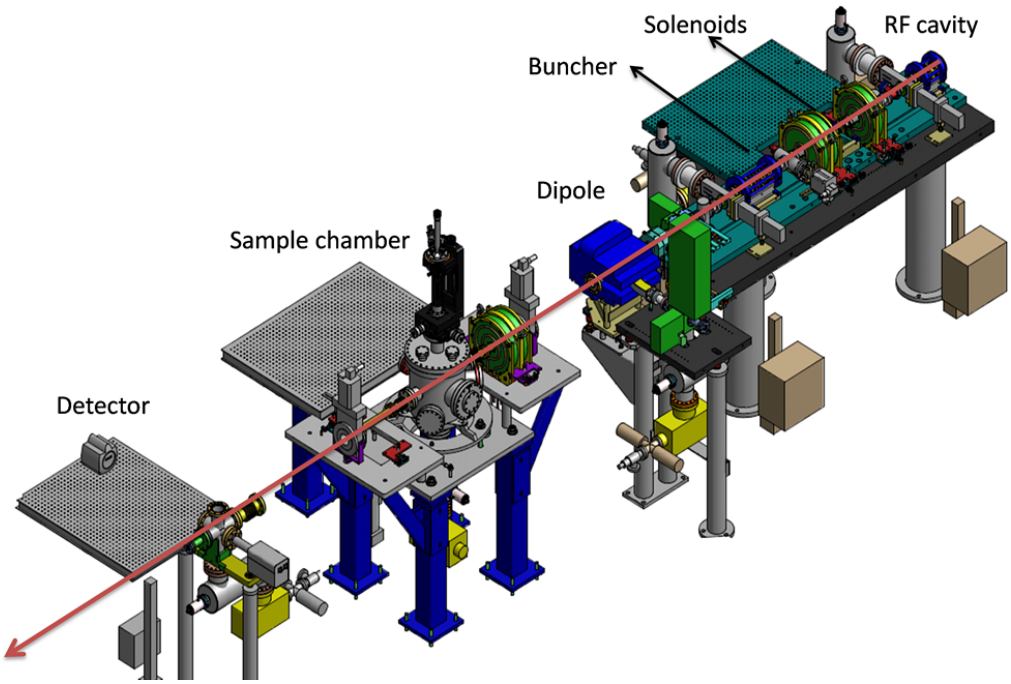

Figure 3.7: Layout of the REGAE beamline.

As shown in Fig. 3.7, the REGAE beam line consists of the RF gun, the rebunching cavity, the magnetic solenoids, a sample chamber and diagnostics.

The RF gun and its infrastructure include the photocathode system, klystron, waveguides and RF cavities. REGAE employs frontside illumination and cathode loadlock system, which is quite different from the compact electron gun. Connecting to the RF system it requires much better vacuum, which is normally around 10^{-10} mbar. The laser beam is coupled onto the photocathode with an in-vacuum aluminum mirror. To maintain good flatness and conductivity, the aluminum mirror consists of a doped silicon wafer coated with 100 nm aluminum by a thermal deposition machine. The cathode loadlock system enables us to transfer cathodes directly from ambient environment into the chamber. Inside the cathode box up to 5 cathodes can be pre-installed. There should be at least one scintillator cathode that is used for alignment of the UV excitation laser. By ensuring a collinear propagation of the UV laser with a Helium-

Neon (HeNe) laser we can get a rough alignment of the UV laser on the scintillator cathode. The HeNe laser helps to see the position of the laser beam on the cathode as the scattering is much higher than that from the UV laser. Precise alignment can be done by imaging the UV laser spot on the scintillator cathode with a CCD installed downstream. It can give us direct information of the laser beam profile and the alignment at the cathode position. Afterwards the $CsTe_2$ (gold, copper or other cathodes) cathode can be switched to replace the scintillator cathode by the loadlock system. A virtual cathode outside the vacuum is used to monitor the pointing of the UV beam during machine operation (Chapter 2: Fig. 2.7). The loadlock system also gives us flexibility to explore materials for better beam emittance, which is dominated by the thermal emittance of the photocathode (Chapter 2: Eq. 2.4). One can greatly increase the transverse coherence length by using cathodes with lower thermal emittance (Fig. 3.8). The influence of the laser spot size on the transverse coherence is discussed in Chapter 2 (Fig. 2.14).

Electric field generated in the RF cavity needs to be present only when electron bunches have to be accelerated. It is provided by a klystron, which is a high gain pulsed amplifier with excellent stability and efficiency. The klystron of REGAE can provide 24 MW maximum power with up to 6 μs long RF pulses and a repetition rate up to 50 Hz. Radio frequency cavities receive RF energy from the klystron and transfer it to electrons as they pass through the cavities. The microwaves in the cavity are synchronized to crest just as each bunch of electrons enters the cavity, so that the bunch is accelerated by a wave that is approaching the peak amplitude. It accelerates the electrons to around 99.5 percent of the speed of light.

The REGAE RF gun is a 1.5 cell S-band cavity with a coaxial on-axis RF coupler. The radio-frequency system provides the driving power for accelerating the electrons. The electric field gradient of the RF gun can exceed 100 MV/m, so that the electrons reach relativistic velocity within a few millimeters. Once relativistic velocity achieved, the Coulomb repulsion stops playing a dominant role in longitudinal pulse broadening, because the impulse required to change the speed of a relativistic electron is much higher than that for a nonrelativistic electron. In addition, relativistic electron beams have little velocity spread, implying minimal pulse broadening between the gun and the target.

The buncher cavity has four cells. By imposing a negative tilt over the length of an electron pulse in its longitudinal phase-space distribution (slow electrons leading to fast electrons), the pulse can be further compressed during its flight in free space to achieve a higher electron density at a certain point. There is no overall gain or loss of the average kinetic energy of the electron pulse. This RF compressor technique has been demonstrated successful also in compact electron gun setups, which compress bunch length to around 400 fs FWHM with high brightness [25, 26]. We can see from Fig. 3.9 that MeV sources help to suppress space charge effect while buncher cavity can further compress the bunch length to sub-100 fs.

The water cooling system of the RF cavities is used for fine tuning the resonant frequency of the cavities and stabilizing the amplitude and phase of the RF field. A temperature variation of 1 degree corresponds to a phase variation of 10.5 degree. With correction from a feedback system REGAE is desired to provide a RF phase stability of 0.01 degree over ten hours, which corresponds to a timing jitter of 10 fs

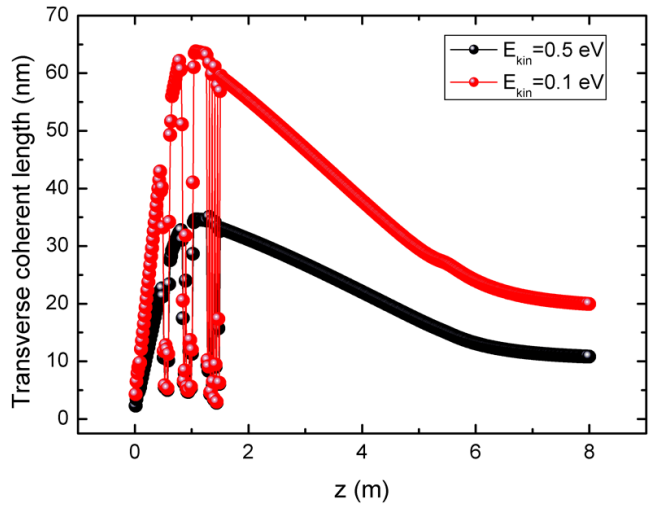

Figure 3.8: Correlation of thermal emittance to transverse coherence length. ASTRA simulation based on REGAE, see Appendix A.

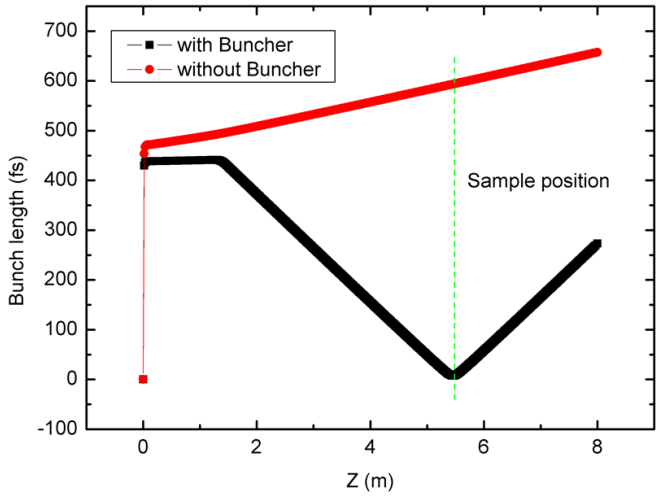

Figure 3.9: Bunch length along the beam line with and without Buncher cavity. ASTRA simulation based on REGAE, see Appendix A.

and 0.001°c temperature stability.

As the beam line extends over more than 10 meters, it is equipped with a few magnet solenoids and steerers to correct and collimate the beam. A single coil solenoid just after the RF cavity is used mainly to reduce the beam divergence. The second solenoid consists of double coils with reversed polarity. It is placed before the buncher cavity to reduce third order aberration. There are another two solenoids before and after the sample chamber for real space imaging and diffraction. A pair of Helmholtz coils is placed around the whole setup to compensate the influence of the earth magnetic field.

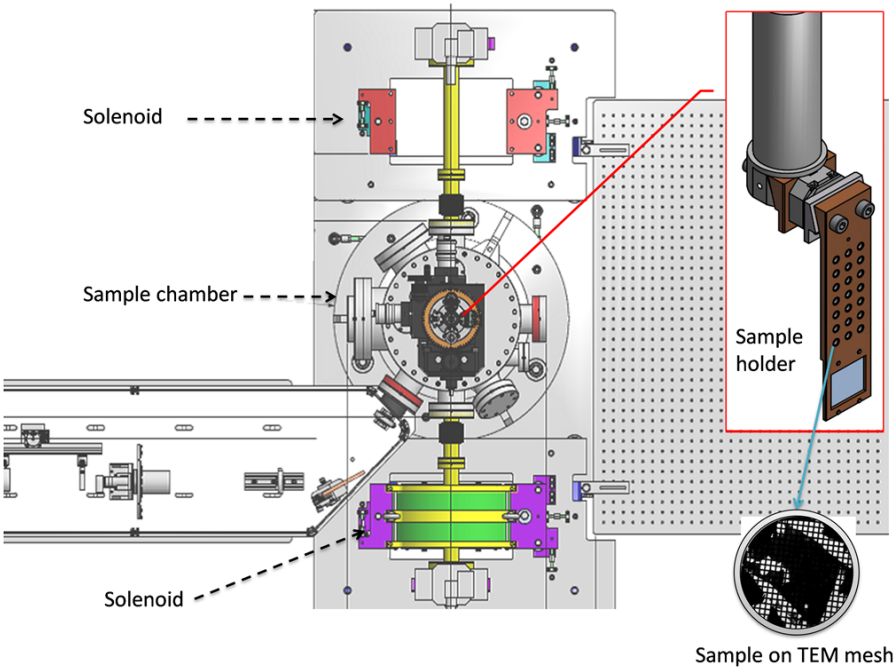

Figure 3.10: REGAE Sample chamber. Insert: sample holder.

The sample chamber (Fig. 3.10) is located 5.5 meters downstream of the cathode where the electron bunch is compressed to its minimal length. At the left side there is an imaging system, with which we can monitor the electron beam on the sample holder. Figure 3.10 (insert) shows the sample holder. The top part holds the samples that are placed on the TEM mesh. The lower part includes a LYSO (Cerium-doped Lutetium Yttrium Orthosilicate) [85] scintillator screen, which helps to characterize the pump laser and the probe electron beam quality at the sample position and optimize the spatial overlap.

In order to monitor the electron beam at different positions along the beam line, two cameras are installed after the RF gun and the Buncher cavities. LYSO scintillator screens are used at these sections to characterize the beam quality. A spectrometer dipole magnet is installed after the Buncher to measure the electron beam energy. The magnet deflects the beam by 90° onto a LYSO screen. When the beam center is in the middle of the screen the electron beam momentum can be calibrated related

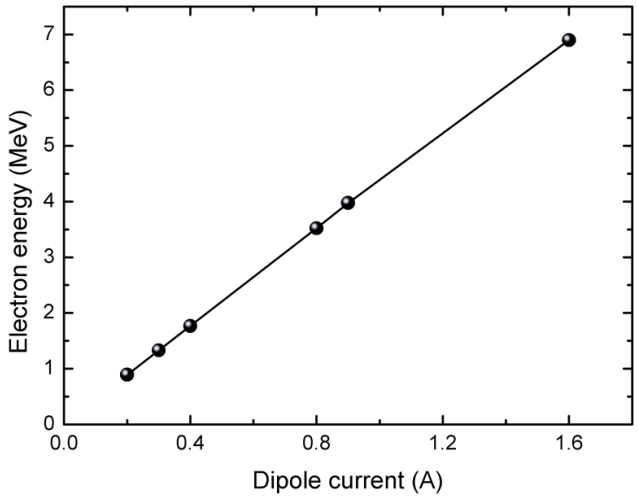

Figure 3.11: Calibrated electron energy relative to dipole current.

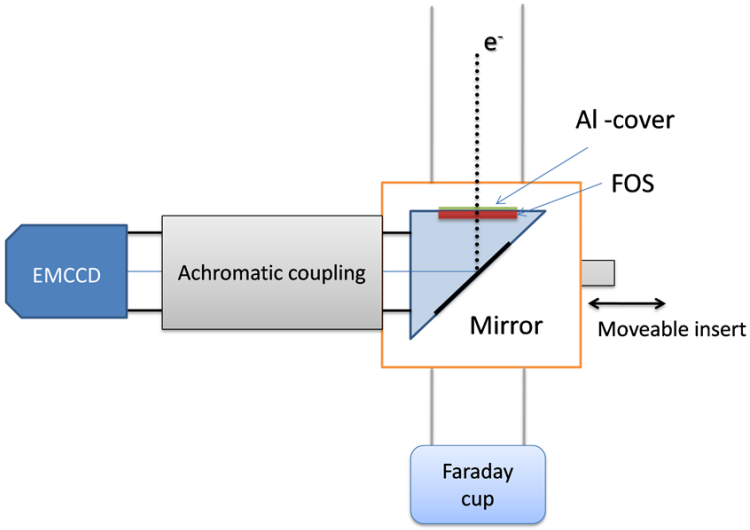

Figure 3.12: Schematic drawing of the detector system.

to the dipole current. Figure 3.11 shows the electron energy as a function of the dipole current. The machine can be operated at 2–5 MeV by adjusting the necessary acceleration field gradient. The de Broglie wavelength (λ =h/p, where h is the Planck constant and p is the beam momentum) associated with the beam is 0.5–0.23 pm for 2–5 MeV beam, which is about 10 times shorter than that for non-relativistic electrons. Four Faraday cups are installed in the beam line to check the charge at different positions [86]. Two movable Faraday cups right after the RF and the buncher cavities also incorporate a scintillator, thus offer simultaneous beam imaging and charge measurements. The other two are stationary Faraday cups placed after the spectrometer and at the end of the beam line. The detection of the diffracted electron works in an indirect way. Figure 3.12 shows a schematic drawing of the detecting system. A fiber optic scintillator (FOS) converts the energy of the electrons to photons. Afterwards the optical photons are reflected by the aluminum mirror towards the collecting optics [10]. This mirror consists of a thin silicon wafer (300 μm) and a 30 nm aluminum coating. It reflects visible light but it is transparent for energetic photons and electrons. To move the holder in and out the beam path it is mounted on a stage inside a four-way vacuum cross, which enables precise alignment and final charge measurement. Because of the relativistic velocity and accordingly small scattering angles the detector is placed 4 meters away from the sample chamber.

3.2.2. Main characteristics of REGAE (ASTRA simulation)

Figure 3.13 shows the pulse duration (a), transverse emittance (b) and coherence length (c) of the electron beam of REGAE simulated with ASTRA. In Fig. 3.13 (a), the electron pulse duration at the photocathode is almost the same as the pulse duration of the incident laser pulse ($\sim$1000 fs FWHM) and can be compressed with the buncher cavity to 20 fs. This short pulse length provides unprecedented temporal resolution and is one of the key parameters of REGAE. A small emittance allows smaller beam diameter, higher bunch charge and better coherence length. As shown in Fig. 3.13(b), the transverse emittance of the electron beam from REGAE is as small as $\sim 6 \times 10^{-3}$ mm mrad. The coherence length (L_c) of the electron beam relates to the possible spatial resolution, and can be expressed by the following equation [75]:

$$L_c = \frac{\hbar}{m_0 c} \frac{\sigma_{x,rms}}{\varepsilon_{n,rms}} = \frac{\hbar}{\sigma_p} \tag{3.3}$$

where, m_0, c, $\sigma_{x,rms}$, σ_p, and $\varepsilon_{n,rms}$ are the rest mass of the electron, speed of light, beam radius, transverse momentum spread and transverse normalized emittance of the electron beam, respectively. The coherence length of the electron beam of REGAE is calculated to be $\sim$30 nm obtained by a small momentum spread and a large beam size at the sample position (Fig. 3.13(c)), with which it will be possible to resolve protein structures in solution or crystalline phases among other more complex systems.

3.2.3. Femtosecond electron diffraction with REGAE

REGAE, with its designed much higher energy, better coherence length and shorter pulse duration, gives us higher flexibility to study more complex materials like protein

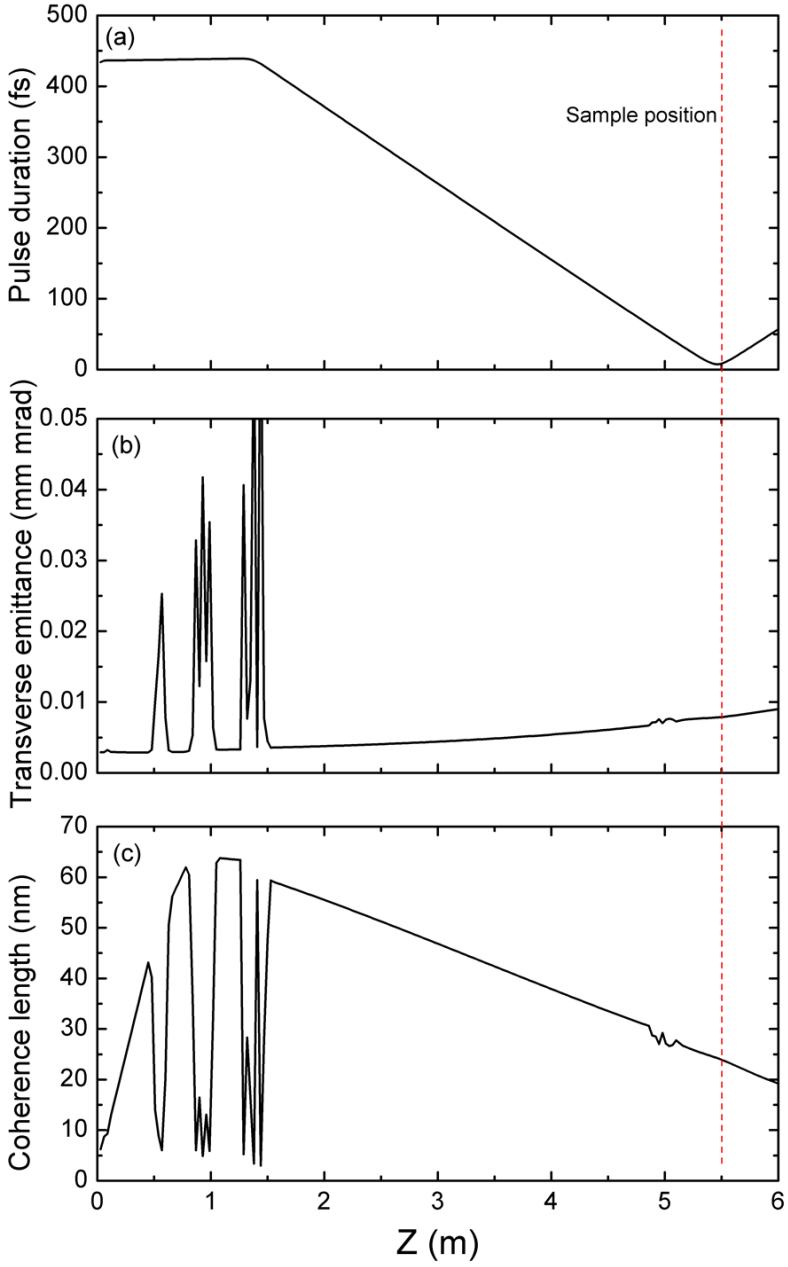

Figure 3.13: Pulse duration (a), transverse emittance (b) and coherence length (c) of the electron beam of REGAE simulated by ASTRA. ASTRA simulation based on REGAE, see Appendix A.

and DNA. Another advantage of the relativistic beams is that it eliminates the velocity mismatch between the pump laser and the probe electrons, which limits the time resolution of dilute samples such as gas phase and liquid samples.

On the other hand, REGAE is a more complex system compared to a compact electron gun setup. It requires more electronics and diagnostics along the 10 meter beam line. All controls should be remotely controlled through servers. On the control computer we develop our user interfaces for different devices and functions. Figure 3.14 shows an example of a few tools for the shutter, motor, charge measurement and so on.

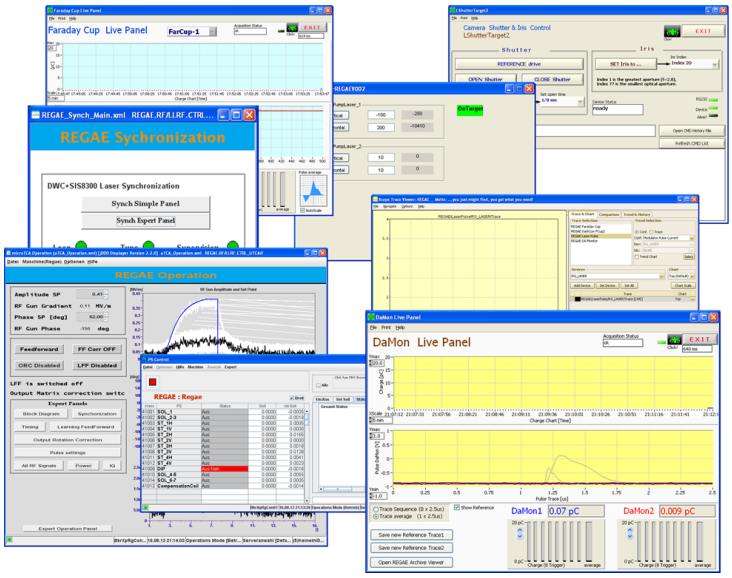

Figure 3.14: REGAE control panel. Some of the verious panels to control the machine.

Figure 3.15 is a simple schematic drawing of the REGAE pump-probe configuration. A Femtosecond laser provides power for both electron generation and sample excitation. The pump laser and probe electrons overlap in the sample chamber, which is 10 meters away from the laser source. The overall scheme is similar to the compact FED system. However it uses in addition one fast pulse picker to control the repetition rate of the pump laser as the electron beam is operated at much lower frequency (up to 50 Hz) compared with laser (1 kHz). The pulse picker includes two polarizers and one Pockels Cell that is passively controlled by the detector with a delay generator. The delay generator runs in single-shot mode with a duty cycle of two, so every cycle the detector will collect data with and without the pump.

Figure 3.16 shows the basic GUI for FED experiments at REGAE. The basic logic of the software is similar to that for a compact FED system. Here the dynamic change window is also given in the GUI, which enables simple on the fly analysis. It shows the relative transmission change (dT/T) change for a specific region of interest after each time step and helps to give us instant feedback during experiment. Further data analysis concerning background and noise correction can be done by further data analysis.

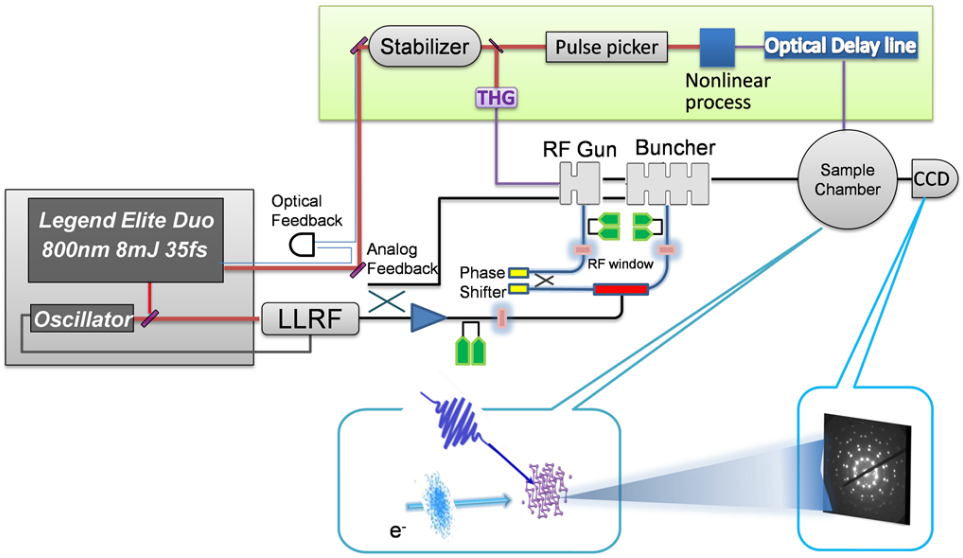

Figure 3.15: REGAE FED system. One laser beam is split into two (one for the photoelectron generation; one for the sample excitation). Pump-probe data is collected by the detector at the end of the beam line.

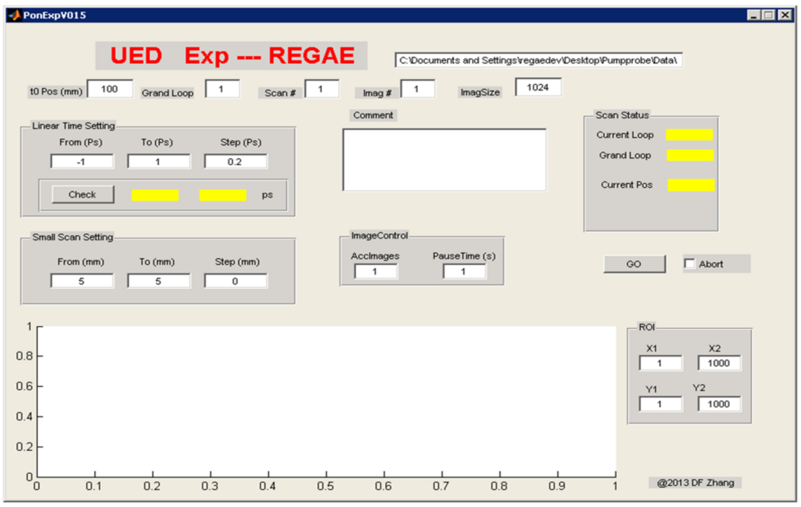

Figure 3.16: REGAE FED software. It includes the basic setting of the delay line, the CCD camera and the pump-probe operation.

3.3. Summary

This chapter discussed the two FED systems that have recently been constructed in Hamburg. The electron generation, beam line configuration and laser-electron pump-probe system were discussed in detail.

1. Egun300 is a compact table-top FED system. This is a "small" setup compared with REGAE and we have more flexibility to investigate the different parts of the system. It can provide fs pulsed electron bunches with an energy up to 150 keV and 10^5 electrons/pulse. This is sufficient for many experiments and very convenient in operation. The first study with this setup for electronic driven cold ablation in alkali halides will be discussed in Chapter 5.

2. REGAE is a much bigger system with sophisticated construction, which represents the future direction of FED setups to provide higher brightness, shorter bunch length, higher energy and larger coherence length. The excellent temporal and spatial resolution of this relativistic electron source will open up a new frontier for ultrafast electron diffraction and dynamic microscopy.

4. Hot electron driven phase transition

4.1. Introduction

The photoinduced ultrafast phenomena has been attracting increasing interest in the past few decades, which is driving the study of a variety of unconventional phenomena such as non-thermal melting [8], bond-hardening [29], vapor condensation [88], semiconductor-to-metal (SMT) phase transition [89–91], enhancement of superconductivity [92,93], and solvated electron triggered chemical reduction [94]. This also leads to the intense interest in the strongly correlated electron materials [95,96] and study of new materials that exhibit complex behavior.

One of the most well-known phenomena of these strongly correlated systems is the SMT in transition-metal oxides. SMT occurs in thermal processing [97]. The transition metal oxide usually changes from semiconductor to a more stable metal phase at temperatures higher than a critical temperature (T_c). Presently, there are two mechanisms generally believed to be responsible for the phase transition: the Peierls mechanism of electron-phonon interactions and the Mott-Hubard transition of strong electron-electron interactions [97–103]. Ultrafast optical excitation has been used to control the phase change of these materials. The photoexcited electron–hole pairs drive the lattice modification and simultaneously induce a profound change in their electrical properties, hence, the optical properties.

In particular, the vanadium oxide family (V_2O_5, V_2O_3, VO_2) has received extensive attention, which presents a noticeable resistivity change between the two phases. Among these, vanadium dioxide, VO_2, has been studied intensely in the last decade because of its large, reversible change in its electrical, optical and magnetic properties at a temperature close to the room temperature [97].

Phase	**Symmetry**	**Lattice constant (angstrom)**	**Angle (degree)**
Semiconductor, Monoclinic	$P2_1/c$, $(C_{2h})^5$	$a_M = 5.75$, $b_M = 4.54$ $c_M = 5.38$	90, 122.6, 90
Metal, Rutile	$P4_2/mnm$, $(D_{4h})^{14}$	$a_R = b_R = 4.55$, $c_R = 2.85$	90, 90, 90

Table 4.1: Lattice parameters of the metal and semiconductor structures of VO_2 [101].

Part of this Chapter is adapted from M. Hada, D. Zhang, A. Casandruc, R. J. D. Miller, Y. Hontani, J. Matsuo, R. E. Marvel, R. F. Haglund, Hot electron injection driven phase transitions, Phys. Rev. B 86 (13) (2012) 134101. Copyright 2012 by American Physical Society. [87].

The first-order SMT in VO_2 that occurs at a T_c of about 340 K has been discussed for its potential applications ranging from photoactive filters to ultrafast optical switching [104]. The SMT in VO_2 is manifested by its large changes in resistivity and dielectric functions [89, 105–107], which are accompanied by a simultaneous structural change [99, 108–110] from the low-temperature monoclinic insulating phase with a band gap of ∼0.7 eV [111] to the high-temperature rutile metallic phase (Table 4.1). Figure 4.1 shows the different structures of VO_2 with rutile and monoclinic structures.

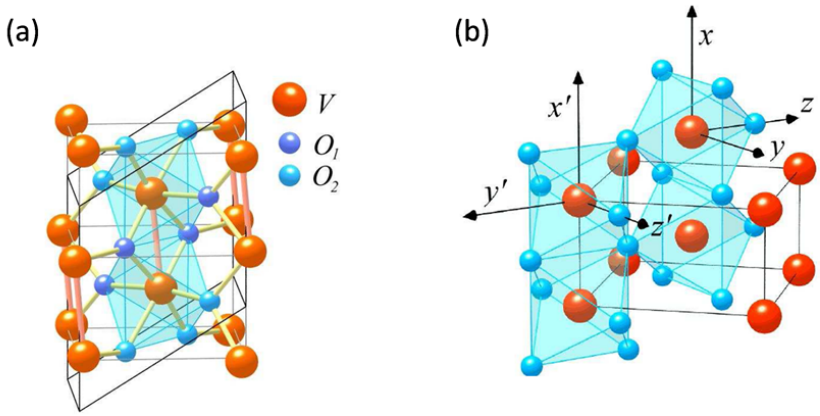

Figure 4.1: The structure of VO_2. (a) Monoclinic structure; (b) Rutile structure. Adapted from [101].

It is generally agreed that the SMT arises from the combination of Peierls and Mott mechanisms [102, 112]. With respect to the prospect of electron injection, there is a charge-transfer effect between TiO_2 (or VO_2) and a Au interface [113], which leads to the SMT switching effect for VO_2 occurring on the microsecond time scale [100]. It has also been observed that the SMT can be assisted by electron scattering due to the surface plasmon resonance comprising an array of Au nanoparticles or thin Au film (∼5 nm) covered by a thin film of VO_2 [114, 115]. In these studies, where very thin Au layers were used, the main driving force for the phase transition was the optical photons that passed through the thin Au layer and were absorbed directly into the VO_2 layer. To exclude this optical contribution, we used a thick Au layer (∼20 nm) on top of VO_2, which has a high absorption of the optical photons in the Au layer. This makes it possible for the first time to observe the effect of the injected hot electrons from the optically excited Au on the SMT phase transition of VO_2, without direct optical excitation of VO_2.

In this Chapter, a new mechanism to induce structural phase transitions by using a secondary source to photo-inject nonequilibrium electrons to alter the lattice potential will be discussed. We characterized the SMT in Au-coated VO_2 with the femtosecond pump-probe transmission experiments. In this study the Au layer serves as a photo-injector of hot electrons into the adjacent VO_2 layer for triggering the SMT process. The optical excitation pulses are absorbed almost entirely within the Au layer. The

transmitted laser beam after the Au layer is too small to optically induce the SMT directly in the underlying VO_2 substrate, however, ultrafast SMT was still observed. Through a number of control studies, the hot electron induced ultrafast phase transition was shown to be the unique trigger for the SMT change in the Au/VO_2 contact.

To elaborate the mechanism, a bias dependence experiment is performed on the multilayer, which demonstrates that the correlation of the optically induced phase transition arises from photoinduced nonequilibrium electrons originating in the Au layer as opposed to thermal transport. In this scenario, the hot electrons generated in the Au contact layer serves as the photo-injector to create conditions of nonequilibrium electrons into the conduction band of the adjacent layer, hence induce the phase transition in VO_2. The antibonding nature of these electronic states destabilizes the lattice potential, when above a critical electron density in the conduction band, leads to lattice instability and ensuing structural transition.

4.2. Experimental setup

The experimental setup uses the optical pump-probe setup with lock-in amplifier in the transmission mode as described in Chapter 2. The 1-kHz femtosecond laser system provides the excitation wavelengths at 800 nm (pulse duration: ∼40 fs) and the probe wavelengths at 400 nm (pulse duration: ∼70 fs). The 800-nm optical pump beam was focused on the sample at an incident angle of 4° with respect to the surface normal, and the 400-nm probe pulse is focused on the excited spot at an incident angle of 30°. The transmission of the sample was detected using the standard lock-in methods with a 500 Hz optical chopper. The samples were prepared with a polycrystalline 30 ± 1 nm thick VO_2 layer fabricated on a sapphire window or Indium tin oxide (ITO) substrate by electron beam evaporation. Some of these samples were subsequently coated with Au films (20 ± 1 nm thickness) by thermal evaporation. VO_2/sapphire, Au/sapphire, Au/VO_2/sapphire, and Au/VO_2/ITO multilayer samples were characterized in the experiment.

Sample	Reflection	Transmission
VO_2/sapphire	28%	57%
Au/sapphire	78%	17%
Au/VO_2/sapphire	76%	18%
Au/VO_2/ITO	75%	16%

Table 4.2: The measured reflection and transmission from each sample (VO_2/sapphire, Au/sapphire, Au/VO_2/sapphire, and Au/VO_2/ITO).

VO_2/sapphire and Au/sapphire samples are used as standard material for comparison. Hot electron induced phase transition effect were observed from Au/VO_2/sapphire. To elaborate the mechanism we extend the experiment to use a transparent conducting material ITO as a buffer layer. A variable bias was introduced for the Au/VO_2/ITO multilayer sample (Fig. 4.2) as a control to determine if the effect arose from ballistic electron transport, as opposed to thermal transport effects, which would not be bias

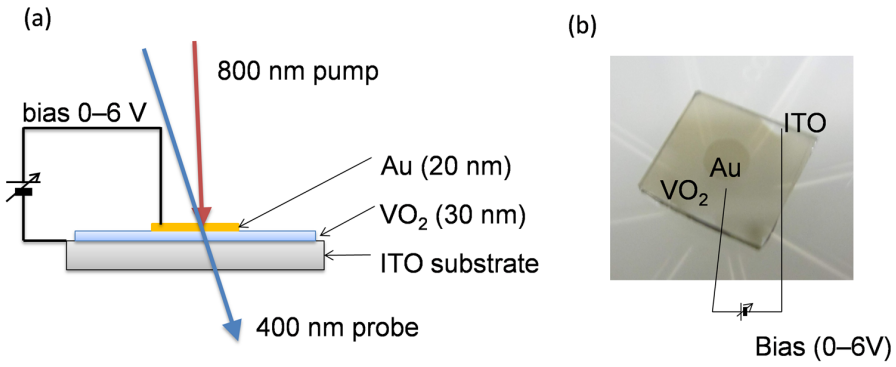

Figure 4.2: (a) The structure of the $Au/VO_2/ITO$ sample with the pump-probe beam geometries and bias. (b) photo of the $Au/VO_2/ITO$ sample.

Sample	Absorption
VO_2/sapphire	15%/0%
Au/sapphire	5%/0%
Au/VO_2/sapphire	4%–5%/1%–2%/0%
Au/VO_2/ITO	4%–5%/1%–2%/3%

Table 4.3: The absorption of the incident laser intensity of each sample (VO_2/sapphire, Au/sapphire, Au/VO_2/sapphire, and Au/VO_2/ITO).

dependent. The optical reflectivity and transmission in each sample were measured and given in table 4.2. The absorption of the incident intensity of each sample can be calculated (Table 4.3). The complex refractive index of Au is 0.18–5.11i at the wavelength of 800 nm. However, this Au film was made by the thermal evaporation and the surface of the material is not perfectly flat; therefore, the real part of the refractive index of the Au layer would be 0.2–1. According to Snell's law, the optical penetration depth in the Au film with an incident angle of 4° would be longer than the film thickness (20 nm).

4.3. Optical pump-probe results

Photoinduced phase transition results in the change of transmission ($\Delta T/T$) as a function of the time. The measured results for VO_2/sapphire, Au/sapphire, and Au/VO_2/sapphire are shown in Fig. 4.3.

The typical photoinduced phase transition behaviour can be observed in the time-resolved transmission curve for the VO_2/sapphire sample (Fig. 4.3 (a)). A sub-picosecond insulator-to-metal transition with an abrupt change in the optical properties of the system results in an increase of the reflectivity and a decrease in the transmission, which is consistent with previous reports [91]. The observed reflectivity/transmission changes persist for tens of nanoseconds and correspond to changes in the complex refractive index, between the equilibrium low-T and high-T. The threshold of the absorbed laser fluence for the SMT of this sample is derived to be $\sim$1 mJ/cm^2 (incident fluence $\sim$7 mJ/cm^2) [99, 105, 106, 109]. This excitation level is equivalent to 4×10^{15} photons/cm^2 with the excited VO_2 volume (1 cm$^2\times$30 nm) containing 9.4×10^{16} valence band electrons. Thus, the optically driven phase transition occurs when about 4% of valence-band electrons are excited to the conduction band.

After the excitation in the Au/sapphire sample (Fig. 4.3(a)), thermal equilibrium among the excited electrons is reached within several hundred femtoseconds, depending on the excitation energy above the Fermi level. Once it is established, slow relaxation will be observed, which can be described by a two-temperature model (Cooling of the electrons proceeds by electron–phonon coupling and diffusive motion) [116, 117].

Above the absorbed laser fluence of $\sim$2 mJ/cm^2, the time-resolved transmission in Au/VO_2/sapphire starts to show similar contributions as that of the directly photoinduced SMT in VO_2. The sudden reduction of the time-resolved transmission in the first 300 fs of Au/VO_2/sapphire results from excitation of the bulk plasmon in the Au layer, which follows with a broad oscillation around 10 ps attributed to the acoustic strain in the Au film. The frequencies (f_n) that fulfill the standing wave condition are given by [118]:

$$f_n = \frac{nv}{2d} \tag{4.1}$$

where v is the speed of sound along a given direction, d is the film thickness , and n is an integer number characterizing the different modes. The speed of sound in Au is 3240 m/s and the thickness of the Au film is 20 nm, therefore, the frequency of

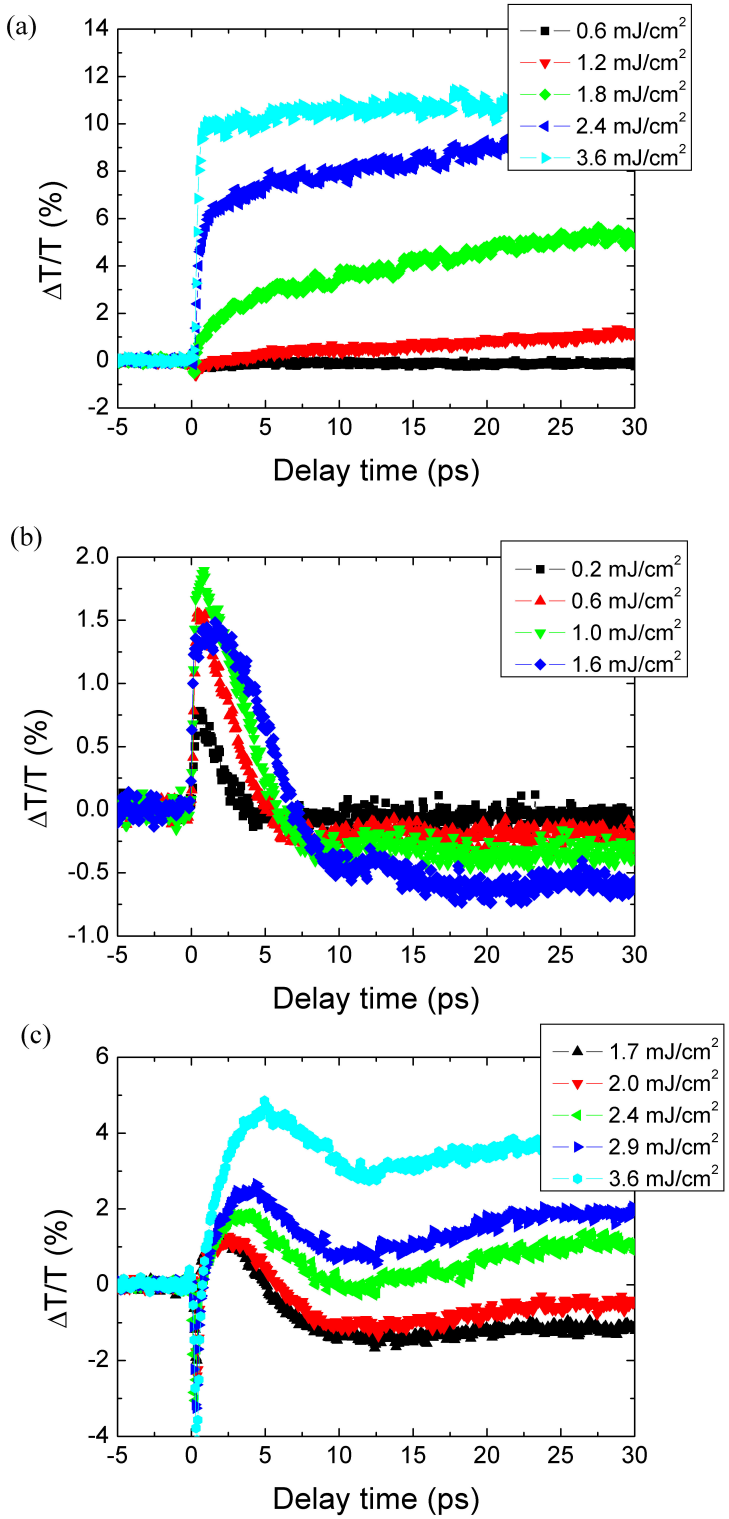

Figure 4.3: Changes in differential transmission with delay time for VO_2/sapphire (a), Au/sapphire (b), and Au/VO_2/sapphire (c).

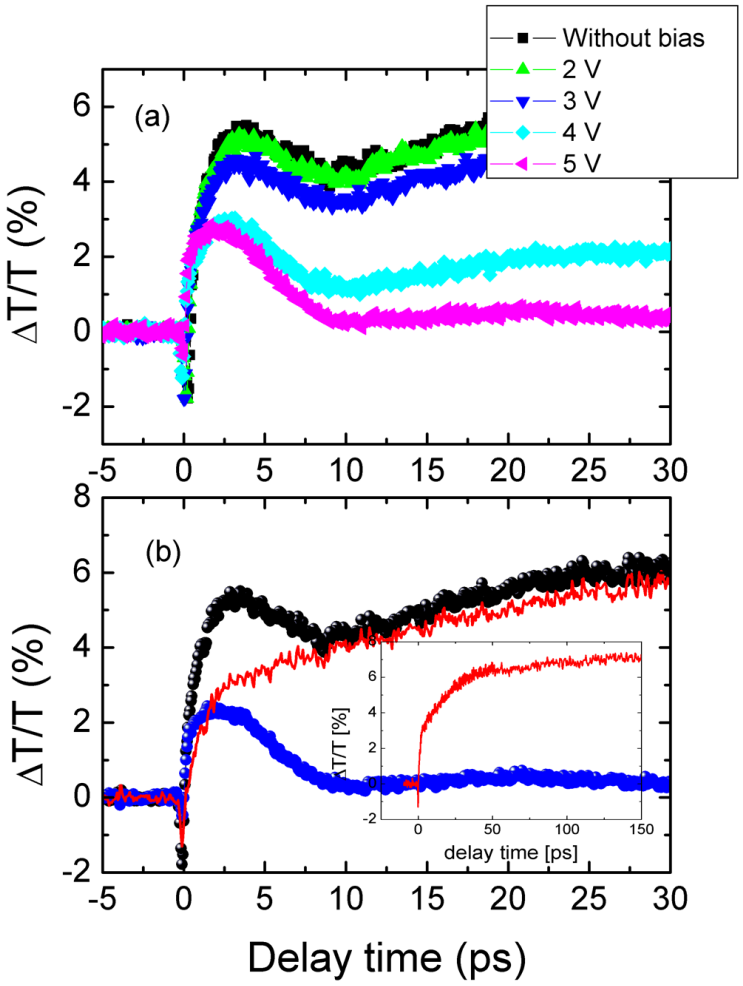

Figure 4.4: (a) Changes in transmission as a function of the delay time for $Au/VO_2/ITO$ with bias assistance at an absorbed laser fluence of 3.2 mJ/cm^2. (b) Subtracted change (red) in the transmission of $Au/VO_2/ITO$ with the bias voltage of 6 V (blue) from that without bias (black); insert: the subtracted change with longer delay time.

the acoustic oscillation can be calculated to be 81 GHz with the period around 12 ps. This value corresponds to the period of the oscillation in Figs. 4.4 (a) and 4.3 (c). It is important to note that, due to the attenuation by the Au film (less than 1% pass through), this level of excitation is at least four times less than that needed to observe the direct photoinduced SMT in VO_2.

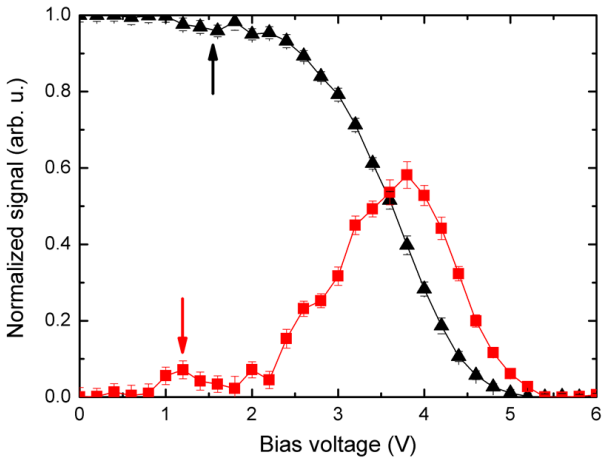

Figure 4.5: The normalized SMT signal ($\Delta T/T$) at the delay time of ~100 ps as a function of bias voltage (black curve). The difference signal with and without bias at 100 ps was normalized to the difference signal without an applied bias. The red curve shows the derivative of this response to highlight the minimum observed at 1.5 V (indicated by the black arrow) and the inflection point for maximally reducing the electron distribution in the VO_2 half space.

In the control experiment, a variable bias (0–6 V) was applied to the Au/VO_2/ITO structure to inhibit the spatial distribution of both equilibrium and nonequilibrium electrons. Figure 4.4(a) shows the time-resolved transmission from the Au/VO_2/ITO multilayer samples with variable bias (0–5 V) at an absorbed laser fluence of 3.2 mJ/cm^2. As ITO is almost transparent at visible wavelength, the time-resolved transmission from Au/VO_2/ITO without bias is similar to that from Au/VO_2/sapphire. However, ITO is an electrical conductor. It enables us to apply a bias on the Au/VO_2/ITO multilayer. With the increasing bias, i.e., as the hot electrons generated in the Au layer were more confined to the Au layer, the transmission decreased, which indicates a reduced contribution of the SMT in VO_2 to the time-resolved transmission (Fig. 4.4(a)). Almost no phase transition in VO_2 can be observed with a bias voltage of 5 V, which can be seen in Fig. 4.4(a). After 10 ps the changes in transmission relax back to around zero. Figure 4.5 shows the SMT signal at fixed delay time of around 100 ps. A threshold effect at approximately 3 V is observed, which is directly related to the electronic temperature of the hot electron distribution excited in the Au layer.

The time-resolved transmission has shown several complex effects from photo-electron coupling, electron diffusion, ionic motion, and phonon excitation. The applied bias voltage modifies the spatial distribution of the hot electrons within the VO_2

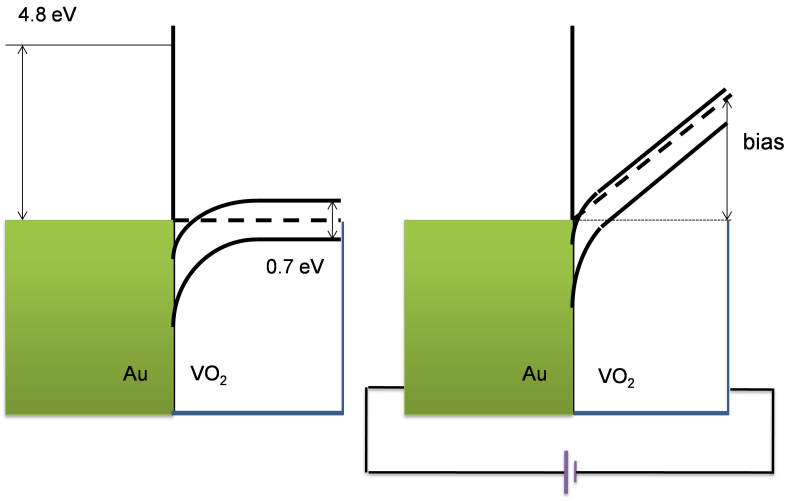

Figure 4.6: The electron band diagram of Au/VO_2 for ohmic contact. The spatial distribution of the generated hot electrons penetrating into VO_2 will be affected by the potential barrier created by the applied bias.

layer, which is illustrated in Fig. 4.6. Subsequently it isolates the effects of the hot electron distribution with the ensuing dynamics. Another possible mechanism the thermal transport will not be affected by the applied bias. Therefore, the subtraction of time-resolved transmission from $Au/VO_2/ITO$ with the bias voltage of 6 V from that without bias provokes that the changes in transmission invoked solely by transport of electrons into the VO_2 layer. From the subtracted data shown in Fig. 4.4 (b), we can see two distinct temporal components involved in the phase transition in Au/VO_2 and associated changes in reflectivity. The first one is a fast nonthermal component of around 2 ps and consequently the second one is a slower thermal relaxation component of 40–50 ps.

4.4. Discussion

Another potential trigger for the phase change is thermally driven stresses that can induce an increased pressure in the phase diagram. This mechanism would develop at the speed of sound. Considering only the VO_2 layer, the speed of sound is $\sim$4000 m/s [119], and the acoustic stress wave would require about 10 ps to propagate across the VO_2 layer (Eq. 4.1). The relaxation of the hot electrons into this acoustic mode takes place on a 5 ps time scale as directly derived from above. This mechanism is much slower compared with the fast component (2 ps) observed in the SMT response. However, the slow SMT component observed in Au/VO_2 samples is more consistent

with a thermal contribution, where the hot electrons generated within the Au layer relax into lattice phonons and increase the effective lattice temperature. Similarly, any hot electrons injected into the VO_2 will subsequently relax into the lattice phonons in the VO_2 half space. The thermal profile across this interface will depend on the fraction of hot electrons transferred to the VO_2. This difference in the lattice temperature provides the fraction of hot electrons transferred to the VO_2. The associated difference in the lattice temperature reflects the gradient for thermal diffusion from the Au into the VO_2 layer. Based on the thermal diffusivity of Au, the observed time scale of the slow component in the optical measurement is consistent with a thermal diffusion contribution from the Au to the VO_2 layer. This clear separation in time scales (fast nonthermal and slow thermal component) enables a determination of the purely electronic and thermal or nuclear motions on the lattice dynamics. That is normally not readily separable from observation of direct photoinduced transition.

The hot-electron-induced phase transition is significantly slower than the direct photo-excitation process as can be seen in Fig. 4.4(insert) and Fig. 4.3(a). The excitation laser produces a significant number of hot electrons in the Au layer, which subsequently transport into the underlying VO_2. The energy of the hot electrons capable of inducing the SMT in VO_2 can be inferred from the time-resolved transmission measurements with varying bias voltages. The hot electron distribution in the VO_2 layer can be attenuated by the applied bias. However, when the potential barrier is smaller than the energy of the hot electrons, these nonequilibrium electrons will freely propagate into the VO_2 layer, as illustrated in the known band junctions shown in Fig. 4.6. The Au and VO_2 interface makes an ohmic contact, which results in a linear current-voltage (I-V) curve across the VO_2 layer. The bias voltage increases uniformly in VO_2 [113]. The hot electrons generated within the Au layer will experience transport conditions under the influence of the initial excess spatial distribution within the Au layer and the triangle potential produced by the bias within the VO_2 region. As can be seen from Fig. 4.5, there appears to be a small drop at the bias of about 1.3–1.5 V, which is related to the band gap of VO_2 in the semiconductor phase (0.7 eV) considering the ohmic contact between VO_2 and Au.

We can use the observed bias dependence to estimate the number of injected electrons required to induce the phase transition in VO_2. The energy of the hot electrons can be assumed to be half the bias voltage ($\sim$1.5 eV), under which condition appreciable attenuation of the SMT is observed. This phase transition process would be governed by ballistic electron transport. Nevertheless, the temperature of the hot electrons (T_{hot}) produced in the Au layer can be roughly estimated from the absorbed laser fluence (P) and electron heat capacity (C_s = 67.6 $JK^{-2}m^{-3}$) as [120]

$$P = \int_{T_{room}}^{T_{hot}} C_s t dt = \frac{1}{2} C_s (T_{hot}^2 - T_{room}^2) \tag{4.2}$$

where T_{room} is the room temperature (293 K). The hot electrons generated in the Au layer would be transported ballistically through the 20 nm layer within 100 fs. According to Eq. 4.2, the temperature of the hot electrons at the threshold (with absorbed laser fluence of 2 mJ/cm^2) would be 5500 K (0.5 eV). According to the Fermi-Dirac distribution

$$f(E) = \frac{1}{e^{(E-E_F)/K_BT} + 1} \tag{4.3}$$

where $f(E)$ is the occupation probability of a state of energy E, K_B is Boltzmann's constant, E_F is the Fermi energy and T is the temperature in Kelvin. The density of the hot electrons with the energy of 1.5 eV or greater in the excited Au film is 4.7×10^{15} electrons/cm^2 (4% of the valence band electrons in the Au layer). This number of excited, nonequilibrium electrons corresponds to the case of the direct photoinduced SMT in VO_2. The penetration depth of the 1.5 eV electrons in VO_2 is a few nanometers. They will induce the SMT in VO_2 through the direct injection and primary scattering processes to give a nonequilibrium distribution within the VO_2. This change in electron distribution is sufficient to change the lattice potential to favor the metallic phase.

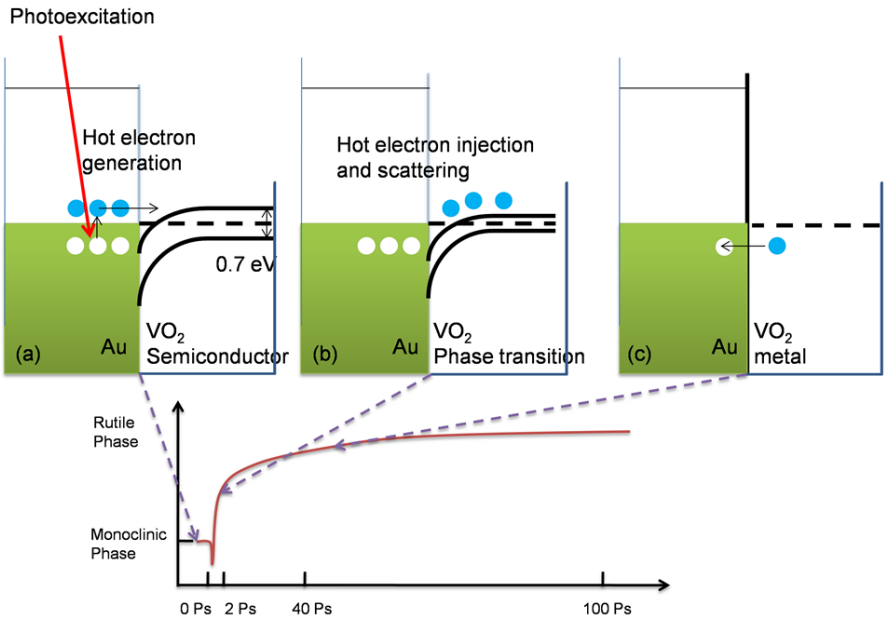

Figure 4.7: (a) Schematic band diagram of Au/VO_2; (b) the hot electron injection from Au layer to VO_2 layer, which leads to the SMT in VO_2; (c) the hot electrons recombine with the holes at the interface of the Au and metallic VO_2 to trap the system in this metastable phase. The figure underneath indicates the time scale of the phase transition.

The coupling mechanism between the Au and VO_2 layers during the phase transition can be attributed to two equivalent interpretations for the production of nonequilibrium electrons within the VO_2 that lead to this SMT phenomenon. One scenario is that the excited electrons generated in the upper Au layer undergo ballistic transport to the VO_2 layer with a speed of around 10^6 m/s [116], and they would pass through Au (20 nm thickness) and VO_2 (30 nm thickness) layers in around 100 fs. These energetic electrons contribute both nonthermally and thermally through subsequent

relaxation processes to the phase transition in VO_2 in a few picoseconds, however, the nonthermal contribution dominates in this process. The other scenario is that nonequilibrium electrons undergo transport through the contact between the Au and VO_2 with electron-phonon coupling. The contact between Au and VO_2 (semiconductor phase) is Ohmic. The exact scenario for nonequilibrium transport between Au and VO_2 does not change the mechanism of the driving force for the observed SMT. The optical pulse generated hot electrons in the Au layer whose energy distribution is sufficiently below the work function of Au, but was nevertheless sufficiently high for the electron to tunnel into the conduction band of VO_2 (Fig. 4.7(a)). Through the direct injection (non-thermal effect) and primary scattering (thermal effect), the injected hot electrons will transfer the energy to the cold VO_2 lattice, which could trigger the SMT in 2 ps (Fig. 4.7(b)). Accompanying the SMT is the evolution of an overlap between the conduction and valence bands [91], which leads to a bandgap collapse (Fig. 4.7(c)). Consequently, the doped electrons can recombine with the holes at the interface of the Au and metallic VO_2 to trap the system in this metastable phase until thermal relaxation over the barrier completes. It would be interesting to extend the time scale to observe the full recovery of the system back to the semiconducting phase. There is apparently a barrier to subsequent relaxation that traps the system for time scales in excess of the 1-ns dynamic range of the present experiment. It should also be noted that, with full thermal equilibrium between the Au and VO_2 half spaces, the lattice temperature is above the phase transition temperature of VO_2 such that the subsequent relaxation back to the semiconducting phase will be dictated by thermal cooling of the structure.

4.5. Conclusion

In conclusion, this chapter discussed the ultrafast SMT in a Au/VO_2 system in the conventional optical pump-probe experiments, with the assistance of an applied bias to separate nonthermal electronic and thermal effects. Photon induced hot electrons generated in the upper Au layer penetrates into the underlying VO_2 layer. The hot electrons couple with the cold lattice in VO_2 immediately through ballistic transport across the interface and trigger the SMT in VO_2 on the timescale of 2 ps. This result suggests that hot electrons have the potential to induce structural changes in a number of materials that undergo phase transition.

4.6. Future outlook

As a further application, it is interesting to note that, with thermal- or voltage-assisted hot electron excitation, it is possible to achieve ultrafast phase transitions in transparent materials that cannot be excited by optical pulses. This hot electron assistant phase transition mechanism could be particularly important as a general optical trigger of critical phenomena to fully exploit the recent advances in ultrabright x-ray and electron sources for the atomically resolved structural dynamics.

In favor of this, it would be interesting to see hot electron driven phase transition atomically with the newly designed FED system (see Chapter 3). It is not trivial to

fabricate high quality VO_2 samples. The thin VO_2 film that we have always show polycrystalline rings. And it is hard to distinguish them with the polycrystalline gold diffraction. Therefore we have chosen another system – Al/Si bi-layer, which is more suitable. Silicon has been investigated with FED experiment to see both the acoustic phonon and the non-thermal melting processes [28, 81]. When 10% of the valence electrons are excited, the lattice is no longer a bound state and it collapses to a disordered structure through a purely electronic effect. The question is whether (or how) hot electrons can trigger this phase change?

We can get very high quality single crystalline silicon, as has been shown in Introduction (Fig. 1.2). In this case, aluminum is chosen as the medium to generate hot electrons. Al is lighter than Au. Its diffraction signal is weaker and its diffraction rings are better distinguished from silicon compared with that from gold. A 20-nm polycrystalline Al is coated on top of the 49-nm single crystalline silicon via thermal deposition. Al on silicon will form a schottky barrier, which is normally in the range of 0.4–1 eV [121, 122]. We can use 800 nm pump laser focusing on the sample to generate hot electrons. The penetration depth of 800 nm light in Al is below 10 nm, the range of ballistic electron transport is on the order of 46 nm [117]. The hot electrons will then penetrate into the silicon layer and induce the phase change.

Fig. 4.8 shows the first diffraction from this bi-layer sample and we can see clearly the single crystalline diffraction dots from silicon, while Al shows the polycrystalline rings. They are well distinguished. Therefore, if the hot electrons could induce non-thermal melting in the underlying silicon layer, we should see a fast collapses of Si lattice in less than 500 fs. However, if only thermal effect happens, much slower (a few ps) dynamics will dominate.

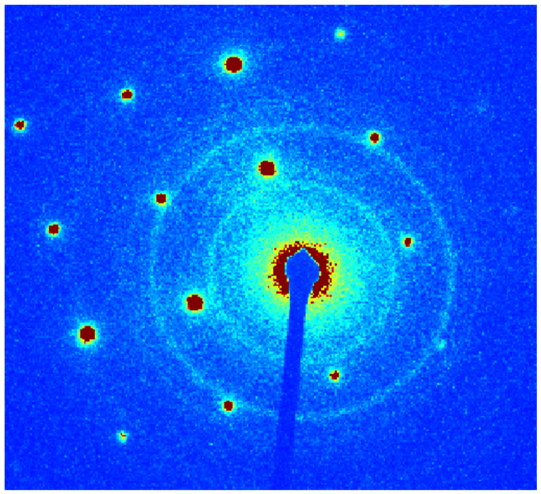

Figure 4.8: Electron diffraction from Al/Si multilayer thin film (Al: 20 nm, polycrystalline; Si: 49 nm, single crystalline).

5. Electronically-driven ablation via highly localized electronic states

.

5.1. Introduction

Laser ablation [123–126] involves many-body interactions. It is a collective response to optical excitation, which will lead to material removal. The ablation processes on metals, semiconductors and dielectric materials drastically diverse in terms of the band-gap and the bulk electron mobility. These processes in semiconductors and metals with femtosecond laser pulse are well investigated [123–127]. Absorption occurs at the surface of the material on the femtosecond time scale. At low photoexcitation intensities the solid surface is heated up by the absorbed laser energy on the picosecond time scale and the material thermally evaporates or sublimes on the nanosecond to microsecond time scale. At higher laser peak power (incident laser fluence: $F \sim 100$ mJ/cm^2), the system is often pushed into a metastable phase as a result of rapid heating, where the phase separation follows from large, local, density fluctuations, i.e., homogeneous bubble formation in the metastable liquid state [127]. With even higher laser fluence ($F > 1$ J/cm^2), the solid surface directly changes into gas via multi-photon ionization. This often leads to the plasma formation ($F \sim 10$ J/cm^2) resulting in the ejection of charged materials due to strong space-charge effects [128]. This process, also known as cold ablation, is a direct ablation bypassing melting, and relies on the effective channeling of cohesive energy into translational degrees of freedom.

The laser absorption processes [129, 130] in dielectric materials vary from that in metals and semiconductors because the single-photon energy of most fs laser pulses (infrared-to-visible range-wavelength) does not exceed the band-gap of the dielectric materials, which make them highly transparent. The absorption of photon energy of the fs laser pulses to the dielectric materials is dominated by nonlinear processes such as multiphoton absorption/ionization and avalanche ionization. Once the photons are absorbed into the material, they create elementary electronic excitations, which relax their energy into the material through carrier-to-lattice interaction channels. The energy stored in the electron-hole pairs creates self-trapped excitons (STEs), self-trapped holes (STHs) and different short-lived precursors, which provide the energy to rearrange the lattice and generate long-lived defects (colour centres) [131–146]. Series of experiments have been performed with moderate photoexcitation (F = 1–10

Part of this Chapter is adapted from M. Hada*, D. Zhang*, K. Pichugin, J. Hirscht, M. A. Kochman, S. A. Hayes, S. Manz, R. Y. N. Gengler, D. A. Wann, T. Seki, G. Moriena, C. A. Morrison, J. Matsuo, G. Sciaini, and R. J. D. Miller, *"Cold ablation driven by localised forces in alkali halides," submitted to Nat Commun*. (∗ equal contribution)

mJ/cm^2) of fs laser pulses by detecting the ions emitted from the surface of alkali halides [133–136]. These results have linked the irradiation of alkali halides and the ablation/desorption processes. At high photoexcitation (F > 1 J/cm^2) the ablation process due to the Coulomb explosion driven by the plasma formation on the dielectric materials is also discussed [145, 146].

With the development of femtosecond X-ray and electron techniques, a series of materials have been studied with atomic resolution. In aluminum, for example, melting is governed by heat transfer from the excited electrons to the initially cold lattice [6]. In semiconductors and semimetals like silicon and bismuth, femtosecond optical excitation can change the potential energy surface such that leads to non-thermal melting [8, 28]. With much higher fluence it is normally believed to be plasma generation that leads to the material removal. But most of the studies are based on a free electron metal system or a semiconductor with shared electrons. In this regard, a system with localized electrons like the alkali halide crystals are interesting systems to interrogate since UV-photoexcitation drives the excited halide centres into highly repulsive and dissociative states [127]. It is normally believed to be plasma and thermal melting that drive the ablation process, however, the underlying mechanism has not been studied in detail.

In this Chapter we have investigated the mechanism and driving force of ablation of dielectric material under the intermediate-range photoexcitation (F $\sim$ 100 mJ/cm^2), which has not been fully explored. We performed single-shot fs electron diffraction [147], fs optical reflectivity and ion detection studies to link the bulk structural and electronic changes to the nature of the ablation process. Our results reveal the development of an ultrafast lattice-disordering process that would lead to ejection of large cluster and/or fragments and the formation of micron-deep craters. This cold laser ablation occurs well below both the threshold for plasma formation and the melting point of the salt, which reflects the strength of electronic driven repulsive forces at play.

5.2. Results and discussion

5.2.1. Time-resolved optical reflectivity measurements

The single-shot optical pump-probe experiments were performed in the before mentioned optical pump-probe setup in Chapter 2 (Fig. 2.21). Optical pump pulses of 400 nm (3.1 eV), 70 fs, s-polarized with an incidence laser fluence of 35–1100 mJ/cm^2 were focused on the sample at an incident angle of 30° (from the surface normal), and the 800-nm 40 fs p-polarized probe pulses or white-light probe pulses were focused on the excited area with an incident angle of 60°. The reflected signal were registered with slow photodiode ($\sim$100 μs response time) for the infrared probe or using optical spectrometer (Avantes) when the dynamics were studied with the white light.

We investigated three different alkali halide crystals (NaCl, CsI, and KI) exposed to UV-fs-photoexcitation. Time dependent measurements on the change of reflectivity after excitation have been performed and visualized in Fig. 5.1. As a reference system, Si is chosen because its fs-laser melting and ablation processes are well understood

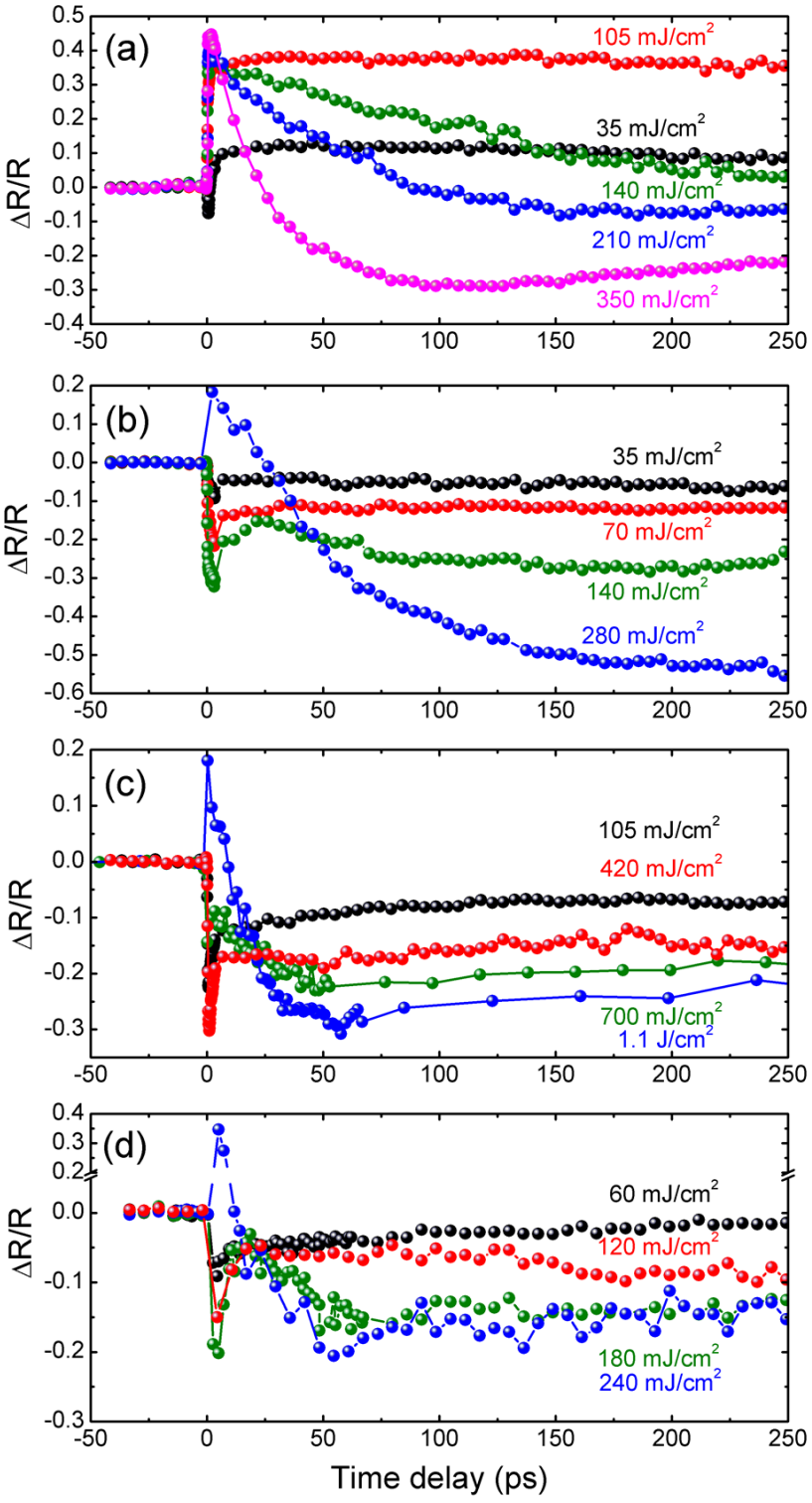

Figure 5.1: Relative reflectivity changes as a function of the time delay, (a) for Si, (b) for CsI, (c) for NaCl and (d) for KI. The incident laser fluences corresponding to the curves in each plot are indicated in the figures.

[148–154]. Thermal melting for Si is expected to occur for incident laser fluences in the range of 35–70 mJ/cm^2, and it becomes apparent as an increase in reflectivity during the first ∼5 ps (black traces in Fig. 5.1(a)) due to the gain of metallic character caused by the formation of liquid Si [149]. Laser fluences of 70–100 mJ/cm^2 correspond to about 9% of valence carrier excitation, which is known to trigger a much faster nonthermal disordering process [5, 28, 155–158] that takes place on a time-scale of 200–400 fs. This effect correlates with a very sharp increase in reflectivity observed in the sub-500 fs temporal span (red trace in Fig. 5.1(a)). The decrease in reflectivity occurring on the 100-ps time scale is due to surface removal caused by the ablation processes corresponding to the spallation, phase explosion, and fragmentation of the material. A similar but more pronounced effect is also observed for the fluencies higher than 200 mJ/cm^2 (see green, blue and magenta traces in Fig. 5.1) [159–161].

The reflectivity changes in NaCl, CsI and KI samples (Figs. 5.1(b-d)) are quite similar to each other, but dramatically different from that in Silicon. A fast decrease of 20–30% is observed within the first 500 fs followed by longer-term changes.

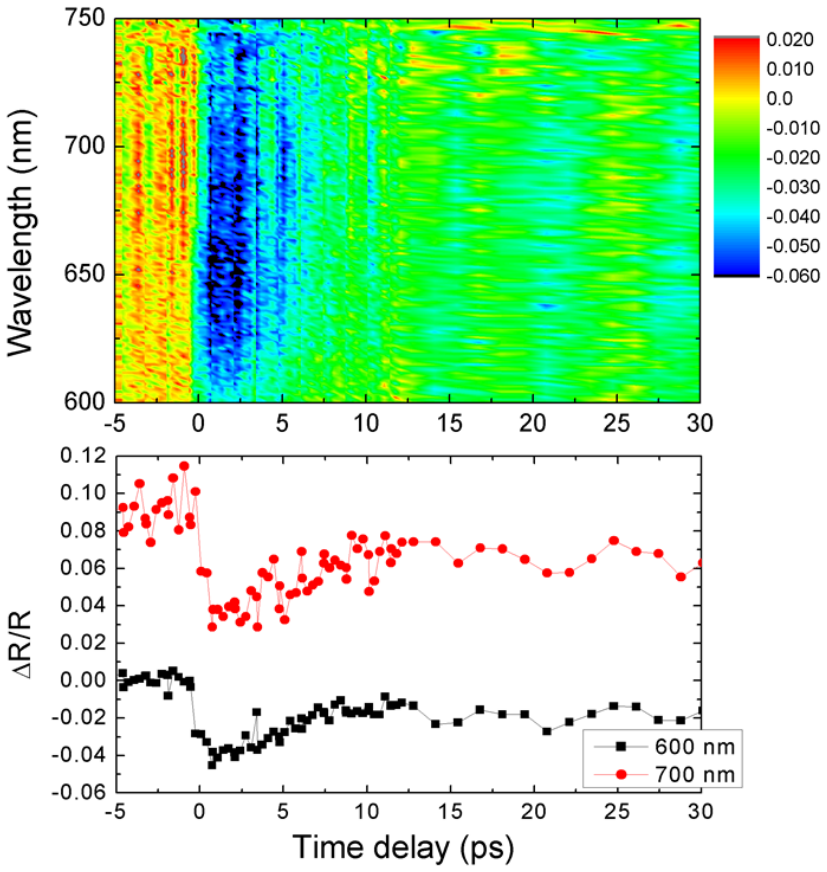

Figure 5.2: Time-resolved reflectivity changes from CsI in the wavelength range of 600–750 nm, F = 70 mJ/cm^2. Line profiles of reflectivity changes at two different wavelengths (600 nm and 700 nm) are presented in lower panel.

To exclude the influence of probe in regard to different wavelengths, we used white light as the probe. Figure 5.2 shows the spectroscopic time-resolved reflectivity changes in CsI. The lower panel in Fig. 5.2 presents the reflectivity changes at probing wavelengths of 600 nm and 700 nm. The behavior of the reflectivity for CsI shows the same trend throughout the whole wavelength range of 600–800 nm. It further indicates that the change is permanent and independent of the probe wavelength. However, it is still unknown what the underlying force is. It is normally believed to be charged particles that create this long-term change during plasma generation. Ion measurement would help to understand the contribution of plasma effect during this cold ablation process.

5.2.2. Ion measurement

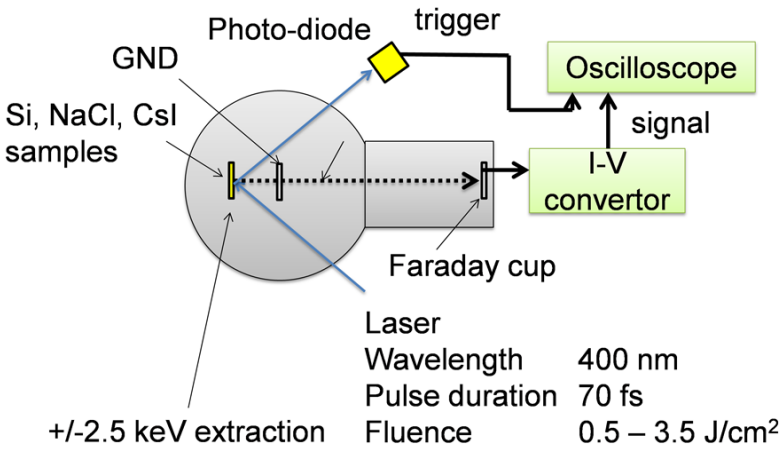

Figure 5.3: Experimental setup for the ion measurement. Sample, extraction electrode and Faraday cup are in high vacuum (10^{-6} mbar).

In order to estimate the threshold fluence for the ablation, we performed simple ion detection measurements to establish the total number of the low (up to 4000) m/q ions emitted from the laser irradiated materials. Figure 5.3 shows the schematic of our home-made setup. The ion measurement system comprises an extraction electrode at 2.5 kV (with positive or negative polarity), a 200 mm long drifting tube, a Faraday cup connected to an I-V converter, an oscilloscope and a sample holder on a translation stage at ground potential. A knife edge for beam diameter measurement is mounted together with the sample, which is parallel to the sample surface. The ions generated by each incident pump pulse of 400 nm, 70 fs are extracted by the electrode and detected by the Faraday cup. The reflection of the incident pump pulse at the sample's

surface is used to trigger the oscilloscope measurement. After each shot the sample is moved to a fresh position. It was averaged five times for each fluence value.

Figure 5.4 shows the yields for positive and negative ion detection as a function of fluence for Si (a), NaCl (b) and CsI (c). The aforementioned reflectivity measurements were found to be in good agreement with the observed threshold for the detection of positive or negative Si ions $F_{th} \approx 200$ mJ/cm^2, which is also in good agreement with previous studies [149]. As shown in Fig. 5.4(a), the number of the detected ions drastically increases at around 800 mJ/cm^2, which was attributed to the gaseous plasma formation. According to the literature [162], this process becomes dominant for F > 1 J/cm^2. As a similar manner in the previous studies, we define the ablation threshold (Si: $F_{abl} \approx 200$ mJ/cm^2) as the laser fluence when the increase and following decrease of optical reflectivity were observed. The plasma threshold (F_{plasma}) is also defined as $F_{plasma} \approx 800$ mJ/cm^2.

Owing to the large band-gaps in KI (6.0 eV), CsI (6.1 eV) and NaCl (7.6 eV), photoexcitation with 400 nm wavelength light (3.1 eV) requires two-photon or three-photon processes. The time-dependent reflectivity changes for CsI, NaCl single crystals and polycrystalline KI film as a function of F are shown in Figs. 5.1(b-d). In KI (Fig. 5.1(d)), the fast drop in reflectivity in the sub-ps time scale at F of 60–180 mJ/cm^2 is very much akin to the observed optical changes in CsI and NaCl (Figs. 5.1(b-c)). At pump fluencies of ∼180 mJ/cm^2, a small bump appears at the end of the well in the green traces for KI (Fig. 5.1(d)) (the same in CsI at F = 140 mJ/cm^2 (Fig. 5.1(b)) and NaCl at F = 700 J/cm^2 (Fig. 5.1(c))). On the other hand, the fast enhancement in reflectivity observed at F = 240 mJ/cm^2 (Fig. 5.1(d)) followed by an decrease in the signal in the 50–100 ps time scale (blue trace in Fig. 5.1(d)) resemble those changes observed for Si at F > 200 mJ/cm^2 (Fig. 5.1(a)), CsI at F = 280 mJ/cm^2 (Fig. 5.1(b)) and NaCl at F = 1.1 J/cm^2 (Fig. 5.1(c)). Based on the fact that reflectivity of ionic and glass materials increase as they melt [162], this provides strong evidence for the melting occurring at the crystal's surface. Therefore we can use the fluence values of 140, 700, and 180 mJ/cm^2 from the green curves in Fig. 5.1 as an upper limit estimate for the melting thresholds for CsI, NaCl and KI samples respectively. The latter observation correlates with the observed ion detection threshold F_{th} = 250 mJ/cm^2 on CsI and F_{th} = 1 J/cm^2 on NaCl (Figs. 5.4(b-c)). The signal dependence of the ion detection measurements in CsI, which is similar to the case of Si, has another threshold at F ∼ 1 J/cm^2 corresponding to the plasma formation. However, these two thresholds for NaCl are very close to each other with F ≈ 1–2 J/cm^2, suggesting the melting and plasma formation in NaCl occurs at a similar incident laser fluence. The optical reflectivity and ion detection experiments were performed in air and in vacuum, respectively. The main difference between the results in vacuum and air is the plasma breakdown threshold, which we can see slightly lower threshold in air; however, it cannot influence the dynamics of the materials in the F range of <1 J/cm^2, where the main discussion was done in this experiment.

5.2.3. Surface crater observation

To reveal the strength of this ablation mechanism, we measured the crater with the interferometer and profiler after single-shot ablation. Limited by the measurable depth

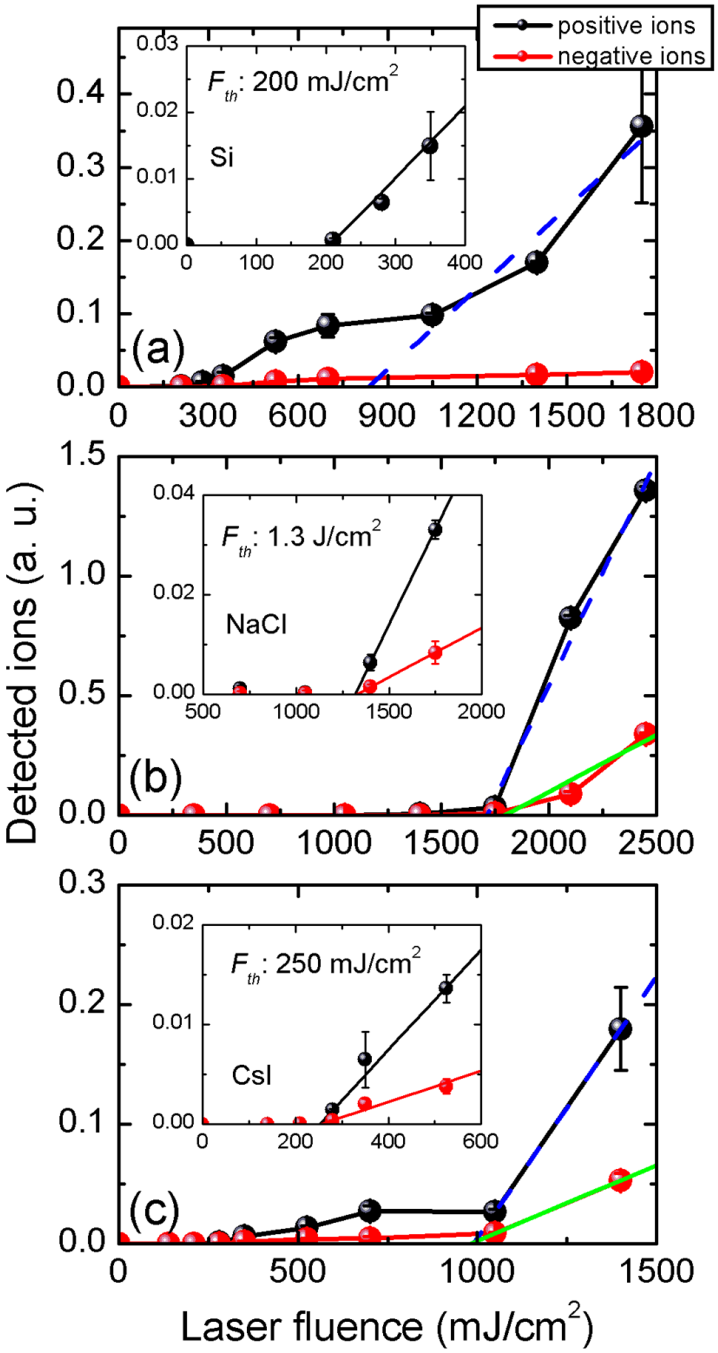

Figure 5.4: Yield for the detection of positive (black trace) and negative (red trace) ions in ion detection measurements for (a) Si, (b) NaCl and (c) CsI samples. Insets: magnified views near the threshold for each sample.

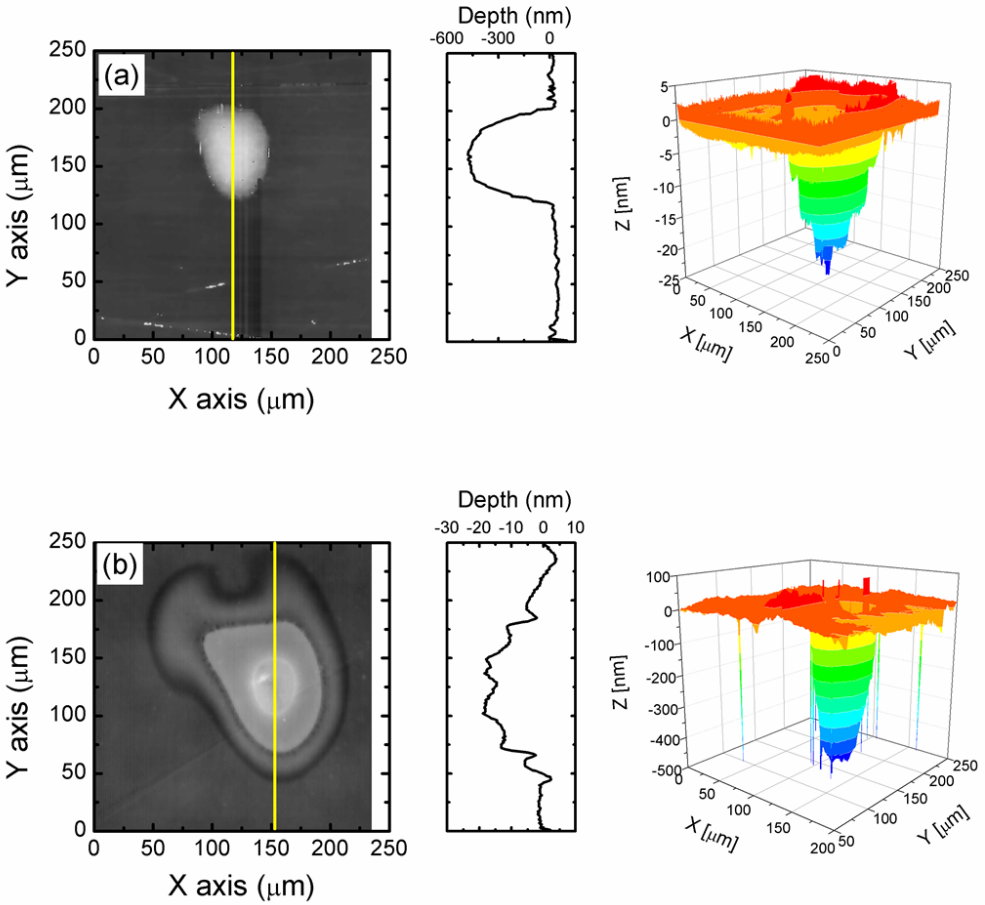

Figure 5.5: Interferometer images: the 3-dimentional crater images on the CsI (a) and Si (b) samples induced by the 400 nm photons. The incident laser fluence on CsI and Si are 140 mJ/cm^2 and 350 mJ/cm^2, respectively.

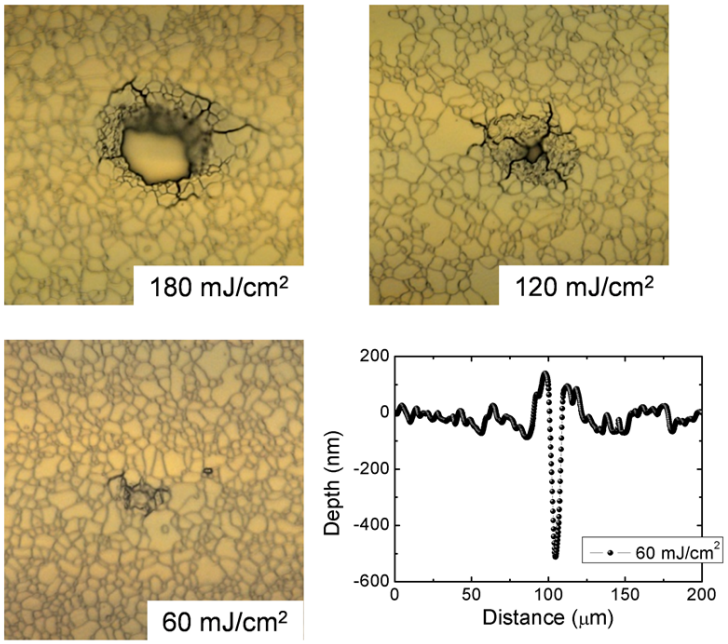

Figure 5.6: Micrographs of the craters produced by single pump pulse on KI film ($F \approx 60$–180 mJ/cm^2) measured by contact stylus profiler.

and resolution of our devices, CsI and Si were measured with interferometer, while NaCl and KI were measured with profiler. Figure 5.5 shows the typical crater's profiles observed via optical interferometry (Zygo) after exposing CsI and Si samples to single excitation pulses, with F = 140 and 350 mJ/cm^2, respectively. The crater's profiles of KI (Fig. 5.6) and NaCl were measured with stylus contact profiler and confocal laser microscope, respectively. Since KI samples are soft deposited films, therefore, the crater depth is relatively deeper compared to the bulk single crystalline materials (CsI and NaCl) with the similar incident laser fluence. Nevertheless, all the alkali halides were created a micron depth craters on the surface by a single fs laser pulse irradiation [130]. To compare, making a similar size crater in Al_2O_3 with a single laser shot requires F = 11.3 J/cm^2 for 295 nm light [163]. The crater depth at the each laser fluence is summarized in Table 5.1. With this we can further estimate the temperature change and excitation of electrons in the ablated materials, which will be discussed later.

5.2.4. Estimation of the fraction of excited halide centers

As mentioned in the introduction, laser ablation in alkali halides has previously been assumed to be caused by multi-photon ionization and consequent ablation by Coulomb explosion. However, our combined studies provide strong evidence for a qualitatively different ablation process that occurs well below F_{th} and F_{melt}. A calculation of the proportion of excited electrons would help to estimate the strength of this ablation

F (mJ/cm)	Depth (Si) (nm)
350	26
210	16
70	9
	Depth (CsI) (nm)
280	704
140	472
105	418
	Depth (NaCl) (nm)
420	970
350	950
	Depth (KI) (nm)
180	> 2500
120	1400
60	500

Table 5.1: Crater depth in Si, CsI, NaCl and KI samples at the different incident laser fluences measured by interferometry and/or laser microscopy.

mechanism.

The effective absorption (A_{eff}) through the crystals was corrected by subtracting a baseline level, which was measured in the limit of low incident laser power. The baseline level contains the absorption in the bulk and scattering from the surface. This correction accounts for the losses due to dispersive effects.

Figure 5.7 shows the dependence of the absorption as a function of fluence in NaCl, CsI bulk crystals and carbon coated KI/SiN film, which is used for the electron diffraction measurements. In Fig. 5.7(a), there is a clear threshold at F = 35 mJ/cm^2. And the signal of A_{eff} is almost saturated at F > 140 mJ/cm^2 with a plateau around $A_{eff} \approx 16\%$. Figure 5.7(b) shows the similar trend as Fig. 5.7(a). The hyper linear region in CsI was far below 35 mJ/cm^2. In the saturation region (>35 mJ/cm^2), the value of the absorption in the surface of CsI was around 34%. The absorption in KI is about ∼1.7% (within the noise level) at the intensity of 30–150 mJ/cm^2 (Fig. 5.7(c)). The plasma threshold of the carbon is about 180 mJ/cm^2; therefore, the incident laser was absorbed in the carbon film or the surface of the carbon at the laser fluence of >200 mJ/cm^2.

With the upper limit estimation of the proportion of excited ion-pairs are performed with the following assumption: the photo-excited depth corresponding to the crater depth and the cross section (S_{corss}) of the 2-photon and 3-photon processes are 50% and 33.3%, respectively. The effective absorption in each material was discussed above. The excited volume (V) contains $\frac{V \cdot \rho}{m} N_A$ ion pairs, where ρ, m, and N_A are density, formula weight and Avogadro number, respectively. The photon number absorbed in the excited volume can be calculated as $A_{eff} \cdot \frac{F}{E_{photon}} \cdot S_{corss}$, where E_{photon} is the single photon energy. The upper limit of the excited ion pairs can be estimated as 2% (NaCl at F = 350–420 mJ/cm^2), 7–8% (CsI at F = 105–140 mJ/cm^2), and 4% (KI at F = 140 mJ/cm^2), respectively. In the case of Si, it is single photon process. Around 9.5% of

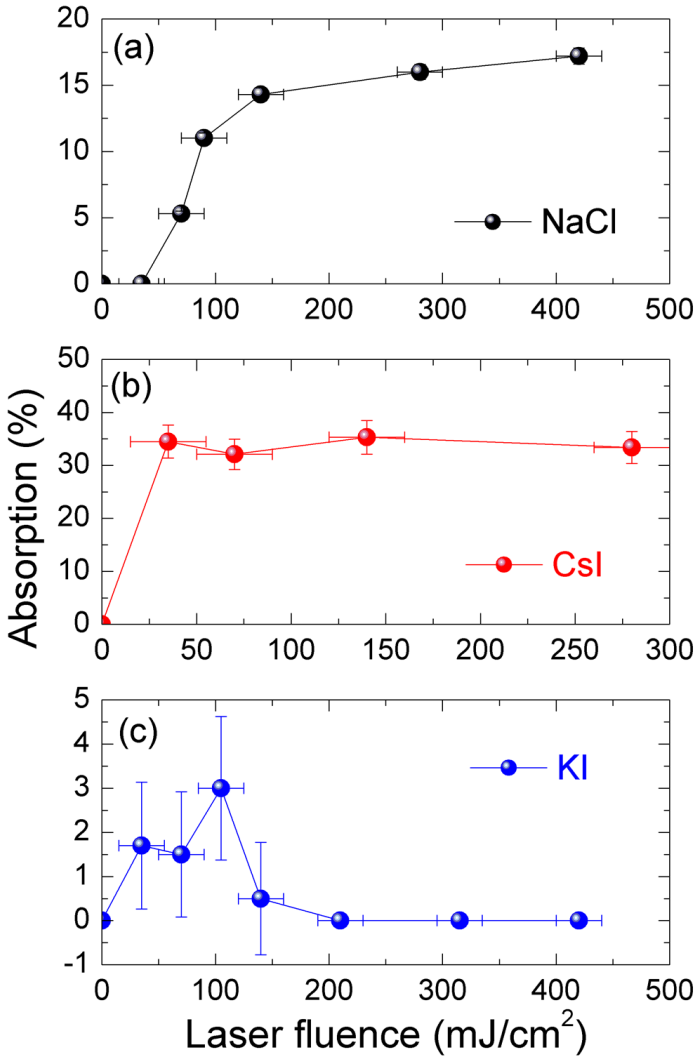

Figure 5.7: Fraction of absorbed pump energy as a function of F in NaCl bulk crystal (a), CsI bulk crystal (b), and KI thin film (c) corrected for diffuse scatter dispersive background.

the valence band electrons (38% of the Si atoms at F = 105 mJ/cm^2) are excited and coincide with previously reported nonthermal melting measurement.

An upperbound estimate of the increase in lattice temperature following photoexcitation can be provided by:

$$\Delta T_l = \frac{A_{eff} \cdot F}{\rho \cdot C \cdot d_c}. \tag{5.1}$$

where d_c the film thickness and and C is the specific heat capacity. For KI (ρ_{KI}: 3.13 g/cm^2; C_{KI}: 313 J/kg·K), this gives a value of T_l (F = 140 mJ/cm^2) = ∼800 K, which is well below its melting point (954 K). This assumption for the lattice temperature is also in good agreement for the laser fluence for the melting threshold, T_l (F_{melt} = 180 mJ/cm^2) = ∼1000 K. Similar calculations can be done with NaCl (ρ_{NaCl}: 2.165 g/cm^2; C_{NaCl}: 854 J/kg·K) and CsI (ρ_{CsI}: 4.51 g/cm^2; C_{CsI}: 201 J/kg·K), which have a value of T_l (F = 105 mJ/cm^2) = 450 K for CsI and T_l (F = 350 mJ/cm^2) = 300 K for NaCl. They are well below the melting temperature (CsI: 894 K; NaCl: 1074 K). This estimation indicates that the ablation process in alkali halides is indeed electronic dominated ablation, i.e. a cold laser ablation process that proceeds through the ejection of bulk material at very low effective excitation levels [143] (<4% excited halide centres (∼10^{20} cm^{-3})).

5.2.5. Time-resolved electron diffraction measurements

With the above mentioned measurement, we have revealed a cold ablation that has occurred at very low excitation level and well below the plasma generation. To further elaborate on the nonthermal mechanism of this ablation process in atomic level we performed single-shot FED experiments to gain direct structural information on the evolution of crystalline order following fs UV-photoexcitation.

Preparation and characterization of thin KI samples

To enable FED experiments in transmission mode, we have developed a protocol for the preparation of sub-100 nm thick <100> direction oriented KI films. It is hard to get thin crystalline alkali halide samples as they absorb water quite easily. The crystallinity can be easily damaged by humid in air. Potassium iodide is less hygroscopic than sodium chloride that makes it easier to work with. First of all free standing silicon nitride window (30 nm thickness) was prepared (Fig. 5.8). The pattern was made by ion milling machine with a mask to remove the SiN layer. The 300-nm silicon was removed by KOH etching. In order to completely remove water, the plate was baked at 300°C for one hour. Afterwards the polycrystalline KI samples (∼50 and 100 nm thickness) were thermally deposited on top of the substrate. The deposition rate and film thickness were monitored in-situ with a quartz oscillator. The KI layer was covered with a very thin carbon layer (<5 nm) to avoid damage from moisture. At the last step, the sample plate was annealed at a temperature of 500 K for half an hour to improve the crystallinity of the material.

The crystallinity of the KI sample was characterized with static X-ray diffraction (XRD) and electron diffraction. Figure 5.9 (a) shows the XRD spectrum from KI

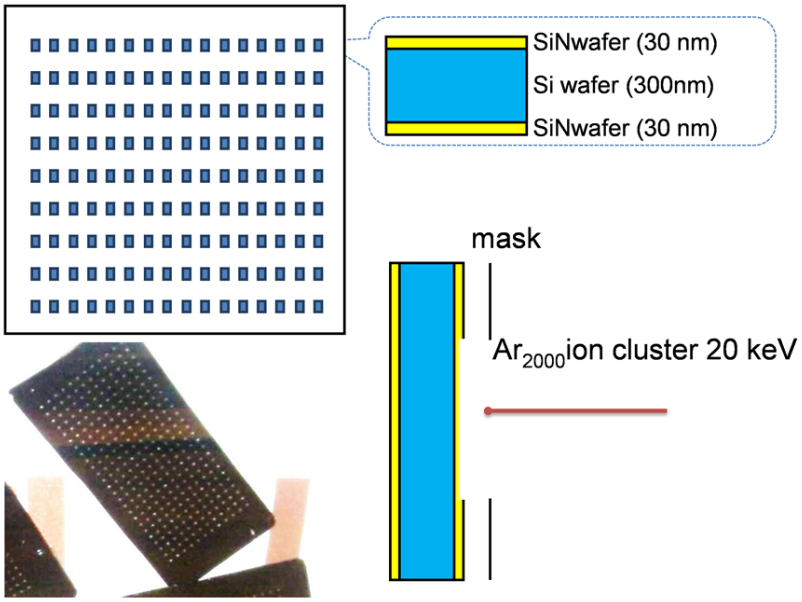

Figure 5.8: Substrate preparation for KI samples.

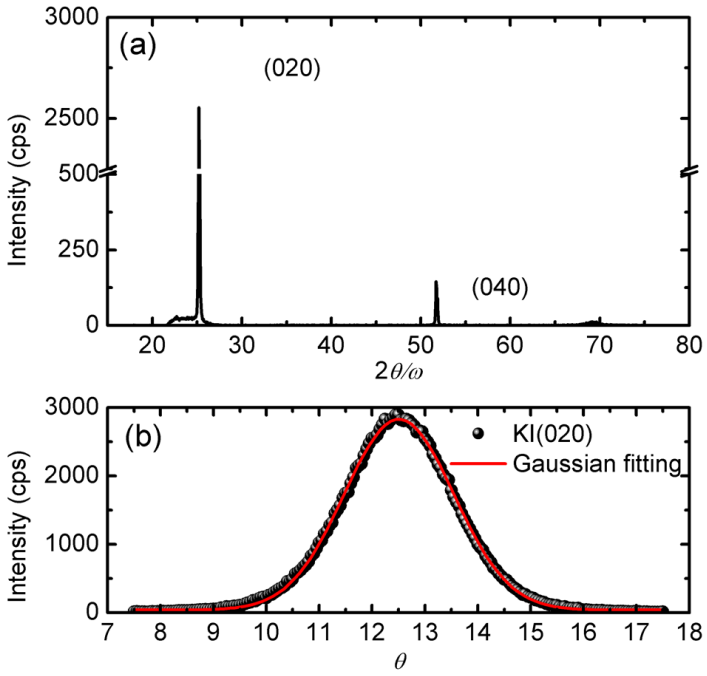

Figure 5.9: The XRD spectrum from KI samples (a) and the rocking curve spectrum of the diffraction line from KI (020) plane (b).

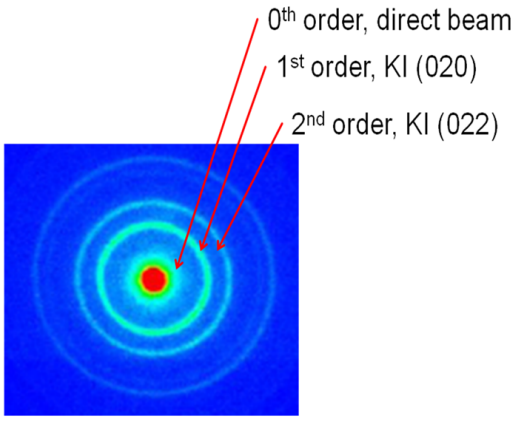

Figure 5.10: Typical electron diffraction pattern from KI samples. This images was average of 10-shot-accumulation of electron bunches (10 shots in 1 image).

sample. The diffraction lines from KI (020) and (040) lattice planes are observed, which suggests that the KI is longitudinally oriented in the <100> direction. The rocking curve measurement (Fig. 5.9(b)) also supports that the KI has some orientation preference in the <100> direction. The electron diffraction image (Fig. 5.10) does not exhibit any isotropy, therefore does not contain any preferential orientation transverse to the electron beam propagation.

For the optical pump-probe reflectivity measurement, the KI thin film (2.5 μm thickness) was prepared in the same way by thermal deposition. 2 mm thick fused silica glass was used as the substrate in this case.

CsI and NaCl are also tried, however, they do not show very good crystallinity. Figure 5.11 shows the XRD and rocking curve of CsI as a comparison, which has a large bump distribution in a wide range (2θ) instead of high intensity narrow peaks.

Experimental setup

The time-resolved electron diffraction measurements were performed with the compact FED system (Egun300). The setup of the time-resolved electron diffraction measurements has been shown in Chapter 3 (Fig. 3.5). The laser beam from the commercial Ti:sapphire laser system was split into two (the pump and probe arms) by a beamsplitter. The optical pulse for the pump arm was converted to 400 nm wavelength through second harmonic generation and focused on the KI samples with a spot size of 450 μm. The optical pulse for the probe arm was converted to 266 nm wavelength through the third harmonic generation and focused onto the gold photocathode generating the electron pulse. The optical path difference between the probe and pump arms can be fine-tuned through the motion of a delay stage. As the single-shot experiment requires very high charge, we proceeded a few procedures to increase the charge and stability

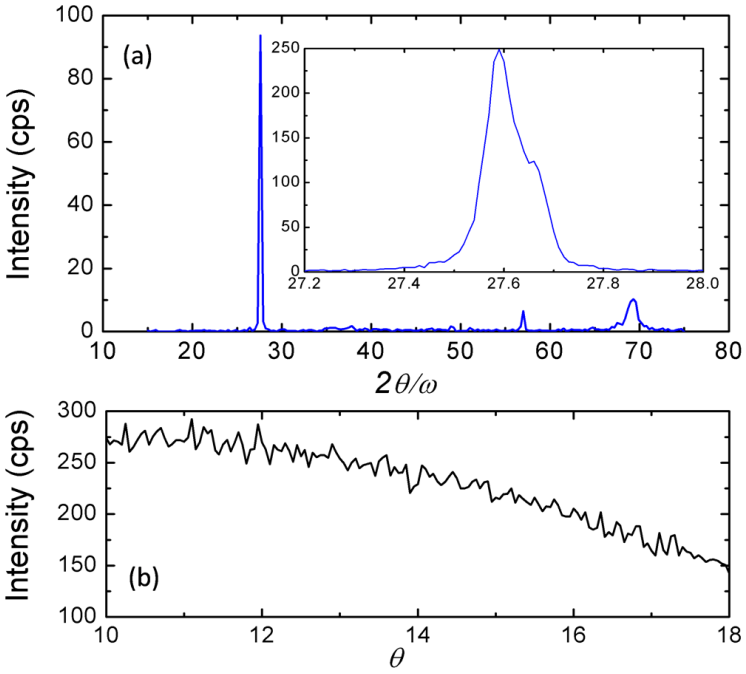

Figure 5.11: The XRD spectrum from CsI samples (a) and the rocking curve spectrum of the diffraction line from CsI (020) plane (b).

of the system. First we increased the cathode to anode distance to around 3 cm and tuned the UV-excitation laser fluence until the generated electrons saturated. Second the electron pulses were accelerated to 90 keV instead of 150 keV with electrostatic field gradient between the photocathode and anode plate to maintain higher stability. Third the pump laser was carefully aligned not to scatter onto the photocathode. At the sample position, we can get a $\sim$1 ps pulses containing $\sim 10^5$ electrons confined to a 120 μm in diameter area. The electron pulse diffracted by the sample was focused with the magnetic lens at the phosphor screen fiber-coupled with charge coupled device (CCD) camera. Samples were moved between excitation pulses so that each pump pulse would hit a fresh spot.

FED measurement

Figure 5.12 shows normalized radially averaged intensity profiles obtained from the single-shot electron diffraction patterns at different time delays (t_d = -250 ps, +30 ps and +1.8 ns) with respect to the optical excitation pulse. The incident laser fluence was 140 mJ/cm^2, which is below the threshold for melting and plasma formation.

The time-dependent diffraction intensities for the (000), (020) and (022)-Bragg reflections are shown in Fig. 5.13. The intensity of the direct transmitted electron beam decreases at $\sim$10 ps (Fig. 5.13 (a)), which has previously been observed in strong excitation [8, 29]. It was attributed to the large atomic motion in the excited material. The intensity of the direct beam gradually increases on the nanosecond time scale as the material is gradually removing from the surface. In the millisecond time scale, the

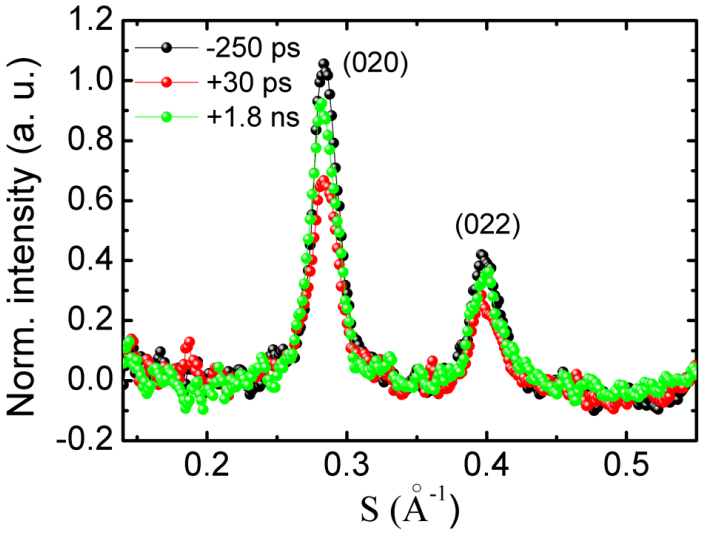

Figure 5.12: (a) The profiles of the single-shot time-resolved electron diffraction patterns from 50 nm KI (F $\approx$ 140 mJ/cm^2) at the time delay of -250 ps, +30 ps and +1.8 ns. The inset is the electron diffraction pattern from the KI thin film.

sample was completely removed and the transmitted electron intensity is increased by a factor of 6. This also reinforces the argument that the ablation process in alkali halide is not invoked by the plasma process because the plasma effect disappears on the $\sim$100 ps time scale.

The change of diffraction pattern on higher orders can further give us more detail atomic motions in the lattice. The time dependent 1^{st} and 2^{nd} order electron diffraction intensities from 50-nm thick KI sample is shown in Fig. 5.13(b). There is a clear decrease in the crystalline order at about 10 ps, which gradually recovers in the nanosecond time scale. According to the dynamic equation we can calculate the temperature in regard to the change of diffraction intensity. The intensity of the electron diffraction (I) can be expressed by the following equations:

$$\begin{aligned} I &= \left|F(\vec{K})\right|^2, \\ F(\vec{K}) &= G(\vec{K}) \sum_{j=1}^{M} f_j(\vec{K}) D_j(\vec{K}) \exp(2\pi \vec{K} \cdot \left\langle \vec{r}_j \right\rangle). \end{aligned} \tag{5.2}$$

where $\vec{K}$ is scattering vector, F($\vec{K}$) is structure factor, G($\vec{K}$) is Laue function, $f_j(\vec{K})$ is atomic scattering factor, D$_j$ ($\vec{K}$) is the Debye-Waller factor and $\left\langle \vec{r}_j \right\rangle$ is average position of the j-th atom in the unit cell. Debye-Waller analysis is based on the concept of random, homogeneous variations of bond distances throughout the crystal. The Debye-Waller factor can be simplified with the mean square displacement (U$_j$) or B-factor (B$_j$) as:

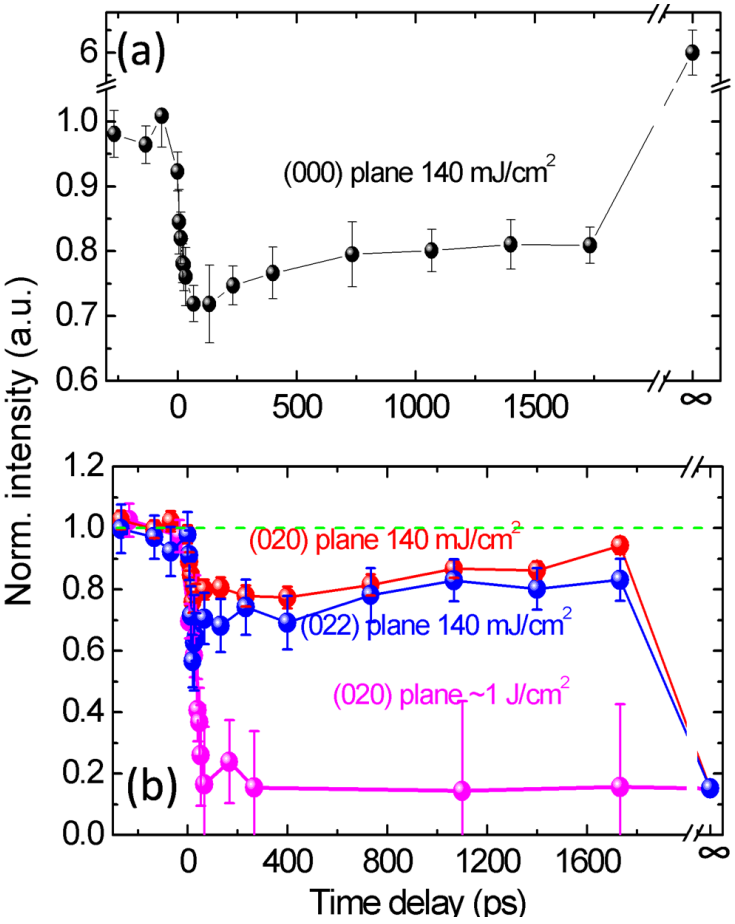

Figure 5.13: Time-dependent electron diffraction intensity changes from 50-nm thick KI (000), (020) and (022) Bragg reflections at F $\approx$ 140 mJ/cm^2 and that from KI (020) at F $\approx$ 1 J/cm^2.

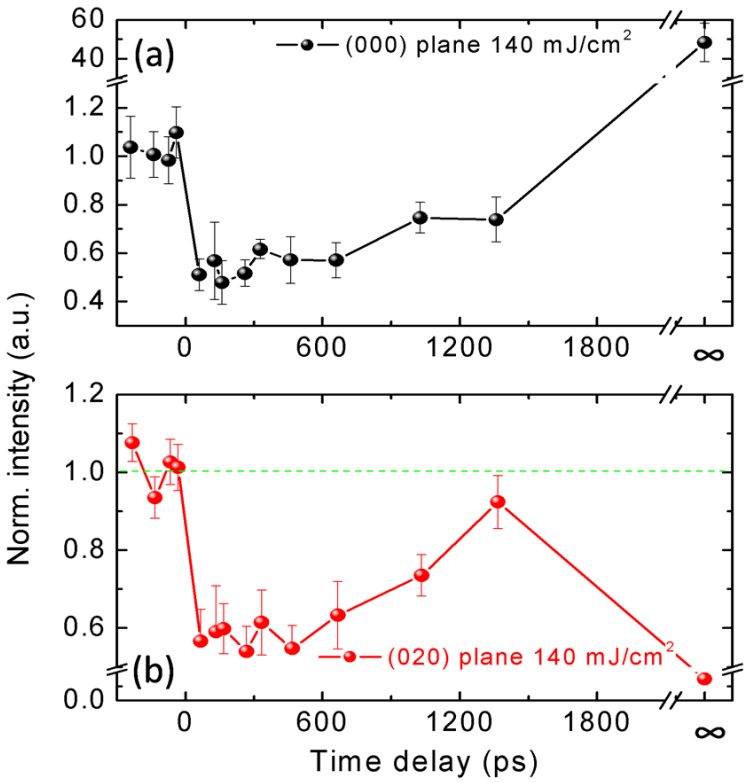

Figure 5.14: (a) Normalized time dependent intensity of transmitted electron beam for 100-nm thick KI sample (0^{th} order electron beam), and (b) normalized time dependent intensity of the diffraction ring from KI (020) plane for 100 nm thick KI samples at F $\approx$ 140 mJ/cm^2.

$$D_j(\vec{K}) = \exp(-K^2 B_j) = \exp(-8\pi^2 K^2 U_j) = \exp[-\frac{-8\pi^2 U_j \sin^2\theta}{\lambda^2}]. \quad (5.3)$$

where θ is the scattering angle and λ is the de Broglie wavelength of the electrons. Based on the simplified Debye-Waller model and the B-factor by H.X. Gao [164] derived from experimental phonon density of states data, the temperature change of the lattice can be calculated, which is ∼1200 K (kinematic theory) and ∼1800 K (modification with dynamic theory [165]) for a 75% change of 1^{st} order and 55% change of the 2^{nd} order scattering vector change. Therefore, the drops in intensities cannot be accounted for by thermal heating alone, since the simple Debye-Waller model predicts an increase in lattice temperature, which is well beyond the melting temperature of KI (954 K) and in conflict with the previously estimated ∼800 K value accounting for the deposited amount of the pump energy into KI sample. In addition, since there is no indication for the formation of liquid KI, the actual lattice temperature after electron-phonon equilibration should be below the melting temperature of KI. The above discrepancy is easily understood by acknowledging the limitations of the Debye-Waller model, which is only applicable for the temperature range where the unit cell structure of the crystalline material remains intact. Another possible mechanism is the formation of point defects, however, it requires around 30% ($\approx 3\times10^{21}$ cm^{-3}) point defects to decrease the (020) diffraction intensity by 25%, which means the lattice-defect-accumulation cannot make this huge modulation in the intensity of the electron diffraction rings [166]. Melting is one possibility that can causes the loss of crystallinity. When the incidence laser fluence is in close proximity to that of the melting threshold there is probability that a fraction of the sample becomes either highly-disordered or turns into a liquid. Most likely, in addition to the sample heating, both defect formation and melting are responsible for the reduction in diffraction signal. As the temperature of the sample starts equilibrating within the photoexcited volume, these partially highly-disordered regions tempt to recrystallize. Therefore, the slow recovery in the diffraction intensity is observed in a nanosecond time interval, after which the Deby-Waller analysis is in a good agreement (T_l = 725 K) with the average temperature estimate. These results suggest that the observed diffracted intensity changes are dominated by electronic stress that modulates the structure factor amplitude, which is a maximum for the unperturbed cubic lattice [81, 167–170]. The electronic stress is the initial distortion, which is directly introduced by the photoexcitation. This effect often modulates into the thermal stress or dephased on the sub-nanosecond time scale [118]. Figure 5.13 shows the time-dependent intensity of electron diffraction ring from (020) at fluence of ∼1 J/cm^2, which is high enough to generate plasma on the surface of KI samples. The diffraction ring completely disappears within 100 ps time scale due to the plasma formation. Also shown in Fig. 5.14, to exclude the effect of multiple scattering the same measurements were also performed with 100-nm thick KI sample, which show similar trend as that in the 50-nm thick sample. It was also performed at the same laser excitation condition (F = 140 mJ/cm^2). A temperature of ∼1900 K is predicted by the Debye-Waller model, which is even higher than the boiling temperature of KI (1600 K).

Figure 5.15(a) shows the temporal evolution of the (020)-Bragg reflection in KI (black

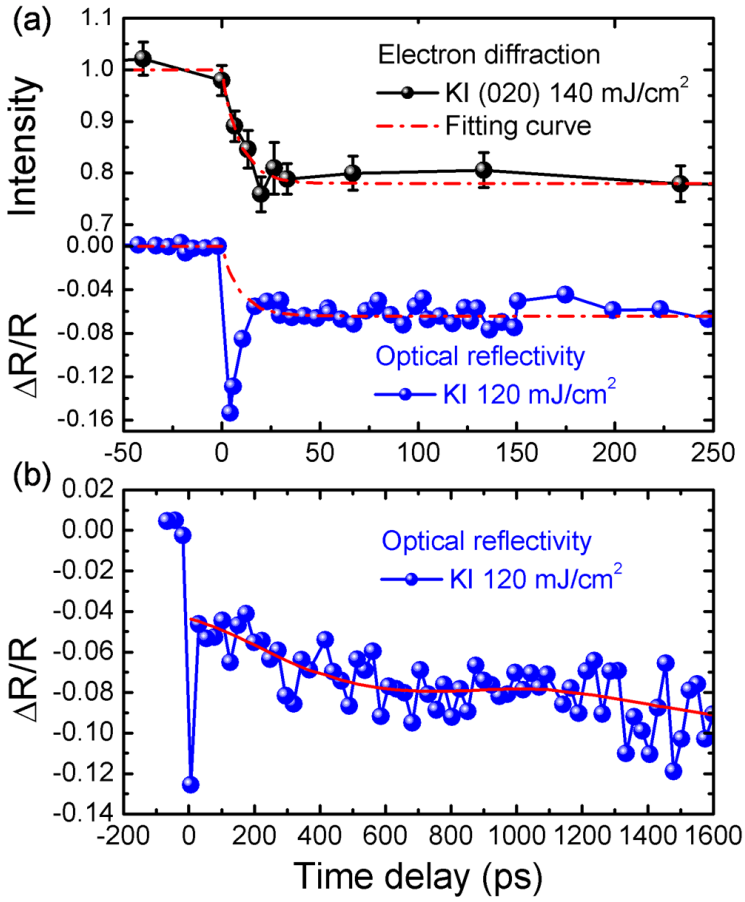

Figure 5.15: (a) Comparison between the time-dependent electron diffraction intensity changes of KI (black symbols), and time-dependent reflectivity changes of KI ($F \approx 120$ mJ/cm^2, blue symbols). The red dashed lines are fits to the electron diffraction changes using an exponential decay function ($\sim$10 ps). (b) The time-dependent optical reflectivity in nanosecond range. The solid red line is a guide to the eye. The oscillation (frequency (f) of $\sim$1 GHz) corresponds to the longitudinal motion ($f = v/2d$, where v ($\sim$2000 m/s) is the speed of sound and d ($\sim$1000 nm) is the length scale of the object [118]).

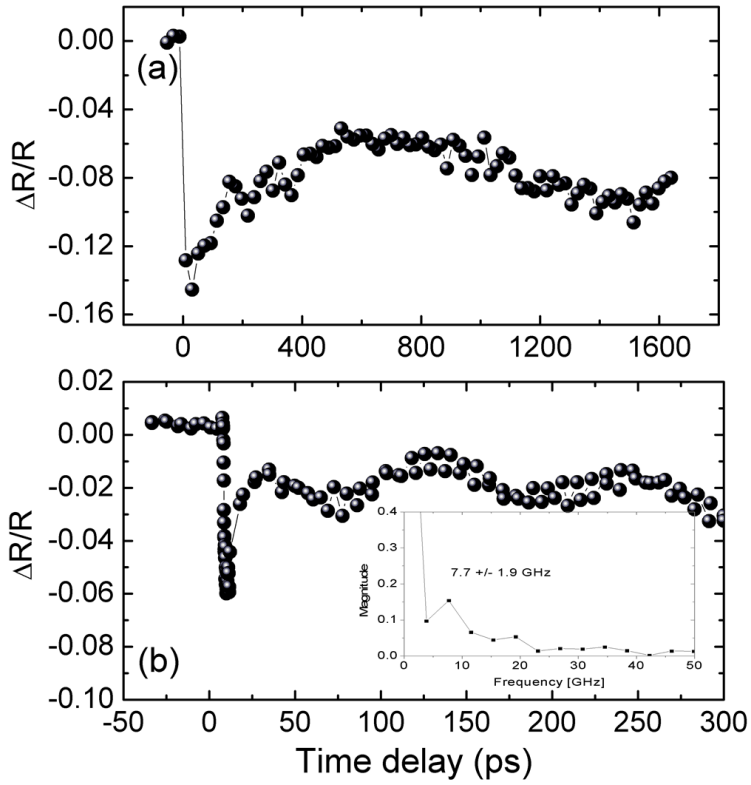

Figure 5.16: Time-resolved reflectivity changes in NaCl (F = 350 mJ/cm^2) and CsI (F = 70 mJ/cm^2). A frequency of 0.6 GHz (NaCl) (a) and 7.7 GHz (CsI) (b) is indicative of an acoustic (strain) wave likely triggered by electronic stress.

symbols) and the observed optical reflectivity changes, with improved signal-to-noise ratio, for KI (blue symbols) under similar photoexcitation conditions. As indicated in Fig. 5.15, the time-dependent reflectivity changes in KI can be separated into three temporal domains as a function of t_d. A fast initial drop for $t_d < 1$ ps, a subsequent increase in the signal at $t_d \approx 10$ ps, and an oscillatory behavior for $t_d > 100$ ps. The observed optical changes in $t_d < 20$ ps can be explained as the creation of excitons [136] that introduce electronic stress, which is partially released through the generation of strain waves in the GHz range. Similar and clearer oscillation in GHz range on CsI and NaCl are also shown in Fig. 5.16. CsI has shallower crater in the range of 100 nm that has a frequency of 7.7 GHz, while NaCl needs 2–3 photon absorption and the crater is much deeper which makes the oscillation period much longer (~1.5 ns periods). The generation of stress is also evidenced by the decrease of intensity of the (020)-Bragg reflection (black symbols in Fig. 5.15) that develops on the same time scale (shown as red dashed traces, which were obtained by exponential fits to the data).

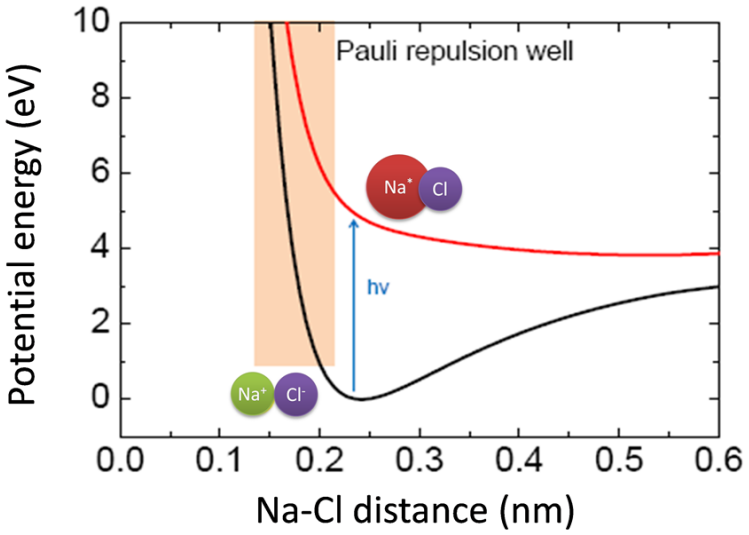

Figure 5.17: The calculated potential surface energy of NaCl molecules. The black line indicates the ground state ($1\ ^1\Sigma^+ : Na^+Cl^-$) and the red line indicates the neutral excited state ($2^1\Sigma^+ : Na^*Cl$). The wavepacket at the local minimum of the ground state would be directly photoexcited to the onset of the Pauli repulsion well.

As calculated before, the large structural changes observed in KI were induced by the excitation of a very small fraction of halide centres, on the order of <4% (estimated from in-situ single-shot optical measurements). This result, with the fact that >30% point defects are required to modulate the intensity in the electron diffraction rings, indicates that the lattice-disorder and ablation processes in the alkali halides with the intermediate photoexcitation (~100 mJ/cm^2) should not be evoked by the

accumulation of lattice defects. In addition, the calculated lattice temperature after electron-phonon equilibration (from Eq. 5.1) was found to be below the melting point of KI. This is in agreement with the FED observations, which confirmed that the sample did not enter a liquid state. It is also interesting to note that Coulomb explosion induced by the plasma formation cannot be applied in this intermediate photoexcitation range. Therefore, we propose the repulsive nature of STEs to explain the lattice-disorder and ablation process with the intermediate-range photoexcitation. When isolated alkali halide molecules (contact ion pairs) are excited by a UV-photon, an electron in a p-orbital of the halogen centre is transferred to the outer s-shell of the alkali metal ion. This charge transfer process causes a sudden increase in the size of the metal centre and switches off the Coulomb attraction between the ions, thereby driving the system into a highly repulsive state that lies at the onset of the Pauli repulsion well [171, 172]. The same repulsive force, which is also referred to Pauli, core-core or Born repulsion force, is usually observed in the ground state of multi-electron atomic systems under a high pressure [173]. This effect in the excited state is depicted in Fig. 5.17, in which the calculated potential energy surfaces for the ground and excited states of the NaCl molecule are shown. The fs laser pulses generate the STEs in alkali halide crystal, where the electrons or holes can be delocalized in the lattice. Once the delocalized electron is localized in the cation site, vice versa, the hole is localized in the anion site, this contact ion pair in the lattice trapping an exciton may have the similar behavior as an isolated molecular promoting the formation of highly repulsive state. These highly repulsive isolated molecules in the lattice may induce the electronic stress driving the large lattice disorder in the crystal, which will lead the subsequent ablation.

5.3. Conclusion

To summarize, we had performed FED and fs-optical reflectivity studies to provide direct information on the structural and electronic evolution of alkali halide crystals (NaCl, CsI and KI) exposed to UV-fs-photoexcitation, i.e. above the threshold for single-shot nonreversible sample damage. Our time-resolved results in combination with ion detection measurements indicate a cold laser ablation process that occurs at excitation levels well below the threshold for plasma formation and even that required to thermally melt the alkali halide crystals.

We found evidence for a cold laser ablation process that takes place in alkali halides upon UV-photoexcitation of an extremely small fraction of halide centres. The observed dynamics might illustrate the very nature of a purely quantum phenomenon, i.e. the onset of Pauli exclusion forces affecting the structure and directing a collective macroscopic response, more than an order of magnitude greater force than previously observed mechanisms.

As a further investigation of the underlying questions, the alkali halide ablation indicates large fragment generation. It would be interesting to observe this with a direct detection. Optical and FED shadowgraphs will be very helpful for a detail analysis of the ejected materials.

The Pauli exclusion force implies the strong electron-hole excitation and different color center formation. A more sophisticated spectroscopic measurement and theoretical model would be necessary for elaborating the dynamic process and detailed mechanism during different color center generation.

6. Characterization of electron time zero and pulse duration in REGAE

Ultrafast electron diffraction has made significant progress towards resolving structural changes at the atomic level. The development of new time-resolved electron sources have been discussed in Chapter 3. REGAE has been designed for unprecedented time resolution down to 20 fs (FWHM) and potentially revealing the fastest dynamic changes like photonic breathing modes occurring in silicon and more complex molecular systems such as proteins and DNA. For FED experiments the spatial overlap of pump laser and probe electrons can be found by a LYSO scintillator (see Chapter 3). However, the temporal overlap is much more difficult. It requires the exact coincidence of the pump and probe pulses to be determined with femtosecond precision independent of any changes of the observed diffraction patterns. Measuring the electron pulse duration and time zero (t = 0) are the two main challenges of FED.

This chapter describes the first FED experiment of REGAE, which is to find the time zero by a single-shot gold melting experiment. Further measurements of REGAE's bunch length with sub 100 fs resolution are proposed.

6.1. Time zero of REGAE

In order to prepare for a FED experiment, it is important to find the time zero precisely. Time zero is given by the perfect temporal overlap between the centroids of the pump (optical) and probe (electrons) pulses at the sample plane. The centroid of both pulses should arrive at the sample plane at the same time [174]. The maximum travel range of the optical delay line (see Fig. 3.15) is around 300 mm (∼2 ns considering the doubled optical path introduced by the retroreflector). First, we set the initial position of the delay line with nanosecond precision. The target camera in Fig. 6.1 has a gated intensifier which has a response time of 1 ns. By detecting both the electron bunch and laser on the LYSO scintillator we can find the rough timing within 1 to 2 ns, which equals to 300 mm to 600 mm optical path in free space.

But this method is not sufficient for femtosecond experiments. Single-shot time-resolved experiment on polycrystalline gold helps to find t = 0 with a resolution of a few picoseconds. We are able to follow the loss of long-range order that is present in the crystalline phase and the emergence of the liquid structure where only short-range atomic correlations are present. The transition completes within 5 ps. The change is dramatic and readily observed. It can visibly tell us whether the current position is before or after time zero.

Single-shot experiment requires a large amount of identical samples. 300 free standing SiN membrane windows are made by conventional anisotropic chemical etching

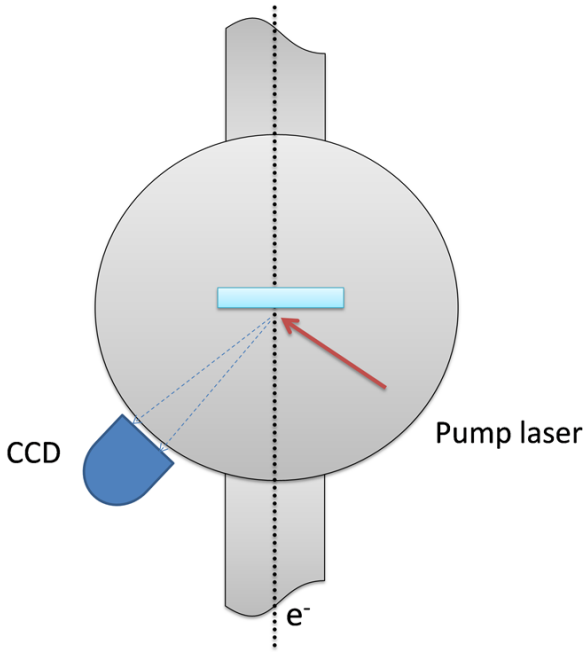

Figure 6.1: Schematic of the sample chamber configuration for nanosecond timing of REGAE's pump laser and probe electron beams.

methods. Each has 200 by 200 μm window with a very thin membrane (30-nm amorphous SiN). The polycrystalline gold samples (75 nm) were thermally deposited on SiN. In order to perform a single-shot experiment, we use a Pockels cell to isolate single laser pulse (pump laser runs at 1 kHz). In addition the detector is gated to 10 μs exposure time to enable single electron bunch detection. The excitation fluence is 150 mJ/cm^2 at 400 nm and 100 fs pulse duration. Under such an excitation level we should be able to melt the sample starting from room temperature. The probe is femtosecond 3.5 MeV electron pulses in diffraction mode. The experiment requires high time resolution and sufficient electron number density to provide single-shot structure determinations to record a full time sequence of events with limited samples (maximum 300).

Each time step was averaged only 3 times limited by the number of samples, however, Figure 6.2(a) shows a clear diffraction ring using electron bunches of 100 femtocoulomb (fc) charge per pulse. Within a time span of less than 5 ps the diffraction rings from (400) plane fade out and disappear completely, which comes from thermal excitation. However the change from lower orders (111), (200), (220), (311) and (222) planes is not very clear. It is mainly due to formation of liquid structure where only short range atomic correlations are present and their diffraction overylap with the diffraction from lower order planes. Meanwhile the intensity of the direct transmitted electron beam decreases at around 5 ps (Fig. 6.2(a)), a behavior which is always observed under strong excitation [8, 29]. It is related to the large atomic displacement in the excited material. On a millisecond time scale, the sample is completely removed and the transmitted electron intensity is increased by a factor of 5. This solid-to-liquid

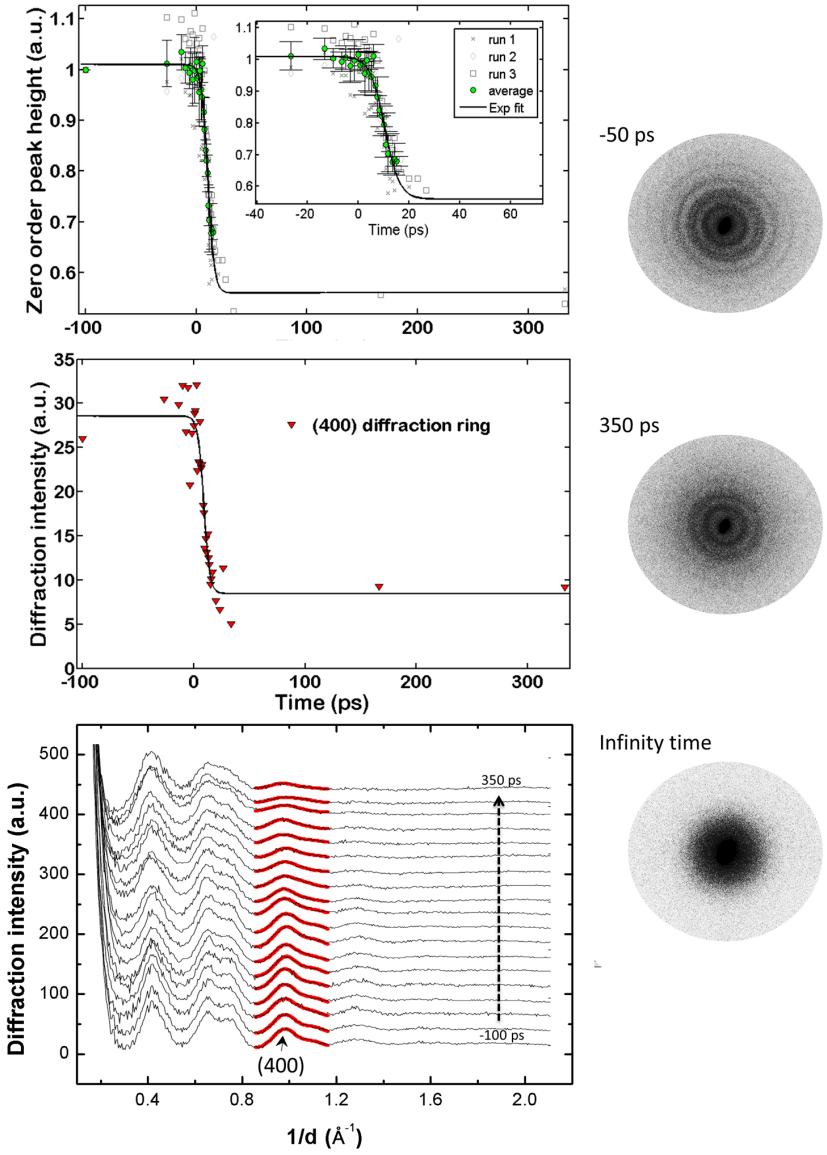

Figure 6.2: The first time-resolved electron diffraction experiment at REGAE, single-shot laser ablation of gold. (a) Normalized time dependent intensity of transmitted electron beam for 75 nm gold sample (0^{th} order electron beam), and (b) normalized time dependent intensity of the diffraction ring from gold (400) plane. (c) radially averaged intensity difference of diffraction images taken at selected time points. Peak amplitudes were normalized by the average amplitude at negative time points and the solid lines are exponential fit of the data.

phase transition tell us the relative time zero position within 0.8 mm (5 ps) range and shows a time resolution of the pump-probe system below 1 ps.

Further measurements should be done with higher resolution and reversible experiments which can be performed for daily use. For example, the laser induced plasma on a copper mesh can deform the electron beam in sub-ps time scale [175], which can reach around 1 ps time resolution. The plasma process is a consequence strong laser induced electron emission and surface charging effect that can distort the probe electron beam. Time zero can be determined from the intensity change of the electron beam.

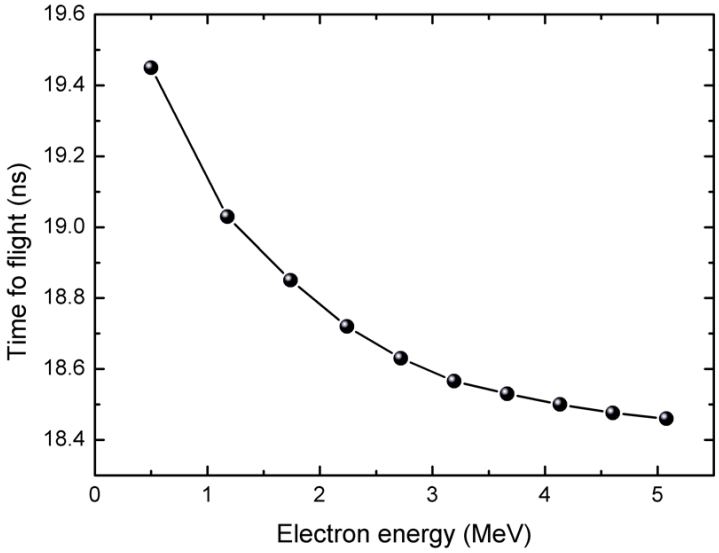

Figure 6.3: Correlation of electron energy to the time of flight at the sample position. ASTRA simulation based on REGAE, see Appendix A.

For different electron energies the corresponding time zero position is quite different due to their different electron velocities. Figure 6.3 shows that an energy change from 2 to 5 MeV leads to a time of flight difference of around 1 ns, which should be taken into account when building up the optical pump setup. The single-shot experiment described above is performed at 3 MeV (98.9353% the speed of light). If we operate the machine at 5 MeV (99.5692% the speed of light), the arrival time is 200 ps earlier than that at 3 MeV. It means the delay line mirror position should be extended by around 60 mm.

6.2. Precise bunch length and timing measurement for REGAE

The electron bunch length is one of the dominant contributions to the time resolution achievable in ultrafast electron diffraction. For RF guns the timing jitter between rf and

laser is another additional and crucial parameter that influences the time resolution. This is not an issue in a DC accelerated electron gun, since the electrons are driven by direct current and there is no requirement of synchronization between laser and RF. Simulations (see Chapter 3 Fig. 3.7) show that REGAE is able to generate electron bunches shorter than 50 fs. DESY LLRF has developed a solution to provide less than 20 fs timing jitter [176]. The capability to fully characterize the bunch length and jitter is particularly important to further improve the machine and time-resolved experiments.

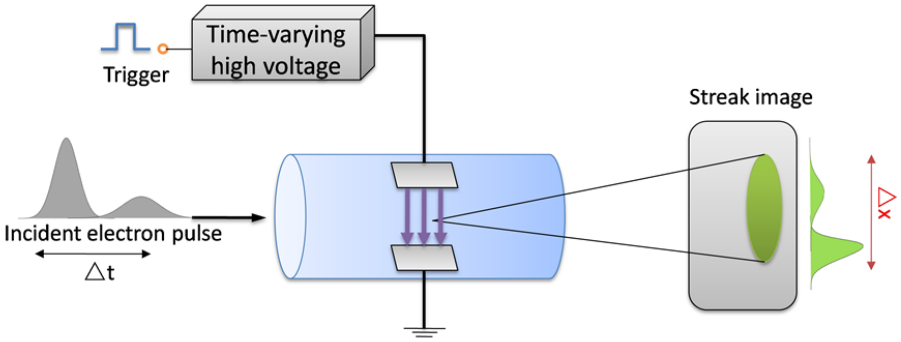

Figure 6.4: Principle of a streak camera.

The conventional method for measuring electron pulse duration is to use a streak camera (Fig. 6.4). A pair of deflection plates is positioned along the electron beam path. A voltage ramp is applied when the electrons pass through them. The according time dependent electric field transfers the electron temporal distribution into a transverse spatial one. Since the streak camera technique does not provide direct information for the time zero, it has to be inferred from plasma generation on a copper mesh placed at the sample position. The streak camera method was further improved by using a photoswitch (GaAs) to synchronize the ramping voltage with the electron beam [177], which provides much higher time resolution of a few hundred fs. Several other techniques have also been demonstrated. A RF cavity can be used to deflect electron beam from temporal distribution to spatial direction. This technique is closely related to the above mentioned streak camera method, and limited by the timing jitter from the RF system [178]. Another technique uses the coherent transition radiation emission when electrons pass an interface between two media of different dielectric constant [179]. However, this method requires prior knowledge of the temporal pulse shape and relies on a relatively large number of electrons that exceed the design parameter of REGAE.

REGAE, with its design for fs electron bunches, calls for an even shorter probe to measure the bunch length. A cross-correlation scheme by using the ponderomotive

force between laser and electrons has been developed by Hebeisen and co-workers in 2006 [22]. It was further improved by using grating enhanced ponderomotive scattering [23]. It provides the probability to measure both the bunch length and time zero with 40 fs time resolution, which is limited by the pulse duration of the laser. The ponderomotive force is an effective Lorentz force experienced by the charged particles in the presence of a slowly spatially varying electromagnetic field. When the light intensity $I \ll 10^{18}$ W/cm^2, the quiver motion of an electron is much slower than the speed of light and we can neglect the magnetic field. The force can be written as a function of the light intensity:

$$\vec{F}(r,t) = -\frac{e^2\lambda^2}{8\pi^2 m_e \varepsilon_0 c^3} \bigtriangledown I(r,t) \tag{6.1}$$

where e and m_e are the charge and mass of the electron, λ is the wavelength of the laser, ε_0 is the permittivity of free space. The scattered electrons are imaged on the detector to give direct visualization of the laser-electron interaction.

The schematic drawing for REGAE ponderomotive measurement is shown in Fig. 6.5. One laser beam with an energy of 2 mJ/pulse and duration of 60 fs is sent to a long delay line (D1) with travel range of 305 mm and split into two (a1 and a2) counterpropagating laser pulses that intersect with the electron beam path (e^-) in the sample chamber. One of the arm (a2) is sent through a small delay line (D2) with 25 mm travel range to permit balancing of the two arms and build up of the standing wave. The laser beams are focused into the chamber with two lenses (L1 and L2) of f = 300 mm (focal length). The two laser beams need to overlap in space as well as time with each other and with the electron pulse to produce the scattering signal. The spatial overlap of the two laser beams can be achieved by alignment on a LYSO scintillator screen inside the chamber and monitoring the interference pattern in position c1 (Fig. 6.5) for optimization. The temporal overlap can be found by using a 45° placed copper mesh (Fig. 6.5 (insert)) [175]. We can find the relative time with electrons for each laser arm within a picosecond range by using the plasma scheme. By maximizing the signal their spatial overlap with the electrons can be further optimized. After spatial and temporal adjustment, the sample holder can be moved up to the pinhole position (Fig. 6.5(insert)), which has a 30 μm pinhole. It helps to clean up the beam to generate a sharp edge on the detector and improve the scattering signal. The laser beams and electrons interact after the pinhole and hence the electrons can be scattered by the ponderomotive force. Fine tuning of small delay line (D2) and maximizing the ponderomotive signal should be done by mapping the position of both small and long delay line and analyzing the scattering signal. After optimization, a cross-correlation scan of the laser-electron would give us the time zero and electron pulse duration independent of any material constants.

In order to get a preliminary idea of the scattering process we modeled the ponderomotive scattering with ASTRA by using the namelist LASER, which includes a laser generated electromagnetic field [32] (see Appendix A for detail parameters). The laser field is calculated when the electron bunch is in a specified interaction region. A synchronized timing is given in the simulation to adjust the time of flight difference due to the velocity difference between the laser and electrons. The Gaussian laser beam

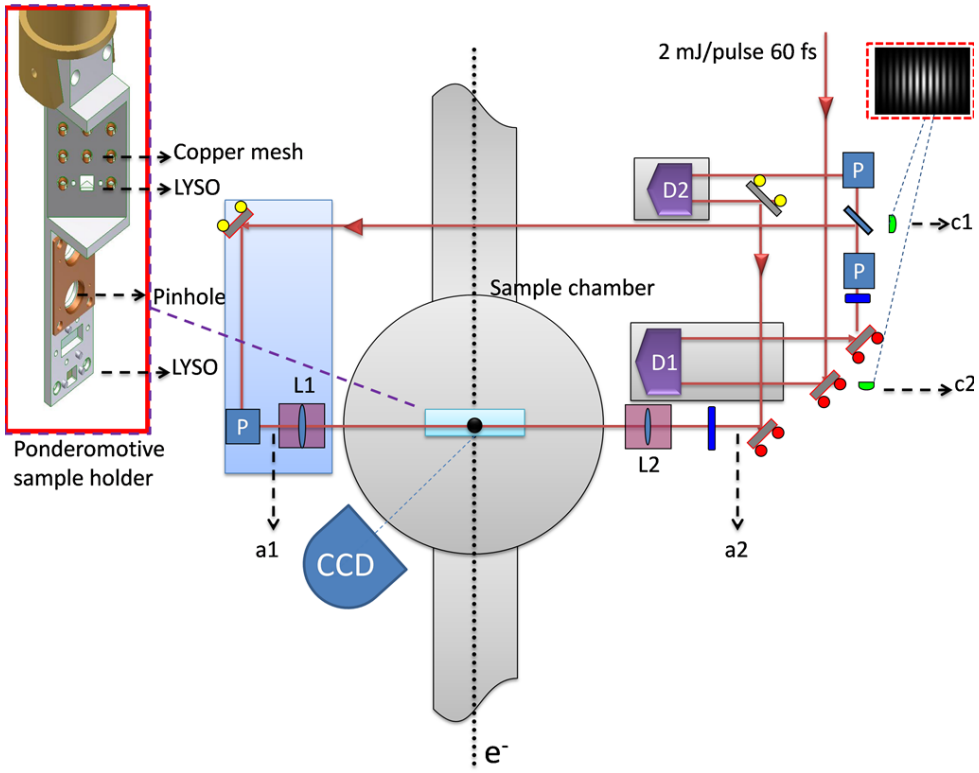

Figure 6.5: Schematic drawing of REGAE ponderomotive setup. One laser beam (2 mJ/pulse, 60 fs) is sent to a delay line (D1: 305 mm travel range) and split into two (a1 and a2) counterpropagating laser pulses. They interact with the electron beam (e^-) in the sample chamber. A small delay line (D2: 25 mm travel range) is used to balance the two arms. CCD (c1 and c2) and motorized mirrors are used to monitor and optimize the standing wave. Insert: ponderomotive sample holder.

envelope function is defined as $E_{nv} = E_0 \frac{w_0}{w} e^{\frac{r^2}{\omega^2}} \mathrm{Sech}(\xi/\xi_0)$ with the peak amplitude E_0, beam radius ω_0 at the beam waist, transverse position $r = \sqrt{x^2 + y^2}$, and phase ξ. The field components write as:

$$\begin{aligned} E_x &= E_{nv} \cos \Psi \\ E_y &= 0 \\ E_x &= -\frac{x}{Z_R} \frac{w_0^2}{w^2} E_{nv} (\sin \Psi + \varsigma \cos \Psi) \\ B_x &= 0 \\ B_y &= E_x \\ B_z &= -\frac{y}{Z_R} \frac{w a_0^2}{w^2} E_{nv} (\sin \Psi + \varsigma \cos \Psi) \end{aligned} \tag{6.2}$$

where $\Psi = \xi + \varphi_{CE} + \varphi_G + \frac{\zeta r^2}{w^2}$ with the Gouy phase $\varphi_G = \arctan(\zeta)$, the carrier envelope phase φ_{CE}, and the phase $\xi = \omega t - kz$.

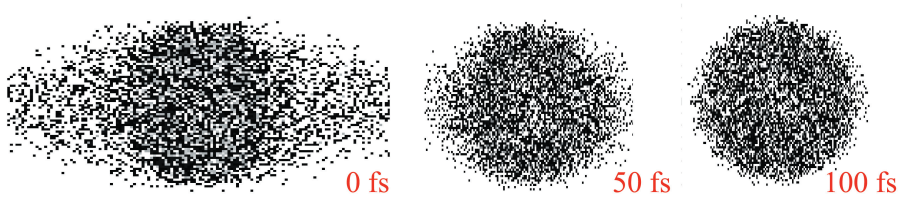

Figure 6.6: Simulated electron beam images on the detector after interaction with a 60 fs laser pulse. The electron beam is stripped by a 30 μm pinhole before interacting with the laser beam (25 μm beam diameter, 60fs, 1 mJ/pulse). The image shows the scattering with different time delay (0 fs, 50 fs and 100 fs). ASTRA simulation based on REGAE, see Appendix A.

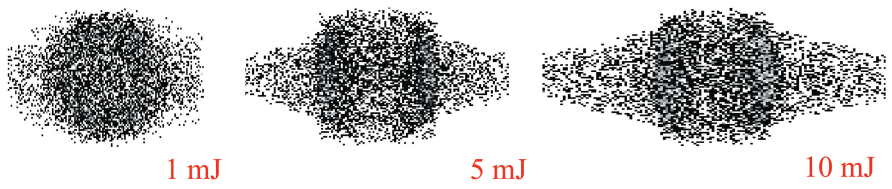

Figure 6.7: Laser power dependence of the ponderomotive scattering. ASTRA simulation based on REGAE, see Appendix A.

Based on REGAE design parameters the simulation uses 10^6 electrons, and a 30 μm pin hole (Namelist: Aperture) just in front of laser-electron crossing to clean up the beam (10^4 electrons pass through the pin hole). Space-charge effect is also included.

After laser-electron interaction the electron beam propagates 4.5 meters to the detector. In the simulation we use two counterpropergating laser beams. The standing wave leads to an enhancement in the ponderomotive force, which is 100 times stronger than that of a single propagating pulse in the lateral direction [23]. Figure 6.6 shows the simulated intersection profile at the detector position. At t = 100 fs there is no temporal overlap between the electron pulse and the optical grating, while at t = 0 the temporal overlap is optimum. The dependence of the amount of scattered electrons on the laser intensity is shown in Fig. 6.7. Higher laser fluence leads to better scattering signal. The force is linearly proportional to the laser intensity, which is also predicted by Eq. 6.1. The simulation follows our current beam line configuration and uses reasonable laser power (2 mJ/pulse with 60 fs (FWHM) considering dispersion along the 10 meter beam line). It shows good and visible scattering at the detector position, which helps to guide our next step to perform the experiment.

6.3. Conclusion

In this chapter, the first experiment to find nanosecond and picosecond time zero of REGAE is described. Simulation of ponderomotive force for REGAE is done with ASTRA.

1. A CCD camera with gated intensifier provides ns time zero measurement. It helps to set the initial position of the delay line. Single-shot gold melting is performed to find ps time zero. It provides a direct and visible way to find time zero.

2. Ponderomotive force is one of the best methods to measure the electron bunch length and time zero. ASTRA simulations are performed to check the setting of the beam line and the laser. It gives us a firsthand information of the feasibility of this method.

The precise measurement of REGAE bunch length and time zero with ponderomotive is now under schedule. It helps to fine tune the buncher cavity to get the shortest electron pulse duration.

7. Summary and outlook

Recent advances in ultrashort hard X-ray and electron pulses have made it possible the observation of dynamical phenomena with atomic spatial and ∼100 fs temporal resolutions. In only 30 years the brightness of femtosecond hard X-ray pulses has been boosted by about one billion times. Nowadays, X-ray free electron lasers (XFELs) produce ultrashort hard X-ray pulses with sufficient brightness (10^{12} photons/pulse) to obtain high quality diffraction in a single shot. On the other hand, ultrabright electron sources with different schemes for electron pulse compression have become a very convenient approach providing an effective brightness close to that of XFELs.

This thesis presented the development of two different ultrabright electron sources and their application in femtosecond electron diffractometers. Related optical setups such as SHG, THG lines, and a NOPA delivered different excitation wavelengths. An Autocorrelator, a FROG, and a cross-correlator served as optical beam characterization and diagnostic tools. Proper manipulation of the UV beam was found to be crucial to obtain the required profiles, both spatial and temporal, to reduce the electron beam emittance in our REGAE apparatus, i.e. increase the transverse coherence length at the sample.

The first time-resolved study in our group involved the development of a femtosecond optical pump-probe setup. The study of Au/VO_2 thin films revealed a new kind of ultrafast SMT phase transition which was induced by the injection of hot carriers into the VO_2 layer. The effects of fs UV irradiation on alkali halides were studied with a variety of different techniques, including FED. A novel cold ablation process, different from plasma ablation and coulomb explosion, has been observed for the first time and reflected the very repulsive nature of the transient excited state. Single shot electron diffraction experiments of alkaline halides helped us understand the initial structural changes driving this cold ablation process. The development of a compact 150 keV FED table-top setup (Egun300) was fundamental for this study which represented the first FED study at the Max Planck Institute for the Structure and Dynamics of Matter. In order to reduce the space-charge induced pulse broadening, higher acceleration voltage as well as shorter time of flight were implemented in this new setup.

REGAE is still under development, with its first time-resolved FED experiment commissioned quite recently. This study was performed to find the time zero and demonstrated the ability to observe structural dynamics under nonreversible photoexcitation conditions. This was a nontrivial task when considering the complexity of this 10 meter long system. We were finally able to observe the loss of long crystalline order in polycrystalline Au and found time zero within 1 ps (with only ∼3 shots per time delay).

After over three years of developments, our group finally counts with this compact FED and REGAE which is coming along.

New generation of FED systems will provide even shorter bunch length with higher brightness. Ponderomotive scattering will provide the ability to fully characterize electron pulses in the sub 100 fs regime. This will help us to further optimize REGAE and its rebunching cavity in order to see even the fastest nuclear motions involved in chemical and biological reactions.

REGAE has showed its pronounced penetration depth. High quality diffraction data was obtained from up to one micron thick Al samples (Fig. 7.1). It will make it possible the exploration of structural dynamics in solution phase through the implementation of nanofluidic cells [180] which are being developed in our group.

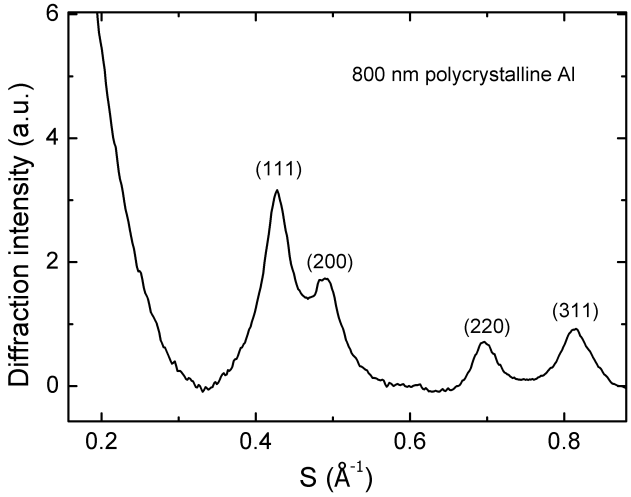

Figure 7.1: Radially averaged intensity profile from 800 nm polycrystalline Aluminium diffraction.

Appendix

A. ASTRA Codes

A Space Charge Tracking Algorithm (ASTRA) [32] is used in this thesis to simulate the beam dynamics and characterize the setups. It is based on the 3D particle tracking techniques, which provides charged particle dynamics in external electromagnetic field.

ASTRA program package consists of four main parts: **Generator** generates the initial particles, **Astra** tracks the particles under the influence of fields, **Fieldplot** that displays the fields of beam line elements, **Postpro** displays phase space plots, and **Lineplot** displays beam size, emittance, bunch length, etc.

In this thesis two electrons sources are considered: Egun300 that uses direct current acceleration and Relativistic (REGAE: 3∼5 MeV) electron gun that is based on radio frequency 3 GHz time-varying electric field. Simulations provide insight to design, development and experiments for our study. The main parameters for these two setups are listed in table A.1. All simulations in this thesis are based on these fundamental settings.

	Egun300 (150 keV) gun	REGAE
Charge	1 fc	100 fc
Laser pulse duration (FWHM)	100 fs	1 ps
Laser spot size on the cathode (FWHM)	200 μm	20 μm
Sample-cathode distance	20 mm	5.5 m
Sample-detector distance	50 cm	5 m

Table A.1: Parameters for Egun300 and REGAE in ASTRA simulation.

ASTRA simulations are also helpful to determine the basic setting in experiments for generating specific electron beam size, bunch length, coherence length, etc. Especially for the relativistic electron source, which consists of many parts and flexible parameters when operating the machine, it is important to know in advance if we are tuning in the right direction.

The basic settings for different Namlists are listed below:

A.1. Generator

```
&INPUT
FNAME = 'rfgun.ini'
IPart=10000
Species='electrons'
Probe=.F.
```

```
Noise_reduc=.T.
Cathode=.T.
Q_total= 8.0000E-05,
Ref_zpos=0.0E0,
Ref_clock=0.0E0,
Ref_Ekin=0.0E0,
Dist_z='u',
sig_clock=0.001E0,
Dist_pz='i',
LE=0.0005
Dist_x='r',
sig_x=1E0,
/
```

A.2. ASTRA

```
&NEWRUN
Head='REGAE'
RUN=1,
Loop=F, Nloop=2,
Distribution = 'rfgun.ini', Xoff=0.E-3, Yoff=0.0,
XYrms = 7.0000E-03,
Trms = 5.0000E-04,
Qbunch = 8.0000E-05,
Track_All = T , Auto_Phase = T , Phase_Scan = F
Check_Ref_Part = F
H_max = 1.0000E-03,
H_min = 0.000,
/

  &OUTPUT
ZStart = 0.000 , ZStop = 8.000,
Zemit = 500, Zphase = 1,
PhaseS = T
EmitS = T,
RefS = T
CathodeS = F
/

  &CHARGE
LSpCh = T
N_min = 100.00,
Max_Scale = 5.0000E-02
Max_Count = 20,
```

```
Exp_Control = 0.1000,
Lmirror = T
Nrad = 15, Cell_Var = 2.000,
Nlong_in = 40,
/

   &Aperture
LApert=T
File_Aperture(1)='RAD'
Ap_Z1(1)=5.4
Ap_Z2(1)=5.41
Ap_R(1)=0.03
/

   &CAVITY
LEfield = T

File_Efield(1) = 'REGAE_GUN.dat'
C_higher_order(1) = T
Nue(1) = 2.998 ,
MaxE(1) = 30.0 , Phi(1) = 0.00000 ,

File_Efield(2) = 'Buncher.dat'
C_higher_order(2) = T
Nue(2) = 2.998 ,
MaxE(2) = 25.00 , Phi(2) = -90.0000,
C_pos(2) = 1.290 ,
/

   &SOLENOID
LBfield = T

File_Bfield(1) = 'Bsol_single.dat'
S_smooth(1) = 4,
MaxB(1) = 0.1600 ,
S_pos(1) = 0.551 ,

File_Bfield(2) = 'Bsol_open1.dat'
S_smooth(2) = 4
MaxB(2) = 0.1100 ,
S_pos(2) = 0.93 ,
/
```

B. Coupled-wave equation

Numerical solutions of Coupled-wave equation equations govern the z-propagation of fundamental and second harmonic fields E_1 and E_2 in a quadratic nonlinear medium are

$$\begin{aligned}(\frac{\partial}{\partial z}+\frac{iL_{\mathrm{NL}}}{2L_{\mathrm{D1}}}\frac{\partial^2}{\partial t^2})E_1 &= iE_1^*E_2\exp(i\Delta kz)+i2\pi(n_2I_0)\\ &\times\frac{L_{\mathrm{NL}}}{\lambda}(|E_1|^2+2|E_2|^2)E_1,\\ (\frac{\partial}{\partial z}+\frac{L_{\mathrm{NL}}}{L_{\mathrm{GVM}}}\frac{\partial}{\partial t}+\frac{iL_{\mathrm{NL}}}{2L_{D2}}\frac{\partial^2}{\partial t^2})E_2 &= iE_1E_1\exp(-i\Delta kz)+i4\pi(n_2I_0)\\ &\times\frac{L_{\mathrm{NL}}}{\lambda}(2|E_1|^2+|E_2|^2)E_2\end{aligned} \tag{B.1}$$

With the parameters defined by:

$$\begin{aligned}\Delta k &= k_{2\omega}-2k_{\omega},\\ L_{\mathrm{NL}}=\frac{2nc}{\chi^2E_0\omega}, L_{\mathrm{GVM}} &= t_0(1/v_{g2}-1/v_{g1})^{-1},\\ L_{\mathrm{D1}} &= \tau_0^2/\beta_1^{(2)}, L_{D2}=\tau_0^2/\beta_2^{(2)}\end{aligned}$$

E_1 and E_2 are in units of the initial peak FH field E_0, which is related to the initial peak FH intensity by $I_0=\varepsilon_0nc|E_0|^2/2, wheren_2$ is Kerr nonlinear index, Δk is phase-mismatch term. Propagation distance z is normalized to the nonlinear interaction length L_{NL} that measures the initial laser intensity, and time t is in units of the initial FH pulse duration τ_0 in a retarded frame. v_{g1} (v_{g2}) and $\beta_1^{(2)}$ ($\beta_2^{(2)}$) are the group velocity and group-velocity dispersion parameters at FH (SH) wavelength, respectively.

We assume the initial FH is a Gaussian pulse $E_1(0,t)=E_0\exp(-t^2/t_0^2)$, with the pulse duration $\tau_0=2\sqrt{\ln 2}t_0$. We can slice the nonlinear medium into small parts and solve the equations with Runge–Kutta methods step by step. For each step we change the equations into frequency domain and treat the real and imaginary part separately. The simplified Coupled-wave equation equations can be solved, which provides numerical solution of FH and SH after nonlinear medium.

In the case of SHG generation, we set the initial FH pulse duration τ_0 = 40 fs. The initial SH field was set zero. BBO crystal for FH (800 nm) and SH (400 nm) is chosen with cutting angle θ_{BBO} = 29.2 degree, ϕ_{BBO} = 90 degree, refractive index (FH) = 1.660282 and refractive index (SH) = 1.630291, Group velocity mismatch (GVM) = 193.664 fs/mm, deff = 2.00 pm/V, Group velocity dispersion GVD_{FH} = 74.69 fs^2/mm and GVD_{SH} = 195.971 fs^2/mm.

Bibliography

[1] http://slac.stanford.edu/.

[2] http://www.xfel.eu/.

[3] http://sacla.xfel.jp/?lang=en/.

[4] http://www.psi.ch/.

[5] A. M. Lindenberg, J. Larsson, K. Sokolowski-Tinten, K. J. Gaffney, C. Blome, O. Synnergren, J. Sheppard, C. Caleman, A. G. MacPhee, D. Weinstein, D. P. Lowney, T. K. Allison, T. Matthews, R. W. Falcone, A. L. Cavalieri, D. M. Fritz, S. H. Lee, P. H. Bucksbaum, D. A. Reis, J. Rudati, P. H. Fuoss, C. C. Kao, D. P. Siddons, R. Pahl, J. Als-Nielsen, S. Duesterer, R. Ischebeck, H. Schlarb, H. Schulte-Schrepping, T. Tschentscher, J. Schneider, D. von der Linde, O. Hignette, F. Sette, H. N. Chapman, R. W. Lee, T. N. Hansen, S. Techert, J. S. Wark, M. Bergh, G. Huldt, D. van der Spoel, N. Timneanu, J. Hajdu, R. A. Akre, E. Bong, P. Krejcik, J. Arthur, S. Brennan, K. Luening, J. B. Hastings, Atomic-scale visualization of inertial dynamics, Science 308 (5720) (2005) 392–395.

[6] B. J. Siwick, J. R. Dwyer, R. Jordan, R. J. D. Miller, An atomic-level view of melting using femtosecond electron diffraction, Science 302 (5649) (2003) 1382–5.

[7] M. Eichberger, H. Schaefer, M. Krumova, M. Beyer, J. Demsar, H. Berger, G. Moriena, G. Sciaini, R. J. D. Miller, Snapshots of cooperative atomic motions in the optical suppression of charge density waves, Nature 468 (2010) 799–802.

[8] G. Sciaini, M. Harb, S. G. Kruglik, T. Payer, C. T. Hebeisen, F.-J. Heringdorf, M. Yamaguchi, M. H. Hoegen, R. Ernstorfer, D. R. J. Miller, Electronic acceleration of atomic motions and disordering in bismuth, Nature 458 (7234) (2009) 56–59.

[9] P. Musumeci, J. T. Moody, C. M. Scoby, Relativistic electron diffraction at the UCLA pegasus photoinjector laboratory, Ultramicroscopy 108 (11) (2008) 1450 – 1453.

[10] Y. Murooka, N. Naruse, S. Sakakihara, M. Ishimaru, J. Yang, K. Tanimura, Transmission-electron diffraction by MeV electron pulses, Applied Physics Letters 98 (25) (2011) 251903.

[11] R. Henderson, The potential and limitations of neutrons, electrons and X-rays for atomic resolution microscopy of unstained biological molecules, Quarterly Reviews of Biophysics 28 (1995) 171–193.

[12] http://regae.desy.de/.

[13] G. Mourou, S. Williamson, Picosecond electron diffraction, Applied Physics Letters 41 (1) (1982) 44–45.

[14] S. Williamson, G. Mourou, J. C. M. Li, Time-resolved laser-induced phase transformation in aluminum, Phys. Rev. Lett. 52 (1984) 2364–2367.

[15] H. E. Elsayed-Ali, G. A. Mourou, Picosecond reflection high-energy electron diffraction, Applied Physics Letters 52 (2) (1988) 103–104.

[16] R. Srinivasan, V. A. Lobastov, C.-Y. Ruan, A. H. Zewail, Ultrafast electron diffraction (ued), Helvetica ChimicaActa 86 (6) (2003) 1761–1799.

[17] J. C. Williamson, M. Dantus, S. B. Kim, A. H. Zewail, Ultrafast diffraction and molecular structure, Chemical Physics Letters 196 (6) (1992) 529 – 534.

[18] M. Aidelsburger, F. O. Kirchner, F. Krausz, P. Baum, Single-electron pulses for ultrafast diffraction, Proceedings of the National Academy of Sciences 107 (46) (2010) 19714–19719.

[19] A. Gahlmann, S. Tae Park, A. H. Zewail, Ultrashort electron pulses for diffraction, crystallography and microscopy: theoretical and experimental resolutions, Phys. Chem. Chem. Phys. 10 (20) (2008) 2894–2909.

[20] P. Baum, A. H. Zewail, Breaking resolution limits in ultrafast electron diffraction and microscopy, Proceedings of the National Academy of Sciences 103 (44) (2006) 16105–16110, PMID: 17056711.

[21] B. J. Siwick, A. A. Green, C. T. Hebeisen, R. J. D. Miller, Characterization of ultrashort electron pulses by electron-laser pulse cross correlation, Opt. Lett. 30 (9) (2005) 1057–1059.

[22] C. T. Hebeisen, R. Ernstorfer, M. Harb, T. Dartigalongue, R. E. Jordan, R. J. D. Miller, Femtosecond electron pulse characterization using laser ponderomotive scattering, Opt. Lett. 31 (23) (2006) 3517–3519.

[23] C. T. Hebeisen, G. Sciaini, M. Harb, R. Ernstorfer, T. Dartigalongue, S. G. Kruglik, R. J. D. Miller, Grating enhanced ponderomotive scattering for visualization and full characterization of femtosecond electron pulses, Opt. Express 16 (5) (2008) 3334–3341.

[24] J. R. Dwyer, C. T. Hebeisen, R. Ernstorfer, M. Harb, V. B. Deyirmenjian, R. E. Jordan, R. J. D. Miller, Femtosecond electron diffraction: 'making the molecular movie', Royal Society of London Philosophical Transactions Series A 364 (2006) 741–778.

[25] M. Gao, H. Jean-Ruel, R. R. Cooney, J. Stampe, M. de Jong, M. Harb, G. Sciaini, G. Moriena, R. J. D. Miller, Full characterization of RF compressed femtosecond electron pulses using ponderomotive scattering, Opt. Express 20 (11) (2012) 12048–12058.

[26] R. P. Chatelain, V. R. Morrison, C. Godbout, B. J. Siwick, Ultrafast electron diffraction with radio-frequency compressed electron pulses, Applied Physics Letters 101 (8) (2012) 081901.

[27] M. Harb, R. Ernstorfer, T. Dartigalongue, C. T. Hebeisen, R. E. Jordan, R. J. D. Miller, Carrier relaxation and lattice heating dynamics in silicon revealed by femtosecond electron diffraction, The Journal of Physical Chemistry B 110 (50) (2006) 25308–25313.

[28] M. Harb, R. Ernstorfer, C. T. Hebeisen, G. Sciaini, W. Peng, T. Dartigalongue, M. A. Eriksson, M. G. Lagally, S. G. Kruglik, R. J. D. Miller, Electronically driven structure changes of Si captured by femtosecond electron diffraction, Phys. Rev. Lett. 100 (2008) 155504.

[29] R. Ernstorfer, M. Harb, C. T. Hebeisen, G. Sciaini, T. Dartigalongue, R. J. D. Miller, The formation of warm dense matter: Experimental evidence for electronic bond hardening in gold, Science 323 (5917) (2009) 1033–1037.

[30] M. Gao, C. Lu, H. Jean-Ruel, L. C. Liu, A. Marx, K. Onda, S. ya Koshihara, Y. Nakano, X. Shao, T. Hiramatsu, G. Saito, H. Yamochi, R. R. Cooney, G. Moriena, G. Sciaini, R. J. D. Miller, Mapping molecular motions leading to charge delocalization with ultrabright electrons, Nature (7445) (2013) 343–346.

[31] R. J. D. Miller, R. Ernstorfer, M. Harb, M. Gao, C. T. Hebeisen, H. Jean-Ruel, C. Lu, G. Moriena, G. Sciaini, 'Making the molecular movie': first frames, Acta Crystallographica Section A 66 (2) (2010) 137–156.

[32] http://www.desy.de/∼ mpyflo/.

[33] http://www.coherent.com/.

[34] D. Strickland, G. Mourou, Compression of amplified chirped optical pulses, Optics Communications 55 (1985) 447–449.

[35] M. Pittman, S. Ferré, J. P. Rousseau, L. Notebaert, J. P. Chambaret, G. Chériaux, Design and characterization of a near-diffraction-limited femtosecond 100-TW 10-Hz high-intensity laser system, Applied Physics B 74 (6) (2002) 529–535.

[36] M. Aoyama, K. Yamakawa, Y. Akahane, J. Ma, N. Inoue, H. Ueda, H. Kiriyama, 0.85-PW, 33-fs Ti:sapphire laser, Opt. Lett. 28 (17) (2003) 1594–6.

[37] M. D. Perry, D. Pennington, B. C. Stuart, G. Tietbohl, J. A. Britten, C. Brown, S. Herman, B. Golick, M. Kartz, J. Miller, H. T. Powell, M. Vergino, V. Yanovsky, Petawatt laser pulses, Opt. Lett. 24 (3) (1999) 160–2.

[38] S. Backus, C. G. Durfee III, M. M. Murnane, H. C. Kapteyn, High power ultrafast lasers, Review of Scientific Instruments 69 (3) (1998) 1207–1223.

[39] D. J. Kane, R. Trebino, Characterization of arbitrary femtosecond pulses using frequency-resolved optical gating, Quantum Electronics, IEEE Journal of 29 (2) (1993) 571–579.

[40] J. A. Armstrong, Measurement of picosecond laser pulse widths, Applied Physics Letters 10 (1) (1967) 16–18.

[41] C. Iaconis, M. E. Anderson, I. A. Walmsley, Spectral phase interferometry for direct electric field reconstruction of ultrashort optical pulses, in: Ultrafast Phenomena XI, Vol. 63 of Springer Series in Chemical Physics, Springer Berlin Heidelberg, 1998, pp. 103–105.

[42] F. Salin, P. Georges, G. Roger, A. Brun, Single-shot measurement of a 52-fs pulse, Appl. Opt. 26 (21) (1987) 4528–4531.

[43] D. Zhang, L. Qian, P. Yuan, H. Zhu, S. Wen, C. Xu, Fiber-array-based detection scheme for single-shot pulse contrast characterization, Opt. Lett. 33 (17) (2008) 1969–1971.

[44] J. Ma, P. Yuan, Y. Wang, D. Zhang, H. Zhu, L. Qian, Single-shot cross-correlator using a long-wavelength sampling pulse, Opt. Lett. 36 (6) (2011) 978–980.

[45] R. Trebino, Frequency-Resolved Optical Gating: The Measurement of Ultrashort Laser Pulses, Springer, New York, NY, 2002.

[46] http://www.femtosoft.biz.

[47] N. K. Fontaine, C. Ji, R. G. Broeke, J. Cao, S.-W. Seo, S. J. B. Yoo, K. Y. Liou, J. R. Lothian, S. Vatanapradit, S.-N. G. Chu, B. Patel, W. S. Hobson, W. T. Tsang, XFROG characterization of a 10 GHz colliding-pulse mode-locked laser, in: Lasers and Electro-Optics, 2006 and 2006 Quantum Electronics and Laser Science Conference. CLEO/QELS 2006., 2006, pp. 1–2.

[48] S. Linden, J. Kuhl, H. Giessen, Amplitude and phase characterization of weak blue ultrashort pulses by downconversion, Opt. Lett. 24 (8) (1999) 569–571.

[49] D. J. Kane, A. J. Taylor, R. Trebino, K. W. DeLong, Single-shot measurement of the intensity and phase of a femtosecond uv laser pulse with frequency-resolved optical gating, Opt. Lett. 19 (14) (1994) 1061–1063.

[50] J. N. Sweetser, D. N. Fittinghoff, R. Trebino, Transient-grating frequency-resolved optical gating, Opt. Lett. 22 (8) (1997) 519–521.

[51] P. O'Shea, M. Kimmel, X. Gu, R. Trebino, Highly simplified device for ultrashort-pulse measurement, Opt. Lett. 26 (12) (2001) 932–934.

[52] S. Imai, T. Yamada, Y. Fujimori, K. Ishikawa, Third-harmonic generation of an alexandrite laser in $\beta - BaB_2O_4$, Applied Physics Letters 54 (13) (1989) 1206–1208.

[53] P. S. Banks, M. D. Feit, M. D. Perry, High-intensity third-harmonic generation, J. Opt. Soc. Am. B 19 (1) (2002) 102–118.

[54] F. Xu, J. Liao, C.-S. Guo, J.-L. He, H.-T. Wang, S. N. Zhu, Z. Wang, Y. Y. Zhu, N. B. Ming, Highly efficient direct third-harmonic generation based on control of the electro-optic effect in quasi-periodic optical superlattices, Opt. Lett. 28 (6) (2003) 429–431.

[55] D. Zhang, L. Qian, K. Wang, H. Zhu, Influence of cascaded nonlinear phase shifts on second-harmonic generation in high-intensity pumped QPM structures, Chinese Physics Letters 25 (10) (2008) 3685.

[56] K. Wang, L. Qian, D. Zhang, H. Yang, H. Zhu, Cascaded nonlinear phase shifts in quasi-phase-matched structures, Phys. Rev. A 76 (2007) 013805.

[57] I. Will, G. Klemz, Generation of flat-top picosecond pulses by coherent pulse stackingin a multicrystal birefringent filter, Opt. Express 16 (19) (2008) 14922–14937.

[58] C. W. Hillegas, J. X. Tull, D. Goswami, D. Strickland, W. S. Warren, Femtosecond laser pulse shaping by use of microsecond radio-frequency pulses, Opt. Lett. 19 (10) (1994) 737–739.

[59] B. J. Pearson, T. C. Weinacht, Shaped ultrafast laser pulses in the deep ultraviolet, Opt. Express 15 (7) (2007) 4385–4388.

[60] S.-H. Shim, D. B. Strasfeld, E. C. Fulmer, M. T. Zanni, Femtosecond pulse shaping directly in the mid-IR using acousto-optic modulation, Opt. Lett. 31 (6) (2006) 838–840.

[61] T. Tanigawa, Y. Sakakibara, S. Fang, T. Sekikawa, M. Yamashita, Spatial light modulator of 648 pixels with liquid crystal transparent from ultraviolet to near-infrared and its chirp compensation application, Opt. Lett. 34 (11) (2009) 1696–1698.

[62] S. Cialdi, M. Petrarca, C. Vicario, High-power third-harmonic flat pulse laser generation, Opt. Lett. 31 (19) (2006) 2885–2887.

[63] K. Floettmann, Note on the thermal emittance of electrons emitted by cesium telluride photo cathodes, TESLA-FEL report 9 (1997) 1997–01.

[64] G. Cerullo, S. De Silvestri, Ultrafast optical parametric amplifiers, Review of Scientific Instruments 74 (1) (2003) 1–18.

[65] G. Cerullo, M. Nisoli, S. De Silvestri, Generation of 11 fs pulses tunable across the visible by optical parametric amplification, Applied Physics Letters 71 (25) (1997) 3616–3618.

[66] P. Tzankov, J. Zheng, M. Mero, D. Polli, C. Manzoni, G. Cerullo, 300 μj non-collinear optical parametric amplifier in the visible at 1 kHz repetition rate, Opt. Lett. 31 (24) (2006) 3629–3631.

[67] T. Wilhelm, J. Piel, E. Riedle, Sub-20-fs pulses tunable across the visible from a blue-pumped single-pass noncollinear parametric converter, Opt. Lett. 22 (19) (1997) 1494–1496.

[68] L.-S. Ma, Z. Bi, A. Bartels, K. Kim, L. Robertsson, M. Zucco, R. S. Windeler, G. Wilpers, C. Oates, L. Hollberg, S. A. Diddams, Frequency uncertainty for optically referenced femtosecond laser frequency combs, Quantum Electronics, IEEE Journal of 43 (2) (2007) 139–146.

[69] A. H. Zewail, Femtochemistry: Atomic-scale dynamics of the chemical bond, The Journal of Physical Chemistry A 104 (24) (2000) 5660–5694.

[70] A. Bartels, F. Hudert, C. Janke, T. Dekorsy, K. Köhler, Femtosecond time-resolved optical pump-probe spectroscopy at kilohertz-scan-rates over nanosecond-time-delays without mechanical delay line, Applied Physics Letters 88 (4) (2006) 041117.

[71] J. A. Valdmanis, G. Mourou, C. W. Gabel, Picosecond electro-optic sampling system, Applied Physics Letters 41 (3) (1982) 211–212.

[72] C. Fattinger, D. Grischkowsky, Terahertz beams, Applied Physics Letters 54 (6) (1989) 490–492.

[73] G. D. Goodno, G. Dadusc, R. J. D. Miller, Ultrafast heterodyne-detected transient-grating spectroscopy using diffractive optics, J. Opt. Soc. Am. B 15 (6) (1998) 1791–1794.

[74] S. Tokita, S. Inoue, S. Masuno, M. Hashida, S. Sakabe, Single-shot ultrafast electron diffraction with a laser-accelerated sub-MeV electron pulse, Applied Physics Letters 95 (11) (2009) 111911.

[75] T. van Oudheusden, E. F. de Jong, S. B. van der Geer, W. P. E. M. Op 't Root, O. J. Luiten, B. J. Siwick, Electron source concept for single-shot sub-100 fs electron diffraction in the 100 keV range, Journal of Applied Physics 102 (9) (2007) 093501.

[76] A. Janzen, B. Krenzer, O. Heinz, P. Zhou, D. Thien, A. Hanisch, F. J. Meyer zu Heringdorf, D. von der Linde, M. Horn von Hoegen, A pulsed electron gun for ultrafast electron diffraction at surfaces, Review of Scientific Instruments 78 (1) (2007) 013906.

[77] P. A. Anderson, Work function of gold, Phys. Rev. 115 (1959) 553–554.

[78] S. Schreiber, J. Hui Han, P. Michelato, L. Monaco, D. Sertore, Properties of cathodes used in the photoinjector RF gun at the DESY VUV-FEL, Proceedings of EPAC 2004 (2004) 3 p.

[79] V. E. Cosslett, Introduction to electron optics: the production, propagation and focusing of electron beams, Clarendon Press, 1950.

[80] V. Kumar, Understanding the focusing of charged particle beams in a solenoid magnetic field, American Journal of Physics 77 (2009) 737–741.

[81] M. Harb, W. Peng, G. Sciaini, C. T. Hebeisen, R. Ernstorfer, M. A. Eriksson, M. G. Lagally, S. G. Kruglik, R. J. D. Miller, Excitation of longitudinal and transverse coherent acoustic phonons in nanometer free-standing films of (001) Si, Phys. Rev. B 79 (2009) 094301.

[82] J. B. Hastings, F. M. Rudakov, D. H. Dowell, J. F. Schmerge, J. D. Cardoza, J. M. Castro, S. M. Gierman, H. Loos, P. M. Weber, Ultrafast time-resolved electron diffraction with megavolt electron beams, Applied Physics Letters 89 (18) (2006) 184109.

[83] R. Li, C. Tang, Y. Du, W. Huang, Q. Du, J. Shi, L. Yan, X. Wang, Experimental demonstration of high quality MeV ultrafast electron diffraction, Review of Scientific Instruments 80 (8) (2009) 083303.

[84] X. J. Wang, Z. Wu, H. Ihee, Femto-seconds electron beam diffraction using photocathode RF gun, in: Particle Accelerator Conference, 2003. PAC 2003. Proceedings of the (Volume:1), Vol. 1, 2003, pp. 420–422.

[85] C. M. Pepin, P. Berard, A. L. Perrot, C. Pepin, D. Houde, R. Lecomte, C. L. Melcher, H. Dautet, Properties of LYSO and recent LSO scintillators for phoswich PET detectors, Nuclear Science, IEEE Transactions on 51 (3) (2004) 789–795.

[86] H. Delsim-Hashemi, K. Flöttmann, M. Seebach, S. Bayesteh, Charge monitors at the relativistic electron gun for atomic exploration – REGAE, Proceedings of IBIC2013 WEPF24 (2013) 868–871.

[87] M. Hada, D. Zhang, A. Casandruc, R. J. D. Miller, Y. Hontani, J. Matsuo, R. E. Marvel, R. F. Haglund, Hot electron injection driven phase transitions, Phys. Rev. B 86 (2012) 134101.

[88] P. Rohwetter, J. Kasparian, K. Stelmaszczyk, Z. Hao, S. Henin, N. Lascoux, W. M. Nakaema, Y. Petit, M. Queiszer, R. Salame, E. Salmon, L. Woste, J.-P. Wolf, Laser-induced water condensation in air, Nature Photonics 4 (7) (2010) 451–456.

[89] M. F. Becker, A. B. Buckman, R. M. Walser, T. Lépine, P. Georges, A. Brun, Femtosecond laser excitation of the semiconductor-metal phase transition in VO_2, Applied Physics Letters 65 (12) (1994) 1507–1509.

[90] S. Iwai, M. Ono, A. Maeda, H. Matsuzaki, H. Kishida, H. Okamoto, Y. Tokura, Ultrafast optical switching to a metallic state by photoinduced mott transition in a halogen-bridged nickel-chain compound, Phys. Rev. Lett. 91 (2003) 057401.

[91] D. Polli, M. Rini, S. Wall, R. Schoenlein, Y. Tomioka, Y. Tokura, G. Cerullo, A. Cavalleri, Coherent orbital waves in the photo-induced insulator-metal dynamics of a magnetoresistive manganite, Nat Mater 6 (9) (2007) 643–7.

[92] D. Lederman, E. Osquiguil, G. Nieva, J. Guimpel, J. Hasen, Y. Bruynseraede, I. Schuller, Photoinduced enhancement of superconductivity, Journal of Superconductivity 7 (1) (1994) 127–130.

[93] D. Fausti, R. I. Tobey, N. Dean, S. Kaiser, A. Dienst, M. C. Hoffmann, S. Pyon, T. Takayama, H. Takagi, A. Cavalleri, Light-induced superconductivity in a stripe-ordered cuprate, Science 331 (6014) (2011) 189–191.

[94] R. Y. N. Gengler, D. S. Badali, D. Zhang, K. Dimos, K. Spyrou, D. Gournis, R. J. D. Miller, Revealing the ultrafast process behind the photoreduction of graphene oxide, Nature Communications 4 (2560) (2013) 3560+.

[95] M. Imada, A. Fujimori, Y. Tokura, Metal-insulator transitions, Rev. Mod. Phys. 70 (1998) 1039–1263.

[96] M. Eichberger, H. Schaefer, M. Krumova, M. Beyer, J. Demsar, H. Berger, G. Moriena, G. Sciaini, R. J. D. Miller, Snapshots of cooperative atomic motions in the optical suppression of charge density waves, Nature 468 (2010) 799–802.

[97] F. J. Morin, Oxides which show a metal-to-insulator transition at the neel temperature, Phys. Rev. Lett. 3 (1959) 34–36.

[98] N. F. Mott, Metal-Insulator Transition, Reviews of Modern Physics 40 (1968) 677–683.

[99] A. Cavalleri, C. Tóth, C. W. Siders, J. A. Squier, F. Ráksi, P. Forget, J. C. Kieffer, Femtosecond structural dynamics in VO_2 during an ultrafast solid-solid phase transition, Phys. Rev. Lett. 87 (2001) 237401.

[100] G. Stefanovich, A. Pergament, D. Stefanovich, Electrical switching and Mott transition in VO_2, Journal of Physics: Condensed Matter 12 (41) (2000) 8837.

[101] V. Eyert, The metal-insulator transitions of VO_2: A band theoretical approach, Ann. Phys. (Leipzig) 11 (cond-mat/0210558) (2002) 648–700. 61 p.

[102] H.-T. Kim, Y. W. Lee, B.-J. Kim, B.-G. Chae, S. J. Yun, K.-Y. Kang, K.-J. Han, K.-J. Yee, Y.-S. Lim, Monoclinic and correlated metal phase in VO_2 as evidence of the mott transition: Coherent phonon analysis, Phys. Rev. Lett. 97 (2006) 266401.

[103] M. M. Qazilbash, Z. Q. Li, V. Podzorov, M. Brehm, F. Keilmann, B. G. Chae, H. T. Kim, D. N. Basov, Electrostatic modification of infrared response in gated structures based on VO_2, Applied Physics Letters 92 (24) (2008) 241906.

[104] H. Coy, R. Cabrera, N. Sepúlveda, F. E. Fernández, Optoelectronic and all-optical multiple memory states in vanadium dioxide, Journal of Applied Physics 108 (11) (2010) 113115.

[105] A. Cavalleri, M. Rini, R. W. Schoenlein, Ultra-broadband femtosecond measurements of the photo-induced phase transition in VO_2: From the mid-IR to the hard X-rays, Journal of the Physical Society of Japan 75 (1) (2006) 011004.

[106] T. L. Cocker, L. V. Titova, S. Fourmaux, G. Holloway, H. C. Bandulet, D. Brassard, J. C. Kieffer, M. A. El Khakani, F. A. Hegmann, Phase diagram of the ultrafast photoinduced insulator-metal transition in vanadium dioxide, Phys. Rev. B 85 (2012) 155120.

[107] S. Wall, D. Wegkamp, L. Foglia, J. Nag, R. F. Haglund, J. Staehler, M. Wolf, Ultrafast changes in lattice symmetry probed by coherent phonons, Nature Communications 3 (2012) 721+.

[108] P. Baum, D.-S. Yang, A. H. Zewail, 4D visualization of transitional structures in phase transformations by electron diffraction, Science 318 (5851) (2007) 788–792.

[109] M. Hada, K. Okimura, J. Matsuo, Characterization of structural dynamics of VO_2 thin film on c-Al_2O_3 using in-air time-resolved X-ray diffraction, Phys. Rev. B 82 (2010) 153401.

[110] M. Hada, K. Okimura, J. Matsuo, Photo-induced lattice softening of excited-state VO_2, Applied Physics Letters 99 (5) (2011) 051903.

[111] S. Biermann, A. Poteryaev, A. I. Lichtenstein, A. Georges, Dynamical singlets and correlation-assisted peierls transition in VO_2, Phys. Rev. Lett. 94 (2005) 026404.

[112] R. M. Wentzcovitch, W. W. Schulz, P. B. Allen, VO_2: Peierls or mott-hubbard? a view from band theory, Phys. Rev. Lett. 72 (1994) 3389–3392.

[113] A. Furube, L. Du, K. Hara, R. Katoh, M. Tachiya, Ultrafast plasmon-induced electron transfer from gold nanodots into TiO_2 nanoparticles, Journal of the American Chemical Society 129 (48) (2007) 14852–14853.

[114] G. Xu, C.-M. Huang, M. Tazawa, P. Jin, D.-M. Chen, L. Miao, Electron injection assisted phase transition in a nano-Au-VO_2 junction, Applied Physics Letters 93 (6) (2008) 061911.

[115] D. W. Ferrara, E. R. MacQuarrie, J. Nag, A. B. Kaye, R. F. Haglund, Plasmon-enhanced low-intensity laser switching of gold::vanadium dioxide nanocomposites, Applied Physics Letters 98 (24) (2011) 241112.

[116] S. D. Brorson, J. G. Fujimoto, E. P. Ippen, Femtosecond electronic heat-transport dynamics in thin gold films, Phys. Rev. Lett. 59 (1987) 1962–1965.

[117] J. Hohlfeld, S. S. Wellershoff, J. G*ü*dde, U. Conrad, V. J*ä*hnke, E. Matthias, Electron and lattice dynamics following optical excitation of metals, Chemical Physics 251 (1–3) (2000) 237 – 258.

[118] G. Moriena, M. Hada, G. Sciaini, J. Matsuo, R. J. D. Miller, Femtosecond electron diffraction: Preparation and characterization of (110)-oriented bismuth films, Journal of Applied Physics 111 (4) (2012) 043504.

[119] D. Maurer, A. Leue, R. Heichele, V. Müller, Elastic behavior near the metal-insulator transition of VO_2, Phys. Rev. B 60 (1999) 13249–13252.

[120] Z. Lin, L. V. Zhigilei, V. Celli, Electron-phonon coupling and electron heat capacity of metals under conditions of strong electron-phonon nonequilibrium, Phys. Rev. B 77 (2008) 075133.

[121] I. Dokme, S. Altindal, M. Bulbul, The barrier height inhomogeneity in Al/p-Si schottky barrier diodes with native insulator layer, Applied Surface Science 252 (22) (2006) 7749–7754.

[122] Z. Horváth, M. Ádám, I. Szabó, M. Serényi, V. Tuyen, Modification of Al/Si interface and schottky barrier height with chemical treatment, Applied Surface Science 190 (2002) 441–444.

[123] B. N. Chichkov, C. Momma, S. Nolte, F. Alvensleben, A. Tünnermann, Femtosecond, picosecond and nanosecond laser ablation of solids, Applied Physics A 63 (2) (1996) 109–115.

[124] X. Liu, D. Du, G. Mourou, Laser ablation and micromachining with ultrashort laser pulses, Quantum Electronics, IEEE Journal of 33 (10) (1997) 1706–1716.

[125] P. Lorazo, L. J. Lewis, M. Meunier, Short-pulse laser ablation of solids: From phase explosion to fragmentation, Phys. Rev. Lett. 91 (2003) 225502.

[126] H. O. Jeschke, M. E. Garcia, K. H. Bennemann, Theory for the ultrafast ablation of graphite films, Phys. Rev. Lett. 87 (2001) 015003.

[127] B. J. Demaske, V. V. Zhakhovsky, N. A. Inogamov, I. I. Oleynik, Ablation and spallation of gold films irradiated by ultrashort laser pulses, Phys. Rev. B 82 (2010) 064113.

[128] X. Zhao, Y. C. Shin, Coulomb explosion and early plasma generation during femtosecond laser ablation of silicon at high laser fluence, Journal of Physics D: Applied Physics 46 (33) (2013) 335501.

[129] S. S. Mao, F. Quéré, S. Guizard, X. Mao, R. E. Russo, G. Petite, P. Martin, Dynamics of femtosecond laser interactions with dielectrics, Applied Physics A 79 (7) (2004) 1695–1709.

[130] P. Balling, J. Schou, Femtosecond-laser ablation dynamics of dielectrics: basics and applications for thin films, Reports on Progress in Physics 76 (3) (2013) 036502.

[131] E. Rabinowitch, Electron transfer spectra and their photochemical effects, Rev. Mod. Phys. 14 (1942) 112–131.

[132] H. N. Hersh, Proposed excitonic mechanism of color-center formation in alkali halides, Phys. Rev. 148 (1966) 928–932.

[133] M. Henyk, F. Costache, J. Reif, Femtosecond laser ablation from sodium chloride and barium fluoride, Applied Surface Science 186 (1–4) (2002) 381 – 384.

[134] A. G. Joly, W. P. Hess, K. M. Beck, J. T. Dickinson, Femtosecond time-resolved photo-stimulated desorption from ionic crystals, Applied Surface Science 186 (1–4) (2002) 339 – 344.

[135] W. P. Hess, A. G. Joly, K. M. Beck, R. M. Williams, J. T. Dickinson, Femtosecond time-resolved laser-induced desorption of positive ions from MgO, Applied Physics A 69 (1) (1999) S389–S393.

[136] W. P. Hess, A. G. Joly, K. M. Beck, M. Henyk, P. V. Sushko, P. E. Trevisanutto, A. L. Shluger, Laser control of desorption through selective surface excitation, The Journal of Physical Chemistry B 109 (42) (2005) 19563–19578.

[137] K. S. Song, C. H. Leung, R. T. Williams, A theoretical basis for the Rabin-Klick criterion in terms of off-centre self-trapped-exciton relaxation, Journal of Physics: Condensed Matter 1 (4) (1989) 683.

[138] T. Tokizaki, T. Makimura, H. Akiyama, A. Nakamura, K. Tanimura, N. Itoh, Femtosecond cascade-excitation spectroscopy for nonradiative deexcitation and lattice relaxation of the self-trapped exciton in NaCl, Phys. Rev. Lett. 67 (1991) 2701–2704.

[139] K. Edamatsu, M. Sumita, S. Hirota, M. Hirai, Transient absorption due to self-trapped excitons in NaBr and NaI, Phys. Rev. B 47 (1993) 6747–6750.

[140] S. Iwai, T. Tokizaki, A. Nakamura, K. Tanimura, N. Itoh, A. Shluger, One-center small polarons as short-lived precursors in self-trapping processes of holes and electron-hole pairs in alkali iodides, Phys. Rev. Lett. 76 (1996) 1691–1694.

[141] A. L. Shluger, K. Tanimura, Laser-induced reactions in crystals: femtosecond pump-probe spectroscopy and *ab initio* calculations of self-trapped excitons and holes in KBr, Phys. Rev. B 61 (2000) 5392–5402.

[142] K. Tanimura, W. P. Hess, Temperature-dependent yield of Frenkel pairs generated by valence excitation in NaCl, Phys. Rev. B 69 (2004) 155102.

[143] N. Ichimura, T. Kawai, S. Hashimoto, F-center formation in KI crystals under high-density optical excitation, Phys. Rev. B 75 (2007) 155121.

[144] J. T. Dickinson, S. Orlando, S. M. Avanesyan, S. C. Langford, Color center formation in soda lime glass and NaCl single crystals with femtosecond laser pulses, Applied Physics A 79 (4-6) (2004) 859–864.

[145] R. Stoian, A. Rosenfeld, D. Ashkenasi, I. V. Hertel, N. M. Bulgakova, E. E. B. Campbell, Surface charging and impulsive ion ejection during ultrashort pulsed laser ablation, Phys. Rev. Lett. 88 (2002) 097603.

[146] R. Stoian, D. Ashkenasi, A. Rosenfeld, E. E. B. Campbell, Coulomb explosion in ultrashort pulsed laser ablation of Al_2O_3, Phys. Rev. B 62 (2000) 13167–13173.

[147] G. Sciaini, R. J. D. Miller, Femtosecond electron diffraction: heralding the era of atomically resolved dynamics, Reports on Progress in Physics 74 (9) (2011) 096101.

[148] C. V. Shank, R. Yen, C. Hirlimann, Time-resolved reflectivity measurements of femtosecond-optical-pulse-induced phase transitions in silicon, Phys. Rev. Lett. 50 (1983) 454–457.

[149] H. W. K. Tom, G. D. Aumiller, C. H. Brito-Cruz, Time-resolved study of laser-induced disorder of Si surfaces, Phys. Rev. Lett. 60 (1988) 1438–1441.

[150] K. Sokolowski-Tinten, J. Bialkowski, D. von der Linde, Ultrafast laser-induced order-disorder transitions in semiconductors, Phys. Rev. B 51 (1995) 14186–14198.

[151] K. Sokolowski-Tinten, J. Bialkowski, A. Cavalleri, D. von der Linde, A. Oparin, J. Meyer-ter Vehn, S. I. Anisimov, Transient states of matter during short pulse laser ablation, Phys. Rev. Lett. 81 (1998) 224–227.

[152] K. Sokolowski-Tinten, D. von der Linde, Generation of dense electron-hole plasmas in silicon, Phys. Rev. B 61 (2000) 2643–2650.

[153] T. Y. Choi, C. P. Grigoropoulos, Plasma and ablation dynamics in ultrafast laser processing of crystalline silicon, Journal of Applied Physics 92 (9) (2002) 4918–4925.

[154] H. Dachraoui, W. Husinsky, Thresholds of plasma formation in silicon identified by optimizing the ablation laser pulse form, Phys. Rev. Lett. 97 (2006) 107601.

[155] P. Stampfli, K. H. Bennemann, Time dependence of the laser-induced femtosecond lattice instability of Si and GaAs: Role of longitudinal optical distortions, Phys. Rev. B 49 (1994) 7299–7305.

[156] C. W. Siders, A. Cavalleri, K. Sokolowski-Tinten, C. Tóth, T. Guo, M. Kammler, M. H. v. Hoegen, K. R. Wilson, D. v. d. Linde, C. P. J. Barty, Detection of nonthermal melting by ultrafast X-ray diffraction, Science 286 (5443) (1999) 1340–1342.

[157] A. Rousse, C. Rischel, S. Fourmaux, I. Uschmann, S. Sebban, G. Grillon, P. Balcou, E. Förster, J. P. Geindre, P. Audebert, J. C. Gauthier, D. Hulin, Non-thermal melting in semiconductors measured at femtosecond resolution, Nature 410 (6824) (2001) 65–68, PMID: 11242040.

[158] E. S. Zijlstra, J. Walkenhorst, M. E. Garcia, Anharmonic noninertial lattice dynamics during ultrafast nonthermal melting of InSb, Phys. Rev. Lett. 101 (2008) 135701.

[159] A. Cavalleri, K. Sokolowski-Tinten, J. Bialkowski, M. Schreiner, D. von der Linde, Femtosecond melting and ablation of semiconductors studied with time of flight mass spectroscopy, Journal of Applied Physics 85 (6) (1999) 3301–3309.

[160] W. L. Kruer, Laser plasma interactions with intensities from 10^{12}–10^{21} W/cm^2, Physics of Plasmas 10 (5) (2003) 2087–2092.

[161] C. Favre, V. Boutou, S. C. Hill, W. Zimmer, M. Krenz, H. Lambrecht, J. Yu, R. K. Chang, L. Woeste, J.-P. Wolf, White-light nanosource with directional emission, Phys. Rev. Lett. 89 (2002) 035002.

[162] D. von der Linde, H. Schüler, Breakdown threshold and plasma formation in femtosecond laser–solid interaction, J. Opt. Soc. Am. B 13 (1) (1996) 216–222.

[163] D. Ashkenasi, A. Rosenfeld, H. Varel, M. Wähmer, E. Campbell, Laser processing of sapphire with picosecond and sub-picosecond pulses, Applied Surface Science 120 (1–2) (1997) 65 – 80.

[164] H. X. Gao, L.-M. Peng, J. M. Zuo, Lattice dynamics and Debye–Waller factors of some compounds with the sodium chloride structure, Acta Crystallographica Section A 55 (6) (1999) 1014–1025.

[165] L.-M. Peng, Quasi-dynamical electron diffraction – a kinematic type of expression for the dynamical diffracted-beam amplitudes, Acta Crystallographica Section A 56 (6) (2000) 511–518.

[166] J. D. Makinson, J. S. Lee, S. H. Magner, R. J. De Angelis, W. N. Weins, A. S. Hieronymus, X-ray diffraction signatures of defects in nanocrystalline materials, Adv. X-ray Anal. 42 (1998) 407–411.

[167] S. Wu, P. Geiser, J. Jun, J. Karpinski, R. Sobolewski, Femtosecond optical generation and detection of coherent acoustic phonons in GaN single crystals, Phys. Rev. B 76 (2007) 085210.

[168] F. Hudert, A. Bruchhausen, D. Issenmann, O. Schecker, R. Waitz, A. Erbe, E. Scheer, T. Dekorsy, A. Mlayah, J.-R. Huntzinger, Confined longitudinal acoustic phonon modes in free-standing si membranes coherently excited by femtosecond laser pulses, Phys. Rev. B 79 (2009) 201307.

[169] Y. Hayashi, Y. Tanaka, T. Kirimura, N. Tsukuda, E. Kuramoto, T. Ishikawa, Acoustic pulse echoes probed with time-resolved X-Ray triple-crystal diffractometry, Phys. Rev. Lett. 96 (2006) 115505.

[170] J. Tang, Coherent phonon excitation and linear thermal expansion in structural dynamics and ultrafast electron diffraction of laser-heated metals, The Journal of Chemical Physics 128 (16) (2008) 164702.

[171] J. W. Rohlf, Modern Physics from a to Z, Wiley, John & Sons, Incorporated, 1994.

[172] P. F. Weck, K. Kirby, P. C. Stancil, Ab initio configuration interaction study of the low-lying $^1\sigma^+$ electronic states of LiCl, The Journal of Chemical Physics 120 (9) (2004) 4216–4222.

[173] J. Freund, R. Ingalls, E. D. Crozier, Extended x-ray-absorption fine-structure study of alkali-metal halides under high pressure, Phys. Rev. B 43 (1991) 9894–9905.

[174] M. Hada, K. Pichugin, G. Sciaini, Ultrafast structural dynamics with table top femtosecond hard X-ray and electron diffraction setups, European Physical Journal Special Topics 222 (2013) 1093–1123.

[175] C. M. Scoby, R. K. Li, P. Musumeci, Effect of an ultrafast laser induced plasma on a relativistic electron beam to determine temporal overlap in pump–probe experiments, Ultramicroscopy 127 (0) (2013) 14 – 18.

[176] M. Felber, M. Hoffmann, U. Mavric, H. Schlarb, S. Schulz, W. Jalmuzna, Laser Synchronization at REGAE using Phase Detection at an Intermediate Frequency, Proceedings of IPAC2012 WEPPD048 (2012) 2624–2626.

[177] G. H. Kassier, K. Haupt, N. Erasmus, E. G. Rohwer, H. M. von Bergmann, H. Schwoerer, S. M. M. Coelho, F. D. Auret, A compact streak camera for 150 fs time resolved measurement of bright pulses in ultrafast electron diffraction, Review of Scientific Instruments 81 (10) (2010) 105103.

[178] P. Musumeci, J. T. Moody, C. M. Scoby, M. S. Gutierrez, T. Tran, RF streak camera based ultrafast relativistic electron diffraction, Review of Scientific Instruments 80 (1) (2009) 013302.

[179] H.-c. Lihn, P. Kung, C. Settakorn, H. Wiedemann, D. Bocek, Measurement of subpicosecond electron pulses, Phys. Rev. E 53 (1996) 6413–6418.

[180] C. Mueller, M. Harb, J. R. Dwyer, R. J. D. Miller, Nanofluidic cells with controlled pathlength and liquid flow for rapid, high-resolution in situ imaging with electrons, The Journal of Physical Chemistry Letters 4 (14) (2013) 2339–2347.

List of Publications

Publications

M. Hada*, D. Zhang*, K. Pichugin, J. Hirscht, M. A. Kochman, S. A. Hayes, S. Manz, R. Y. N. Gengler, D. A. Wann, T. Seki, G. Moriena, C. A. Morrison, J. Matsuo, G. Sciaini, and R. J. D. Miller, "Cold ablation driven by localised forces in alkali halides," submitted to Nat Commun. (∗ equal contribution).

R.Y. N. Gengler, D. Badali, D. Zhang, K. Dimos, K. Spyrou, D. Gournis, and R. J. D. Miller, "Revealing the ultrafast process behind the photoreduction of graphene oxide," Nat Commun 4 (2560) (2013) 3560.

M. Hada, D. Zhang, A. Casandruc, R. J. D. Miller, Y. Hontani, J. Matsuo, R. E. Marvel, and R. F. Haglund, "Hot electron injection driven phase transitions", Phys. Rev. B 86 (13) (2012) 134101.

M. Hada, J. Hirscht, D. Zhang, S. Manz, K. Pichugin, D. Mazurenko, S. Bayesteh, H. Delsim-Hashemi, K. Floettmann, M. Huening, S. Lederer, G. Moriena, C. Mueller, G. Sciaini, and R. J. D. Miller, "REGAE: New Source for Atomically Resolved Dynamics," Research in Optical Sciences, (2012), JT2A.47.

Conferences

D. Zhang, M. Hada, J. Hirscht, S. A. Hayes, K. Pichugin, A. Casandruc, S. Manz, R. Y. N. Gengler, T. Seki, J. Matsuo, G. Moriena, G. Sciaini, and R. J. D. Miller, "A femtosecond electron diffraction study: Electronically-driven ablation via highly localized electronic states, 15th European Symposium on Gas Electron Diffraction, Frauenchiemsee, Germany, June 23rd 2013, oral presentation.

D. Zhang, S. Manz, A. Casandruc, J. Hirscht, S. Keskin, J. Nicholls, K. Pichugin, S. A. Hayes, S. Jangam, T. Hasegawa, A. Marx, S. Bayesteh, H. Delsim-Hashemi, M. Felber, H. Schlarb, M. Hoffmann, M. Huening, T. Gehrke, F. Mayet, M. Hachmann, G. Moriena, S. Epp, M. Hada, K. Floettmann, R. J. D. Miller, "REGAE: Towards Ultrafast electron diffraction and dynamic microscopy", 15th European Symposium on Gas Electron Diffraction, Frauenchiemsee, Germany, June 23rd-27th, 2013, poster presentation.

D. Zhang, M. Hada, R. Y. N. Gengler, T. Seki, J. Matsuo, G. Sciaini and R. J. D. Miller, "Pauli Driven Cold Explosion in Alkali Halides", Banff Meeting on Structural Dynamics, The Banff Center, Banff, Alberta, Canada, February 17th-20th, 2013, poster presentation.

D. Zhang, J. Hirscht, M. Hada, S. Manz, K. Pichugin, D. A. Mazurenko, S. Bayesteh, H. Delsim-Hashemi, K. Floettmann, M. Huening, S. Lederer, G. Moriena, C. Mueller, G. Sciaini, R. J. D. Miller, "REGAE: New Source for Atomically Resolved Dynamics" Banff Meeting on Structural Dynamics, The Banff Center, Banff, Alberta, Canada, February 19th-22nd, 2012, poster presentation.

Acknowledgements

After three years work in laser area during my master study, I am increasingly attracted by the application of laser in discovering the nature of physics. In the early 2010, I was luckily given the opportunity by Prof. R. J. Dwayne Miller to do a Ph.D and continue to investigate science. As the first member in Miller group at University of Hamburg in Germany, I have been given a lot of opportunities to learn and grow. It is very challenging to start up a new lab especially with only a few people at the beginning and I need to train myself to learn as many things as possible – Optics, electronics, programming, management, etc. With over three years hard work we have developed three systems and the FED team has grown up to more than 10 people. Benefiting from my laser background I have been worked on laser related setups and developed the first time-resolved system – optical pump-probe setup, with which the first two results had shown up in Miller group in Hamburg. Another focus of my work is to develop the new FED electron sources, which is the field I am most interested in. I appreciate the chance to join the development of the electron gun from the very beginning. This time is tough, but there were so many people who had helped me and guided me to the right direction, and I have learned more than I can imagine. Therefore, I would like to take this opportunity to thank those who helped and supported me to complete the Ph.D study.

I would like to express the deepest appreciation to my supervisor Prof. R. J. Dwayne Miller, who has been a constant source of inspiration and support for the work that led to this thesis. His insistence to aim for the impossible has been my driving force to explore the unknown scientific area throughout my years at the University of Hamburg.

Thank Germ*á*n A. Sciaini, Gustavo Moriena, Julian Hirscht, Dmitry Mazurenko, Kostyantyn Pichugin, Stuart Hayes, and Masaki Hada for their help in building the brand new lab. Their excellent ideas, suggestions, experimental and theoretical works do lay the foundation of my research. Special thanks to Germ*á*n A. Sciaini and Masaki Hada. As FED group leaders, they have been consistently giving me guidance and support in my project. Germ*á*n is a great scientist and has enormous enthusiasm in exploring the scientific world. He has been motivating, encouraging, and enlightening on my work. Masaki has been showing his genuine caring, concern, and faith in me during my Ph.D. His guidance on my work has enabled the completion of the project. We had spent countless time working together, and I have learned a lot from his various knowledge on physics, engineering, and intriguing sense. I owe special thanks to Julian, Stuart and Kostyantyn. Julian, Thank you for constructing the electron gun and designing so many parts for the machine. Thank you, Stuart, for taking so many time to upgrade the system, which has made it possible to make the electron gun in a better condition. And Kostyantyn, thank you for all the help with developing the software. I had learned so much from your gifted programming skill.

Meanwhile I wish to express my sincere thanks to our REGAE team members Stephanie Manz, Albert Casandruc, Sercan Keskin, Rolf Loch, Alexander Marx, Sascha Epp and Yingpeng Zhong, who have been working with me on REGAE and giving me unconditional support during the completion of my thesis. I would like to thank Stephanie Manz, Rolf Loch, and Sascha Epp for their valuable comments and professional suggestions about the writing of the thesis.

In addition, I want to recognize the following group members for their suggestions, ideas and helpful work to the project: Valentyn Prokhorenko, Etienne Pelletier, Regis Gengler, Taisuke Hasegawa, Nadja Bardenheuer, Daniel Badali, Haider Zia, Samansa Maneshi, Santosh Jangam, Hubert Jean-Ruel, Lai Chung Liu, Meng Gao, Yifeng Jiang, Rui Xan, Djordje Gitaric, and Josef Gonschior.

I would also like to express my gratitude to all members from DESY, with whom I have closely collaborated for REGAE: Klaus Floettmann, Hossein Delsim-hashemi, Shima Bayesteh, Matthias Hoffmann, Matthias Felber, Frank Mayet, Max Hachmann, Michael Seebach and Sven Lederer. Especially thanks to Klaus, who has given me many supports on accelerator physics and simulation work with ASTRA. His expertise had made possible REGAE moving forward. Hossein and Shima's work on detecting system has finalized the FED system. I am extremely grateful and indebted to their expert, sincere and valuable guidance to me.

I would also like to mention my trustable and reliable friend Lushuai Cao who had given me countless help during my staying in Germany. Meanwhile all other friends I had fun moments: Cristian, Vikaran, Qing, Guang, Hongming, Jia et al.

I want to thank my parents and brother for their support and patience throughout many years of my school study. Thanks for their care, love and support.

Last but most importantly, I would like to thank my beloved wife Na Wang for her deep love, her encouragement and patience.